

Wetting Dynamics Beneath an Impacting Droplet

Présentée le 27 février 2023

Faculté des sciences et techniques de l'ingénieur
Laboratoire de mécanique des interfaces souples
Programme doctoral en mécanique

pour l'obtention du grade de Docteur ès Sciences

par

Ramin KAVIANI

Acceptée sur proposition du jury

Prof. B. T. A. Lecampion, président du jury
Prof. J. M. Kolinski, directeur de thèse
Prof. R. Tadmor, rapporteur
Prof. A. Carlson, rapporteur
Prof. M. Farhat, rapporteur

Dedicated to MohammadAli Kaviani

Acknowledgements

First and foremost, I wish to thank my supervisor and the head of the EMSI lab, prof. John M. Kolinski, who accepted me as a PhD student in his group. John, I am indebted to you for making our lab an ideal place for me to work in and enlightening me into the ways of the beauties in experimental research. I have always felt assured with your help and endless support.

I enjoyed being a part of the EMSI team, sharing ideas with my labmates, past and present, and having everybody's support. Martin, thanks a bunch for sharing an office with me, being such a great friend, and all the interesting discussions we had about life and work. Lebo and Albert, many thanks for creating the fun moments we shared. I appreciate knowing and working with you and will never forget your help and kindness. My mate, Youssef, thanks heaps for your friendship and the time that you put to translate my abstract to French. Xinyue, Chenzhuo and Dylan, thanks for the small chats and being such good team mates. Evelyn, merci beaucoup for all your assistance during this journey.

I would like to thank my committee members for kindly accepting to be in my thesis jury and taking the time to critically read this thesis. I wish to pay my regards to prof. Mohamed Farhat, prof. Rafael Tadmor, and prof. Andreas Carlson for reviewing this dissertation and for their valuable comments on the manuscript. I appreciate prof. Brice Lecampion for accepting to preside over the jury.

I would like to thank several scientists at EPFL who were very generous with me. The (incomplete) list includes Navid Borhani, Amirhossein Saba, Ludovic Keiser, Demetri Psaltis, Pan Jia, Francois Gallaire, and Yves Bellouard. I also thank all friends and colleagues from LFMI, ECPS, and ANEMS groups at EPFL.

My dearest friends in Switzerland made my life enjoyable as I worked on my thesis, especially Shahrad, Amin, Omid, Sajjad, Emilio, Petra, Elisabeth, and MohammadHossesin. Thanks y'all for the happy moments and the unforgettable memories. I wish you the best for your future and hope we can meet up some time in the not too distant future.

Finally, I would like to express my sincerest gratitude to my parents, Mina and MohammadAli, who have provided everything that one could hope for in a family. Thank you for your countless sacrifices and unconditional love. I would not be able to start nor finish this PhD without your support. I further owe a great deal of gratitude to my

Acknowledgements

siblings, Hanieh and Raheleh. I am particularly indebted to you for your encouragement, steadfast support, and continuing love.

Lausanne, 30 January 2023

Ramin Kaviani

Abstract

Many natural and industrial processes involve fluid flow at a three phase interface between liquid, solid and gas. When the liquid is forced to move rapidly over the solid surface, the physical mechanisms governing contact line motions are multi-phase and multi-scale and as a consequence the dynamics can be complex. We perform direct observations of the wetting phenomena at the interface of liquid droplets impacting on a rigid flat surface using high resolution microscopy and high speed imaging.

Upon impact of a liquid droplet on a smooth solid, a thin air film is formed and squeezed in between the two. Depending on the impact parameters, the air film can remain stable and facilitate the rebound of the droplet, or liquid-solid contact occurs that binds the droplet to the solid surface, leads to subsequent spreading or splashing. In order for the liquid-solid contact to occur, the air film must rupture under the impacting droplet. The physical mechanisms responsible for the rupture of the air film have not yet been conclusively determined; in particular a quantitative test for the theory of air film rupture is lacking. Currently, the mechanism assumed to be responsible for liquid-solid contact formation is an interfacial forces-driven destabilization of the initially flat liquid-air interface. The liquid-air interface is destabilized when the attractive stresses (*e.g.*, van der Waals forces or electrostatic forces) overcome the stress associated with deforming the surface due to surface tension. This instability is characterized by a critical air film thickness (h^*) at which the film destabilizes and wetting initiates. We carefully measured the air film thickness at which the droplet rebounds for water-glycerol solution and silicon oil droplets with similar viscosities on atomically smooth mica surfaces. h^* for the silicon oil (≈ 30 nm) is smaller than that of the water-glycerol solution (≈ 60 nm); however, the local minimum air film thickness (h_{\min}) immediately prior to contact formation, is approximately the same value for both liquids (≈ 20 nm).

We experimentally probe the dynamics of wetting that occur when an impacting drop first contacts a dry glass surface. We show that initially, wetting is mediated by the formation and growth of nano-scale liquid bridges that bind the liquid to the solid across a thin film of air. As the liquid bridge expands, air accumulates and deforms the liquid-air interface, and a capillary wave forms ahead of the advancing wetting front. This capillary wave regularizes the pressure at the advancing wetting front in a manner that generates an anomalously low wetting velocity. As the liquid viscosity increases, the wetting front

velocity decreases; we provide a phenomenological scaling for the observed decrease of the wetting velocity with liquid viscosity.

In order to investigate the interfacial kinematics involved in the droplet impact with high fidelity and resolve the small length scales involved, we implemented two high-speed microscopy techniques, including monochromatic Fizeau interferometry (FIF) contrast microscopy and frustrated total internal reflection (FTIR) microscopy. We improved the accuracy of the FTIR microscopy technique on weakly birefringent substrates from the previously reported ~ 30 nm to ~ 5 nm by adding few readily accessible optical elements to the conventional FTIR setup. We carefully calibrated our combined FIF and FTIR setup using a nano-meter precise piezo stage.

In an effort to push the accuracy limits of combined FIF and FTIR microscopy, we tackled the trade-off between imaging rate and region of interest using a deep-learning framework. The deep learning network was trained on synchronous profilometry data acquired using the two imaging modalities, such that the FTIR imaging data were recorded at high resolution, while the FIF imaging data were recorded with a less spatial resolution and larger field of view. The deep learning framework used a multi-layer convolutional neural network to enhance the FIF image resolution based upon the data in the FTIR images. In this way, we obtain the high spatial resolution of the FTIR measurements from the lower resolution FIF data. A high-order overset technique ultimately yields full up-scaled images from the network outputs without losing precision. We evaluated the accuracy of the super-resolved image using test data. We implemented this hybrid framework, called HOTNNET, in its entirety on high-speed imaging profilometry data acquired in the study of droplet impacts on a smooth, solid surface. We use HOTNNET to recover full, high-resolution images at high rates while bypassing the need for explicit interferometric phase unwrapping. This framework can be readily adapted to other paired datasets by retraining the network on the novel data.

Key words: Wetting; Droplet Impact; Air Entrainment; Dynamic Contact Lines; Frustrated Total Internal Reflection Microscopy; Reflection Interference Contrast Microscopy; Deep Learning; Super-Resolution.

Résumé

De nombreux processus naturels et industriels impliquent un écoulement de fluide à une interface à trois phases entre liquide, solide et gaz. Lorsque le liquide est contraint de se déplacer rapidement sur la surface solide, les mécanismes physiques régissant les mouvements rapides de la ligne de contact sont à plusieurs phases et à plusieurs échelles et, par conséquent, la dynamique peut être complexe. Nous réalisons des observations directes du phénomène d'impact de gouttelette sur la surface de la gouttelette avant et après la formation de contact en utilisant des outils de microscopie à haute résolutions et une imagerie à haute vitesse.

Lors de l'impact d'une goutte de liquide sur une surface solide lisse, un film d'air mince est formé et comprimé entre les deux. Selon les paramètres d'impact, le film d'air peut rester stable et faciliter le rebond de la goutte, ou bien un contact liquide-solide se produit qui lie la goutte à la surface solide, entraînant une propagation ultérieure ou une éclaboussure. Pour que le contact liquide se produise, le film d'air doit se rompre sous l'impact de la goutte. Les mécanismes physiques responsables de la rupture du film d'air n'ont pas encore été déterminés de manière concluante ; en particulier, il manque un test quantitatif pour la théorie de la rupture du film d'air. Actuellement, on suppose que le mécanisme responsable de la formation de contact liquide-solide est une déstabilisation de l'interface liquide-air due aux forces d'interfaces. L'interface liquide-air est déstabilisée lorsque les contraintes attractives (par exemple, les forces de van der Waals ou les forces électrostatiques) surpassent la contrainte associée à la déformation de la surface due à la tension superficielle. Cette instabilité est caractérisée par une épaisseur critique du film d'air à laquelle le film se déséquilibre et le mouillage commence. Nous avons soigneusement mesuré l'épaisseur du film d'air à laquelle la goutte rebondit pour des gouttes d'eau-glycérol et d'huile de silicone de viscosités similaires sur des surfaces de mica à l'état atomiquement lisse. h^* pour l'huile de silicone (≈ 30 nm) est inférieure à celle de la solution eau-glycérol (≈ 60 nm); cependant, l'épaisseur minimale de film d'air (h_{\min}) immédiatement avant la formation de contact est approximativement la même pour les deux liquides (≈ 20 nm).

Nous explorons expérimentalement les dynamiques de mouillage qui se produisent lorsqu'une goutte en impact entre en contact pour la première fois avec une surface de verre sèche. Nous montrons qu'au départ, le mouillage est régi par la formation et la croissance de ponts liquides à l'échelle du nanomètre qui lient le liquide au solide à travers un film mince d'air. À mesure que le pont liquide s'étend, de l'air s'accumule et

déforme l'interface liquide-air, et une onde capillaire se forme devant le front de mouillage avançant. Cette onde capillaire régularise la pression au front de mouillage avançant de manière à générer une vitesse de mouillage anormalement faible. À mesure que la viscosité du liquide augmente, la vitesse du front de mouillage diminue ; nous fournissons un dimensionnement phénoménologique de la diminution observée de la vitesse de mouillage avec la viscosité du liquide. Afin d'enquêter sur les cinématiques interfaciales impliquées dans l'impact de la goutte avec une grande fidélité et de résoudre les petites échelles de longueur impliquées, nous avons mis en œuvre deux techniques de microscopie à haute vitesse, notamment la microscopie de contraste par interférométrie Fizeau monochromatique (FIF) et la microscopie par réflexion totale frustrée (FTIR). Nous avons amélioré la précision de la technique de microscopie FTIR sur les substrats faiblement biréfringents de l'ordre de 30 nm à environ 5 nm en ajoutant quelques éléments optiques facilement accessibles à la configuration FTIR conventionnelle. Nous avons soigneusement étalonné notre configuration combinée FIF et FTIR en utilisant une platine piezo à précision nanométrique.

Dans le but de pousser les limites de précision de la microscopie combinée FIF et FTIR, nous avons abordé le compromis entre le taux d'imagerie et la région d'intérêt à l'aide d'un cadre d'apprentissage profond. Le réseau d'apprentissage profond a été entraîné sur des données de profilométrie synchronisée acquises à l'aide des deux modalités d'imagerie, de sorte que les données d'imagerie FTIR ont été enregistrées à haute résolution, tandis que les données d'imagerie FIF ont été enregistrées avec une résolution spatiale moins importante et un champ de vision plus large. Le cadre d'apprentissage profond a utilisé un réseau de neurones à convolution à plusieurs couches pour améliorer la résolution de l'image FIF sur la base des données des images FTIR. De cette manière, nous obtenons une haute résolution spatiale des mesures FTIR à partir des données FIF de moins bonne résolution. Une technique d'overset d'ordre élevé permet finalement d'obtenir des images entièrement upscalées à partir des sorties du réseau sans perte de précision. Nous avons évalué la précision de l'image sur-résolue à l'aide de données de test. Nous avons mis en œuvre intégralement le cadre hybride, appelé HOTNNET, sur des données de profilométrie d'imagerie à haute vitesse acquises dans l'étude des impacts de goutte sur une surface solide lisse. Nous utilisons HOTNNET pour récupérer des images à haute résolution complètes à des taux élevés tout en évitant la nécessité de déroulage explicite de la phase interférométrique. Ce cadre peut être facilement adapté à d'autres ensembles de données appariées en réentraînant le réseau sur les données nouvelles.

Mots clés: Mouillage; Impact de gouttes; Entraînement d'air; Lignes de contact dynamiques; Microscopie par réflexion interne totale frustrée; Microscopie de contraste d'interférence de réflexion; Apprentissage profond; Sur-résolution.

Contents

Acknowledgements	i
Abstract (English/Français)	iii
Nomenclature	ix
1 Introduction	1
1.1 Droplet Bouncing	2
1.2 Low Speed Impact Dynamics	5
1.3 Outline of this Manuscript	9
2 Interface Imaging & Resolution Enhancement with HOTNNET	11
2.1 Imaging Setup	13
2.2 Deep convolutional neural network	15
2.3 Mosaic mapping with overset technique	18
2.4 HOTNNET Results	21
2.5 Discussion	23
2.6 Conclusion	27
3 FTIR and FIF Microscopy	29
3.1 FTIR Profilometry Modality	29
3.2 Interferometric Imaging and Profilometry	33
3.3 Calibration	37
4 Droplet Impact: Air Film Rupture	39
4.1 Experimental Setup	40
4.2 Squeezing and Piercing the Air layer	42
4.3 Discussion	46
4.4 Conclusion	50
5 Droplet Impact: Liquid-Solid Nucleated Contact	51
5.1 Method	51
5.2 Results	52
5.3 Discussion	58

6	Conclusions and Perspectives	61
6.1	Conclusions	61
6.1.1	Microscopy	61
6.1.2	Wetting Initiation	61
6.1.3	Wetting Propagation	62
6.2	Perspectives	62
6.2.1	Microscopy on Curved Surfaces and Scale Dependency	62
6.2.2	Soft Interfaces	63
6.2.3	Additional Physical Effects	63
	Bibliography	65
	Curriculum Vitae	77

Nomenclature

Abbreviations

BC	Boundary Condition
CCD	Charge-Coupled Device
CFD	Computational Fluid Dynamics
FIF	Fizeau Interferometry
GKE	Gas Kinetic Effects
HOTNNET	High-order OverseT assembly method and the deep convolutional Neural NETWORK
MD	Molecular Dynamics
MKT	Molecular Kinematic Theory
N-S	Navier-Stokes
NRMSE	Normalized Root Mean-Squared Error
RMS	Root Mean Square
VGG	Visual Geometry Group
w.r.t	with respect to

Roman Letters

\mathcal{B}	Magnetic field
\mathcal{E}	Electric field
c_A	Light speed in medium A
n_A	Refractive index medium A
r	Reflection coefficient in Fresnel equations
t	Transmission coefficient in Fresnel equations
\mathbf{u}	Velocity vector
Bo	Bond Number
Ca	Capillary Number
D	Droplet Diameter
G	Gibbs Free Energy
g	Gravity Acceleration
H	Height

h	Gap in liquid-gas interface or air layer thickness
I	Light Intensity
k_G	Gas specific heat ratio
L	Length / Characteristic length
p	Pressure
Re	Reynolds Number
t	Time
U	Velocity / Reference velocity
u_i	i -th coordinate velocity
We	Weber Number
x_i	Spatial coordinates
BS	Non-polarizing Beam-Splitter
CL	Condenser Lens
LCVR	Liquid Crystal Variable Retarder
PBS	Polarizing Beam-Splitter

Greek Letters

η	Dynamic viscosity
γ	Surface tension
κ	Wave-number in vacuum
λ	Wavelength in vacuum
μ_A	Permeability in medium A
ν	Kinematic viscosity
ρ	Density
ε_A	Permittivity in medium A

Subscripts

0	Initial Condition or constant value
\perp	s-polarized
max	Maximum
min	Minimum
A,B,C,...	Of medium A, B, C
G	Of gas properties
L	Of liquid properties
D	Dynamic
i, j, k, \dots	Used for index notation
ref	The reference value for non-dimensionalization
S	Static

Nomenclature

Conventions

$:=$	Left-hand-side is defined as
$=:$	Right-hand-side is defined as
$\mathcal{A}, \mathcal{B}, \mathcal{C}, \dots$	Vectors used in Maxwell's equations and Jones matrix algebra
$\mathbf{A}, \mathbf{B}, \mathbf{C}, \dots$	Vectors
$\mathbf{a}, \mathbf{b}, \mathbf{c}, \dots$	Vectors
$\mathbf{A}, \mathbf{B}, \mathbf{C}, \dots$	Matrices
$\underline{\underline{A}}, \underline{\underline{\Sigma}}, \dots$	2nd-Order tensors

1 Introduction

The impact of a drop on a surface is a ubiquitous phenomenon in our daily experience. It also plays a vital role in a plethora of natural and industrial applications, including bioaerosol generation, pesticide control, deposition of inks, resins and coatings. The phenomenon intrigued scientists for centuries. Leonardo da Vinci drew a water drop splashing in the margins of *The Codex Leicester* in 1506. In 1877, through basic observations, Worthington and Clifton [131] sketched different outcomes of impacting droplets on a solid substrate; namely bounce, spread or splash.

Since then, many researchers have considered the dynamics of impacting droplets (see for example review by Josserand and Thoroddsen [61]). They include studies of Newtonian fluids [10, 14, 25, 58, 74, 76, 81, 95, 100, 107, 109, 114, 116, 118] and non-Newtonian fluids, *e.g.*, power-law liquids [4, 17] and shear-thinning fluids [4, 89, 130].

The experiments of Thoroddsen et al. [121] on impacting droplets have shown the formation of a dimple beneath the drop and entrapment of an air bubble. They measured the initial thickness of the air disk to be in microscopic scales. It is only recent that laboratory tools can capture the involved small scales [30, 31, 69, 70, 79, 83, 125]. The dynamics of the droplet impact phenomena has been captured using X-ray imaging [76], interferometry [39], white color interferometry [125], two-color interferometry [32], tri-wavelength interferometry [45] and total internal reflection method [70]. Such imaging tools have helped to reveal physics occurring in micro-scales that may have macroscopic consequences. This has drawn sustained research interests to revisit the basic phenomena from a fundamental perspective. Recent investigations into the influence of the ambient air on droplet impact dynamics establish the critical effect the gas has on the outcome of the liquid-solid impact process, including suppression of splashing [86–88, 134], a lift-off transition in the liquid-air interface [69], and complete rebound of the drop from a hydrophilic surface [28, 29, 68], adding to our understanding of the role of air in droplet impacts [18, 38, 39, 61, 101, 135].

As a prelude to wetting, the impinging liquid first compresses the air beneath the drop

into a dimple [11, 76, 119, 121], and subsequently confines the intervening air into a nanometer-thin film^I circumscribing the dimple region [31, 69, 70, 125]. The dynamics at the leading edge of the spreading liquid have been shown to be distinct from the dimple region, and are important for droplet spreading and splashing [38, 84, 122]. On ideal smooth surfaces, such as freshly cleaved mica, contact occurs when the thickness of the thin air film reaches a few nanometers, and the interface is destabilized by surface forces [68]. On typical surfaces, defects nucleate contact much earlier; thus, liquid-solid contact initiates by the formation of a capillary bridge, linking the solid and liquid. The liquid bridge grows as the fluid rapidly wicks through the thin film of air, binding the drop to the surface [31, 68, 69]. These dynamics lead to the onset of wetting, and bear remarkable similarity to dewetting studies on solid surfaces [15] and freely suspended viscous films [12], with key differences introduced by the nanometer thin air film. In order for the nascent contact to grow, the spreading liquid must fully displace the air beneath the drop ahead of the propagating contact line. Indeed, recent simulations of dynamic wetting underscore the overwhelming difficulty of predicting the role of liquid viscosity in the wetting process due to the complicated flow patterns occurring across many scales [113].

Kolinski et al. [70] coined the expression “droplet skating on an air film” for the initial impact dynamics and further studied increased contact formation by isolated contacts and increased impact velocity [69] and the rebound of droplet in low impact velocities [68]. Other researchers studied later dynamics of droplet impact including smooth spreading and splashing threshold [93, 100], substrate surface temperature [18], rebound [82], the surrounding gas effect [73, 124], and the effect of viscous forces [106].

There have been theoretical and computational studies in the field as well. Hicks and Purvis [53] and Hendrix et al. [51] theoretically modeled the air layer thickness and the size of entrapped bubble. Mandre et al. [87] studied the lubrication equation and gas compression under higher speed droplet impacts. Duchemin and Josserand [42] solved the lubrication equations in the air layer for its drainage dynamics. The problem has been investigated by means of molecular dynamics (MD) simulations [26], finite element modeling [23], combined finite element/difference based on continuum mechanics that captures liquid viscous effects [90]. Notably, Chubynsky et al. [23] incorporated the gas kinetic effects (GKE) in the nano-metric air layer and took into account the important van der Waals forces between the liquid and solid.

1.1 Droplet Bouncing

The physical setup considered throughout this work is a drop of liquid falling towards a flat solid surface in the presence of a surrounding gas (air). As the liquid drop falls towards

^IThis will be revisited in the current work.

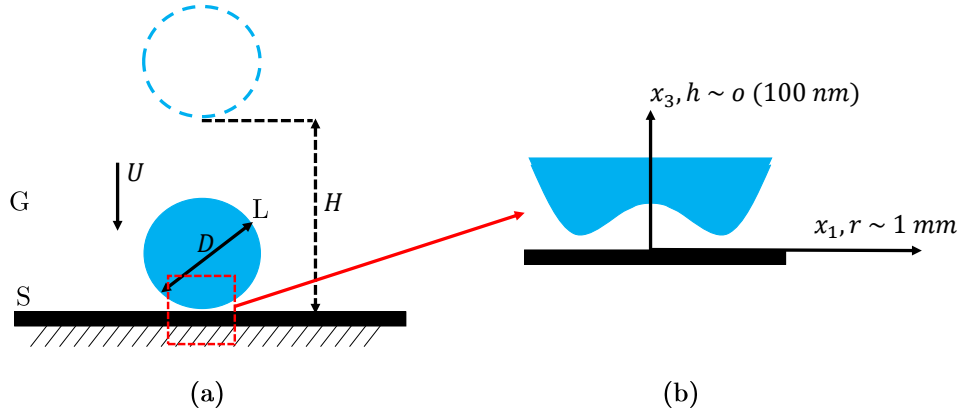


Figure 1.1: a) A liquid droplet (L) of $D = O(1\text{mm})$ diameter is falling from the height H towards solid substrate (S) surrounded by ambient air/gas (G). b) An exaggerated view of the region underneath the droplet just before the contact initiation where the air forms a lubrication layer with nanometric thickness and creates a dimple shape in the droplet bottom profile.

the solid surface, it interacts with the surrounding gas. The drop is initially spherical, with diameter D , falling towards a horizontal solid surface (S) at uniform vertical velocity U as shown in Fig. 1.1.a. The gas is initially at uniform atmospheric pressure, P_{atm} . We use the subscripts L and G to refer to the liquid and the gas, respectively, and 0 denotes the initial conditions. The liquid–air interface begins to deviate away from the substrate surface even before the droplet comes into contact (Fig. 1.1.b). We designate the liquid viscosity by η_L , its surface tension by γ_L , its density by ρ_L , and its kinematic viscosity by $\nu_L := \frac{\eta_L}{\rho_L}$. We assume that the fluid/solid configuration to be isothermal way below the liquid boiling temperature, with gravitational acceleration, g . We assume a rigid substrate with no free vibration or deformation forces. We characterize the configuration geometry by a characteristic length, D , the diameter of a droplet.

The flow on the scale of the experiment can be parameterized with Capillary number ($Ca := \frac{\eta_L U}{\gamma}$) which gives the ratio of viscous pressure to surface tensions; the Reynolds number ($Re := \frac{\rho_L U D}{\eta_L}$) which provides inertial/viscous forces; Weber Number ($We := \frac{\rho_L D U^2}{\gamma}$) giving inertia forces/surface tension ratios; and Bond number ($Bo := \frac{\rho_L g D^2}{\gamma}$) for gravity/surface tension. Another useful non-dimensional parameter is Ohnesorge number ($Oh := \frac{\eta_L}{\sqrt{\rho_L \gamma D}}$) which is the ratio of inertia-capillary to inertia-viscous time scales or viscous forces

$$\frac{\eta_L}{\sqrt{\rho_L \gamma D}} = \frac{\eta_L U}{\gamma} \frac{1}{U} \frac{1}{\sqrt{\rho_L \gamma D}} = \frac{Ca}{Re} \frac{1}{\sqrt{\rho_L \gamma D}}$$

Spring bounce: First consider the droplet impacts with U 's large enough for the droplet to easily break through and push away air film and make contact with a non-wetting solid substrate. The rebound can happen via a spring-like process through interactions between the liquid and solid surface. Upon impact, the droplet spreads radially (due to

Table 1.1: The regime of parameters used in the experiments of the current work.

Parameter	Description	Magnitude	Units	Remarks
D	Droplet diameter	$O(10^{-3})$	m	
U	Impact velocity	$O(10^{-1} - 10^0)$	m/s	
ρ_L	Density of liquid	$O(10^3)$	kg/m ³	
ν_L	Kinematic viscosity of liquid	$O(10^{-6} - 10^{-4})$	m ² /s	
γ_L	Liquid surface tension	$O(10^{-2})$	Pa.m	
P_{atm}	Initial gas pressure	$O(10^5)$	Pa	Used for air
ρ_G	Density of gas	$O(1)$	kg/m ³	
η_G	Dynamic viscosity of gas	$O(10^{-5})$	Pa.s	
k_G	Heat specific ratio	$O(1)$	-	

inertia) until it reaches a maximum extent [47, 48], then recoils (due to surface tension) through a Taylor-Culick type retraction [33], and eventually may bounce off in an elongated shape perpendicular to the surface [1, 61]. The expansion/retraction cycle of the drops is reminiscent of springs, where inertia and elastic forces similarly conspire to generate oscillations. However, in our everyday experiences we observe that in many cases bouncing is suppressed: droplets that are not too heavy or too viscous bounce off. Drops larger than their gravito-capillary length ($L_{Ca} := \sqrt{\frac{\gamma}{g\rho_L}}$) do not rebound [5] and further, there exists a critical liquid viscosity, beyond which the droplets do not bounce off neither [57]. The spring-like rebound can be described as conversion of the surface energy of the spread liquid into kinetic energy while gravity and viscous stresses hindering the process [104]:

- Drops smaller than their visco-capillary length ($Oh > 1$) cannot bounce due to viscous dissipation
- Drops larger than their gravity-capillary length ($Bo > 1$) cannot bounce due to their weight.

Air cushion bounce: Above summarizes the “liquid-solid contact regime” rebound on hydrophobic surfaces. However, there exists a bouncing regime off wetting substrates which is a fascinating interaction. The experimental evidence of complete rebound [28, 29, 68] of the drop from a hydrophilic surface points to “liquid-air cushion regime” bounce. In this regime bouncing occurs without the liquid ever meeting the solid and there is a nanometer-scale film of air that separates the liquid and solid. The lubrication dynamics within the air layer conspire against the inertia of the liquid droplet seeking contact with the solid substrate, and during the rebound, the shear in the air film is the dominant source of dissipation [68].

In the majority of the experiments in the present work, we consider the impact velocities around the threshold of “liquid-air cushion regime”, *i.e.*, between 0.5-0.7 m/s. This

corresponds to an impact Weber number with a range of 10.4 – 27.8, calculated based on the droplet diameter. Relevant initial conditions, physical properties, and other characteristic parameters are listed in Table 1.1. We use solutions of water and glycerol to obtain fluids with viscosities ranging from 1 to 100 cSt (See Chapters 2 and 5). When studying the air film instability and surface forces in Chapter 4, we experiment with both silicon oil and water-glycerol solutions of similar viscosity, *i.e.*, 10 cSt but in a wider impact speeds range, 0.37-0.91 m/s. We carry out all the experiments in the room temperature with air as the gas medium.

For the substrate, we consider flat borosilicate crown glass (n-BK 7) with surface polish quality of 40-20 Scratch-Dig in Chapters 2 and 5. In Chapter 4, where we aim to eliminate the substrate surface roughness effects, we use muscovite mica sheets. A mica slab can be easily cleaved through its thickness, obtaining an atomically flat surface over several millimeters^{II}. Furthermore, mica has benefits of being chemically stable, inert to most liquids, transparent, and with high tensile/shear stiffness. One disadvantage is that mica is birefringent, which complicates FTIR microscopy method that we address in Chapter 3. Also after cleaving, the mica surface carries electrostatic charge.

1.2 Low Speed Impact Dynamics

The continuity equation of a continuum medium and the incompressible Navier–Stokes equations govern the liquid motion,

$$\frac{\partial u_{L_i}}{\partial x_i} = 0 \quad (1.1)$$

$$\frac{\partial u_{L_j}}{\partial t} + u_{L_i} \frac{\partial u_{L_j}}{\partial x_i} = -\frac{1}{\rho_L} \frac{\partial p_L}{\partial x_j} + \nu_L \frac{\partial^2 u_{L_j}}{\partial x_i \partial x_i}, \quad (1.2)$$

where u_i and p denote velocity and pressure field, respectively and we employed Einstein's summation convention. Dynamic wetting mediated by air is a three-phase phenomenon by nature. The dynamics prior to the initiation of contact has not yet been conclusively determined. It is controlled at first by formation and then the drainage of the thin air layer. We simplify the equations using two-dimensional Cartesian coordinates (x_1, x_3) .

In the air layer formation regime, the axisymmetric lubrication equation is applicable in the gas medium because the air film thickness (h), is much less than the film radius [117]:

^{II}This is a subject of debate. There are experimental evidences showing immediately after cleaving a reaction between the mica, atmospheric CO₂ and water occurs [22]. However, the mica surface would only be covered by up to one formula unit of K₂CO₃ per nano-metre which is mobile in humid conditions, and crystallizes under drier conditions.

$$\frac{\partial(\rho_G h)}{\partial t} = \frac{1}{12\eta_G} \frac{\partial}{\partial x_1} \left(\rho_G h^3 \frac{\partial p_G}{\partial x_1} \right), \quad (1.3)$$

where

$$h := h(x_1, t), \quad (1.4)$$

and no-slip boundary conditions are assumed [85]. Introducing the shear stress, τ_{ij} , we write the following boundary conditions. The stress boundary conditions at the liquid-gas interface dictate

$$\tau_L(x_1, h, t) = \tau_G(x_1, h, t) \quad (1.5)$$

and the Laplace condition for pressure,

$$p_L = p_G + \gamma_L \frac{\partial^2 h}{\partial x_1^2}. \quad (1.6)$$

Far enough away from the axis of impact, the pressure in the gas is the ambient pressure,

$$\lim_{x_1 \rightarrow \pm\infty} p_G(x_1, t) = P_{\text{atm}}. \quad (1.7)$$

The problem has symmetry about $x_1 = 0$ which gives

$$u_{L_1}(0, x_3, t) = 0, \quad (1.8)$$

$$\frac{\partial u_{L_1}}{\partial x_1}(0, x_3, t) = 0 \quad (1.9)$$

for the liquid medium and

$$\frac{\partial h}{\partial x_1}(0, t) = 0, \quad (1.10)$$

$$\frac{\partial p_G}{\partial x_1}(0, t) = 0 \quad (1.11)$$

for the gas.

The above system of equations, closed with boundary conditions, can be numerically

integrated in time with a reasonable initial condition [90]:

$$h(x_1, 0) = h_0 + \frac{x_1^2}{D} \quad (1.12)$$

where h_0 is the initial height of the center of the interface and

$$u_{L_3}(x_1, x_3, 0) = -U, \quad (1.13)$$

$$u_{L_1}(x_1, x_3, 0) = u_{L_2}(x_1, x_3, 0) = 0 \quad (1.14)$$

are the velocity initial conditions.

In the drainage regime with low speed impacts, inertia can be neglected resulting the liquid pressure field that simply compensates the drops weight. In this regime, the lubrication dynamics of air layer prevents mathematically the rupture of the film in a finite time duration [41]. Hence, the finale of this regime needs to involve additional physical mechanisms that trigger the instability and rupture of the air film. As Duchemin and Josserand [42] call them, usual suspects include surface roughness, van der Waals interactions, and thermal fluctuations. We will get to them and also electrostatic interactions in Chapter 4 and 6.

In both the air layer formation and drainage regime, the gas compressibility can be ignored as $U < 1$ m/s. However, in the air drainage regime, the above lubrication theory ceases to be valid as soon as the air layer thickness becomes slender. As we show in Chapter 4, this is determined by Knudsen number, $Kn := \frac{\lambda_G}{h}$, where the gas free mean path for air is $\lambda_G \approx 70$ nm. Firstly, the classic lubrication theory shall incorporate the rarefied gas effect [23] and also the no slip assumption no longer holds [85]. Experimental data are required to validate the GKE parameters available in the literature. Secondly, the boundary condition shall include additional short-range forces in the normal direction. We can capture these effects by adding additional normal stress

$$p_{sr} = p_M + p_{vdW}, \quad (1.15)$$

on the droplet boundary bordering the air film, *i.e.*, left hand side of Eq. (1.6); where p_M and $p_{vdW} = -\frac{A_H}{6\pi h^3}$ are Maxwell's stress and disjoining pressure (van der Waals contribution), respectively. Without these data the system of governing equations are incomplete.

Analysis of the air film rupture can provide insight into the mechanisms responsible for air film instability and the transition to contact. Thermodynamically, the free energy change (ΔG) associated with the wetting of substrate surfaces by the liquid is given by

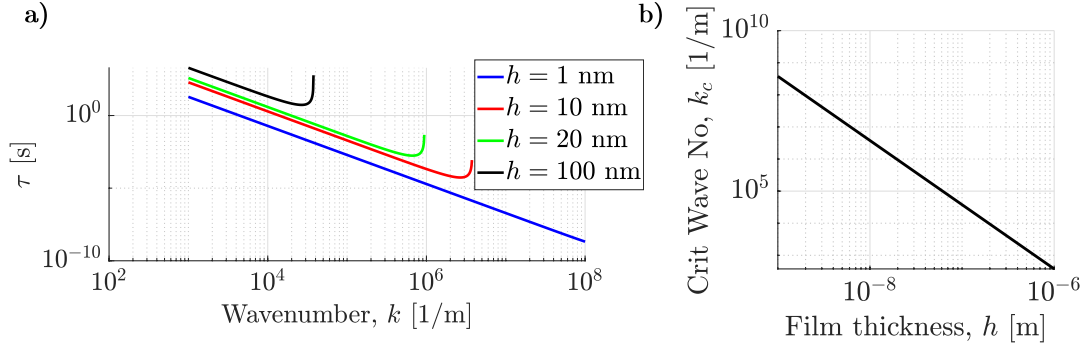


Figure 1.2: Results of linear stability analysis. a) The critical time at which the air film loses stability is plotted as a function of wavenumber k values of the film thickness h , as shown in the colored lines labeled in the legend. b) The critical wave number k_c scales inversely as the square of h for fixed values of the Hamaker constant $A = 3e - 19$ J and 10 sSt silicon oil surface tension $\gamma_G = 0.022$ Pa/m.

Young-Dupre's equation [46]

$$\Delta G = -\gamma_{LG}(1 + \cos(\theta)), \quad (1.16)$$

where γ_{LG} and θ are interfacial tension between liquid-air and the liquid contact angle on the solid surface, respectively. ΔG becomes more negative by decreasing the substrate hydrophobicity, *i.e.*, increasing $\cos(\theta)$. The liquid-air interface beneath the droplet is inherently unstable by nature of the interfacial attraction between the liquid and a hydrophilic surface. Indeed, there is a strong attraction between the liquid and the solid, driven by interfacial forces, which are in 'competition' with surface tension - that acts to keep the interface flat.

Mechanically, the onset of the wetting occurs when the gradient of the interaction force overcomes the effective elastic constant of the liquid free surface which is proportionate to surface tension of liquid [2, 16, 56]. Prior to air layer rupture, the surface tension is in balance with the interaction forces, p_{sr} . When the attractive force exceeds a critical value, the air film ruptures and the wetting begins [45]. In the absence of Maxwell stresses (electric charges), the growth rate for the interfacial instability is given by [13]:

$$\frac{1}{\tau} = \frac{k^2 h^3}{3\eta_L} \left(\gamma k^2 - \frac{A}{2\pi h^4} \right). \quad (1.17)$$

Here, $k = 2\pi/\lambda$ is the wave number of the instability, where λ is the wavelength; and h is the steady-state film thickness. This is based on a linear stability analysis and A is the modified Hamaker constant with GKE effects [23]. If $\tau < 0$, any disturbance on the liquid-gas surface grows. The sign of the term in the brackets provides a critical wave number (k_C) for when we expect the film of thickness h becomes linearly unstable.

The stability of the air film can then be assessed for different values of h and k . The time constant for linear instability is seen to decrease strongly as a function of wave number for several different values of h , as shown in Fig. 1.2.a. For fixed A and γ , the critical wave number is a strong function of the film thickness, and scales as $k_C \propto 1/h^2$, as can be seen in Fig. 1.2.b.

In this work, we show that the air film ruptures at a closest approach distance (h^*) of below 100 nm, when the total interaction forces are attractive and sufficiently strong to trigger the liquid contact on the substrate. We develop accurate experimental techniques that capture film thicknesses of $o(100)$ nm and use fast imaging to directly observe the air layer formation, drainage, and rupture. Our database can be used to verify the short-term force estimations and GKE effects.

1.3 Outline of this Manuscript

Chapter 2 introduces the imaging modalities used in this work, namely, frustrated total internal reflection (FTIR) and Fizeau Interferometry (FIF). We address the challenge with regard to the trade-off imposed between the imaging temporal rate and spatial resolution. We propose and implement a framework based on machine learning, *i.e.*, deep neural networks. We implement the method in its entirety on high-speed imaging profilometry data acquired in the study of droplet impacts on a smooth, solid surface, and is used it to recover full, high-resolution images. In the remaining chapters of this thesis, the machine learning-enabled part of the imaging system is not utilized providing a more direct observation of the physical system and first-hand measurements of the impact dynamics.

The mapping of the aforementioned images to the target physical parameters is the subject of Chapter 3. We explain the way the recorded images and light intensities from underneath the droplet are used to obtain 4D profilometry data. We calibrate the FIF and FTIR microscopy modalities and show that they are suited to measure air layer profile with error bars as small as few nanometers.

Chapter 4 is dedicated to the physics involved right before the wetting or droplet bouncing occurs. We experimentally investigate the air layer formation, its thinning/drainage and instabilities. Further, we discuss the interaction forces between the liquid droplet and the solid substrate across the thin layer of air.

In Chapter 5, we study the early stage of wetting beneath the droplet on a glass substrate. We consider a special contact initiation mechanism through nucleation. We experimentally probe the liquid bridge expansion, air accumulation, the deformation of the liquid-air interface, and the formation of the capillary wave ahead of the advancing wetting front. We explain how the capillary wave is regularizing the pressure at the advancing wetting

front and the anomalously low velocities of the dynamic contact line under the droplet.

Lastly in Chapter 6, we summarize the major contributions of this dissertation and outline the possible future directions of our research that can be appraised.

2 Interface Imaging & Resolution Enhancement with HOTNNET

Myriad applications of imaging involve rapid phenomena [24, 102, 126, 137]. In the studies of these phenomena, a trade-off between spatial and temporal resolution is imposed by the data bandwidth of typical high-speed camera hardware - we can obtain a pixel-dense image at low imaging rates, or low-pixel count images at high-rates, but we cannot obtain high pixel-count images at the highest frame rates without specialized techniques [36]. In addition to this technical constraint, physical phenomena such as optical diffraction or the finite numerical aperture of the image-forming objective also restrict spatial resolution. These limitations impede our ability to resolve rapid and multi-scale phenomena.

For rapid and multi-scale interfacial phenomena, interferometric imaging is often used as a means of visualization. This imaging modality has numerous applications in scientific and engineering fields, ranging from contact mechanics [60], fluid interfacial phenomena [27, 32, 35, 125, 136], biotechnology [108], nanotechnology [66], astronomy [92] to more industrial sectors like semiconductor [123] and display industries [78]. Interferometric imaging has the added benefit that it can be used as a non-invasive optical measurement technique. With interferometric imaging, the information about the target physical quantity is encoded in a two-dimensional fringe pattern, where the intensity of the fringes indicates the optical interference at a given spatial location within the image. This introduces a problem of lost phase information, leading to ambiguity in the interpretation of the interferogram; the ambiguity of the phase is only resolved in a process called demodulation. The demodulation process can limit the precision and accuracy of the measurement and requires a large field of view to work effectively.

This majority of the material in this chapter appeared in Exp Mech as Kaviani, R. and Kolinski, J. M. (2022). High resolution interferometric imaging of liquid-solid interfaces with HOTNNET. *Exp Mech*, 63(2):309-321.

Authors' Contributions R.K. and J.M.K. conceived the project. R.K. developed the neural network and implemented the code for pre-processing and processing the data under the guidance of J.M.K. R.K. and J.M.K. interpreted the results. R.K. and J.M.K. equally contributed to writing the manuscript.

Interferometry is often used in measurements of deformation during contact to obtain precise information about the gap between adjacent surfaces via interfacial profilometry; these measurements provide insight into material displacement, and can characterize material response due to mechanical loading or wear. As a result of the small spacing between adjacent surfaces, contact phenomena can occur on fleeting timescales; thus the problem of insufficient imaging resolution renders the aforementioned challenge of interferogram demodulation very difficult indeed. For fast interfacial dynamics, the limitations of high-speed imaging require that spatial resolution is reduced, or the field of view is shrunk, to obtain the necessary temporal resolution; however, any sacrifice of resolution or field of view can impair the demodulation effort by blurring or decreasing the fringe resolution. Even for slow or stationary interfacial profilometry, surface discontinuities, sharp interface changes and high slopes in the profilometry can degrade the fringe contrast [132] which makes it challenging to use interferometric optical techniques in nano-scale surface topographies [127].

Within the domain of contact mechanics, droplet impacts exemplify the rapid phenomena that can occur at an interface. Many experiments on droplet impacts use interferometry to directly visualize the contact profile and also the air gap between a liquid and a flat smooth substrate during impact [38, 79, 83]. Interferometric fringes can be demodulated to reveal the three dimensional profile of the air layer beneath the impacting drop, with a trough-to-peak resolution of approximately 150 nanometers between the dark and bright fringes. In these studies, however, absolute measurements of the air gap can only be obtained through more technically advanced implementations, such as white-light interferometry [125] or two-color techniques [30, 31], and require additional hardware and processing.

We address this imaging challenge using deep convolutional neural networks (DCNN) to obtain accurate and absolute values of the target quantities, while bypassing the need for explicit interferometric phase unwrapping. DCNNs were recently used to recover cohesive properties in the context of dynamic fracture mechanics from experimental interferometry images [59] in a manner similar to our recovery of FTIR imaging data from interferometric imaging data. Here, we exploit the proven ability of DCNNs [97] to obtain a super-resolved image from a low-resolution counterpart in the study of droplets impacting on a glass surface. Our DCNN, adapted from Visual Geometry Group (VGG) deep convolutional network [103], simultaneously demodulates the interferometric fringe patterns and maps them to target quantities. This builds upon recent efforts to use neural networks to unwrap the phase of interferometric fringes [7, 80, 139], that show better accuracy [43] and robustness [77] than approaches like phase shifting [141] and spatial phase demodulation methods [115].

A set of images recorded during the droplet impact experiments comprise the DCNN training database. We image the entire spatial extent of the droplet impact interface with an interferometric modality using a large field of view. Concurrently, we employ

a frustrated total internal reflection (FTIR) microscopy modality to image a narrow sub-region of the interface at a higher resolution, producing the absolute target quantities. We then crop the interferometry images and the FTIR images to the common sub-region, thus forming the data pairs used to train and test the DCNN. Once trained, the network then maps all the other sub-regions to high resolution data; these upscaled subregions are then assembled via a high-order overset image reconstruction technique [110] for the entire sequence of low-resolution interferometric images. The hybrid processing framework, consisting of the High-order OverseT assembly method and the deep convolutional Neural Network (HOTNNET), produces demodulated, super-resolved images on a large field of view. We can then use a nanometer-precise, closed-form mapping function (see Section 3) to treat the HOTNNET output, thus obtaining accurate, absolute measurements with improved resolution along all directions, with accuracy of the order of the sub-fringe thickness resolution obtained with two-color interferometric imaging methods [29].

2.1 Imaging Setup

A 1.6 mm diameter drop of water-glycerol solution was released from a syringe luer adapter, and impacted on a smooth glass surface, as shown in Fig. 2.1.a at top. The droplet viscosity in each experiment was selected from 8 different viscosities in the range of 1 to 100 centi-Stokes. Impact velocity was controlled by releasing the droplet from among 5 different fall heights, H , varying from 12.5 to 24.5 mm. At each height, all viscosities were tested once; thus, in total, 40 impact experiments were conducted. Prior to liquid-solid contact initiation, a nanometer scale air film forms between the droplet and the glass surface. The initial thickness of this air film varies inversely with impact velocity, from approximately 300 nm to tens of nm [68]. The liquid-solid-air interface was simultaneously imaged with two independent optical measurement techniques: FTIR and Fizeau Interferometry (FIF). These data were used in reports on the lift-off instability beneath an impacting droplet (see Section 5 and [69]).

In the FTIR method [68–70, 102], the top surface of an optically smooth dove prism (BK-7 glass) is illuminated with collimated light, aligned to be incident at an angle greater than the critical angle for total internal reflection at a glass-air interface, but smaller than the critical angle at the glass-liquid interface. This light excites an exponentially decaying evanescent field above the prism’s surface, and when the liquid droplet enters within a few decay lengths of the surface, some light is transmitted to the droplet, and the intensity of the reflected light reduces. The proportion of light transmitted to the drop increases as the droplet gets closer to the surface, further reducing the reflected intensity. The reflected light is imaged onto a high-speed camera sensor using a long-working distance (Mitutoyo 5X) microscope objective. The normalized light intensity is directly related to the air layer thickness by a deterministic transfer function, which varies with the incident light polarization, as described in in the next Chapter

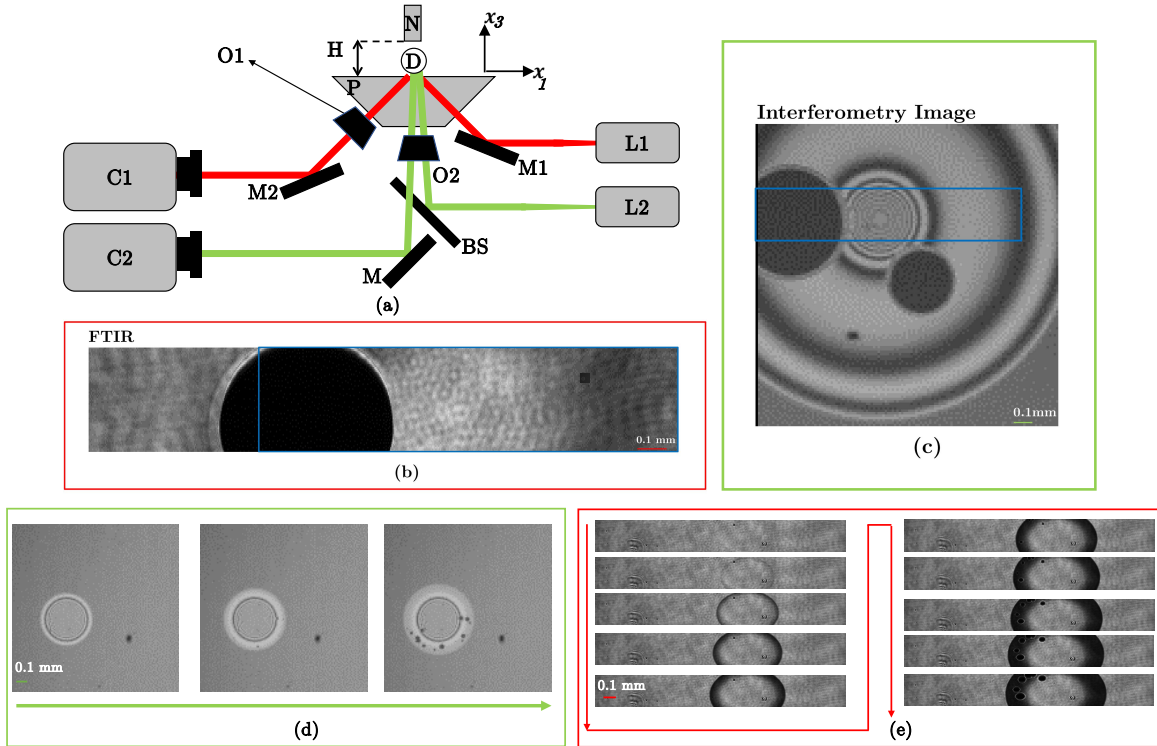


Figure 2.1: The experimental schematic and representative images. (a) The 1.6 mm diameter drops of water-glycerol solution fall from the height H from the nozzle (N). Light emitted from a Thorlabs HNL150LB HeNe laser (L1) illuminates the Dove prism (P) upper surface and totally internally reflects from the glass-air interface directly beneath the impacting droplet and is captured by camera C1 after exiting from the prism and passing through a dry 5X Mitutoyo microscope objective (O1). Fizeau interferometry data is acquired with the independent light path from a Thorlabs M530L2 green LED light source (L2) that is collimated and goes through the beam splitter (BS) and is captured on sensor C2 through another dry 5X Mitutoyo microscope objective (O2). C1 and C2 are Phantom V711 and Phantom V7.3 fast cameras, respectively with tube lenses. They record at 180,000 and 90,000 frames per second, respectively, and are simultaneously triggered externally using an analog signal for each droplet impact experiment. Mirrors (M, M1 and M2) are used for light path alignment. Two example images of the thin air film during contact initiation beneath the droplet: FTIR image (b) and Fizeau interferometry fringes image (c). The FTIR image is stretched by a factor of $\sqrt{2}$ in the x_2 direction (see Section 3) to account for the oblique illumination angle, thus unifying the scale of the major and minor axes of FTIR images. The interferometric image recovers a larger region on the surface. The surface region sampled by both imaging methods simultaneously is shown by a blue rectangular box which has a height and width of 0.35 mm and 1.42 mm, respectively. (d) and (e) show the rapid nature of contact initiation. Onset of wetting is mediated by the formation and growth of nanoscale liquid bridges, binding the liquid to the solid through a thin film of air. FTIR imaging modality better resolves the fleeting time scales where the contact initiates but on a narrower field of view.

The interferometric method requires a second optical path. In this approach, collimated light is directed onto the optical path using a 50-50 beam-splitter and focused onto the impact surface. When the droplet enters to within the coherence length of the light, an optical cavity is formed between the droplet surface and the solid surface. Some of the light reflects from the solid-air interface; a smaller amount of the transmitted light then reflects from the air-liquid interface. Depending on the gap thickness between the solid and the liquid, these two reflected beams will interfere [31, 39]. The interference between the two reflected beams from the spatially varying gap results in a pattern of fringes that are subsequently imaged onto a second high speed camera sensor. Both FTIR and FIF optical configurations are depicted in Fig. 2.1.a. Alignment of the optical paths and robust optical mounts were used to ensure image registration fidelity along the 40 experiments.

Simultaneous FIF and FTIR imaging is used in recent interfacial mechanics studies to probe the liquid-air interface beneath an impacting droplet [19, 94, 95]. These imaging modalities provide complimentary information about the liquid-air profile at different scales and with different resolutions - FTIR can resolve up to the wavelength of light with exponentially increasing resolution as the droplet approaches closer to the surface, whereas FIF can be used to measure gaps of up to several microns with lesser resolution. During simultaneous imaging, FTIR provides a reference for absolute measurement of the liquid-air interface with FIF; however, this doesn't remove the need for FIF fringe demodulation.

In our simultaneous FIF and FTIR imaging setup, the FIF imaging path corresponds to a larger physical region extending over the entire impact zone beneath the droplet; by contrast, the FTIR modality images a smaller region near the impact axis with greater magnification. The common region recorded by both imaging methods is shown by a blue rectangular box in Fig. 2.1.b & c. The FIF images comprise 128×128 pixels at a resolution of 12.7 microns per pixel in x_1 and x_2 directions with a precision of about one micron in the x_3 direction. The FTIR images comprise 512×64 pixels at a resolution of 3.8 by 5.0 microns per pixel in the x_1 by x_2 directions. FTIR resolves the gap thickness to within 10 nanometers in x_3 direction [67]. FTIR and FIF images are recorded at 180,000 and 90,000 frames per second, respectively; example images are shown in Fig. 2.1.b-c. The sequence of images shown in Fig. 2.1.d-e shows the rapid nature of contact formation.

2.2 Deep convolutional neural network

We developed a deep convolutional neural network that maps our FIF images to our FTIR images. The network we employed [64] is adapted from the EnhanceNet neural network [103].

Similar networks have proven to be a robust tool in numerous applications in the field of

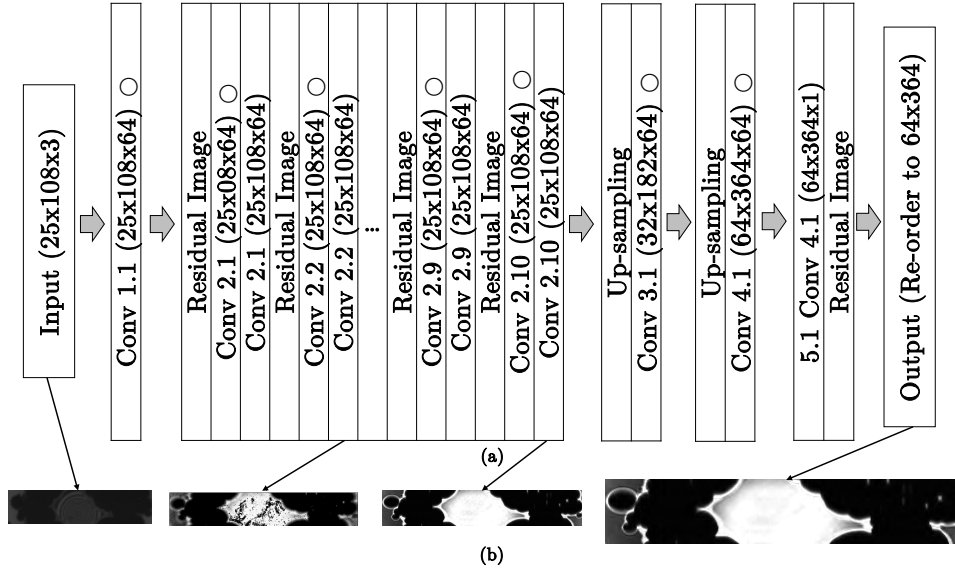


Figure 2.2: The architecture of the network employed in this work. The network implicitly performs unwrapping of the input interferometry fringes, up-sampling the data to a higher spatial resolution, and improves the signal to noise ratio at the same time. (a) All the convolutional layers employ a stride of a size (3×3) . The \circ symbols on the convolutional layers indicate Rectified Linear Units (Relu) activation. (b) In the first few convolutional layers the outline of the grayscales are determined. In the other words, the network distinguishes which stage of contact dynamics are being taught the network. The FIF images are enlarged in the figure and not to be scaled.

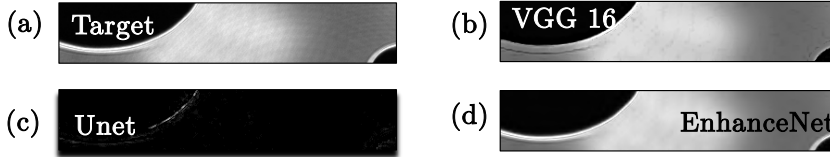


Figure 2.3: Performance of different neural networks on a test image (a) Target FTIR data (b) VGG-16 output after 1250 epochs (c) U-Net output after 2000 epochs (d) Our Modified EnhanceNet result after 800 epochs. VGG-16 output diffuses the sharp profile applies a filtering operator on sharp edges. Our attempts for U-Net network training have been unsuccessful and led to divergence. EnhanceNet shows a faster convergence rate and was superior in capturing the profile of the contact line.

data science whenever information is abundant [34, 75], and there is considerable interest in using these networks in engineering applications [37, 54, 59]. The structure of our network is detailed below and is available online [64].

We developed a deep convolutional neural network that maps our FIF images to our FTIR images. The network we employed [64] is adapted from the EnhanceNet neural

network [103], consisting of several interconnected layers, as depicted schematically in Fig. 2.2.

The EnhanceNet is a generative feed-forward fully convolutional network [103], derived from Visual Geometry Group (VGG) deep neural network [112], using strided convolutions but with leaky ReLU activation and without pooling layers. Our network uses an Adam optimizer with a learning rate of 0.0005 to minimize the mean square error cost function. Our goal was to achieve normalized root mean-squared error of order $O(10^{-6})$ in the interior of the images (see the discussion section 2.5) which is 2 orders of magnitude smaller than the error on edges, *i.e.*, $O(10^{-4})$.

With this metric, we found the EnhanceNet perform better in comparison with similar upsampling and convolution networks in terms of capturing the contact line (Fig. 2.3). Different networks were implemented using the TensorFlow version 1.14 Python library and was run on an NVIDIA Tesla T4 graphics processing unit. Our DCNN has shown better accuracy and an increased rate of convergence compared to GAN and U-Net. It took our modified EnhanceNet training 800 epochs over a course of 9.5 hours runtime to satisfy the convergence criterion. This was faster and more efficient compared to the original EnhanceNet and the VGG-16 architectures taking over 2400 and 4000 epochs with runtime period of each over 24 hours, respectively. Due to the fine structure of the liquid-solid contact line, as many training epochs were required for the network to achieve reproducibility of these dynamics. Our attempts for U-Net architecture training have been unsuccessful (Fig. 2.3.c). We used batch shuffling of the training data set with a drop-out ratio of 12 percent was used to avoid over-fitting.

To train the network, we generate input-output data pairs from the images recorded during the impact experiments. Prior to training, the images are treated with a pre-processing protocol. First, the FIF images are interpolated in time using a quadratic interpolation function in order to synchronize the FTIR and FIF images. This yields a total of 14871 time synchronized frames from the 40 droplet impact experiments. Second, the data from the common region indicated by a blue rectangle in Fig. 2.1.b-c are denoised and cropped from the images. The dimensions of the FIF and FTIR images are reduced to 25×108 and 64×364 pixels, respectively. Third, from each FIF-FTIR pair, 3 additional data pairs are generated by mirroring the images on x_1 , x_2 , and $x_1 - x_2$ axes which increases the number of data pairs to 59484. As the final step, instead of pairing the FIF-FTIR images on a 1 to 1 basis, the input FIF data is augmented by 2 FIF frames, one before and one after the target time step, resulting in the pairing of 3 successive FIF images to 1 FTIR image; yielding data pairs with dimensions $3 \times 25 \times 108 \Rightarrow 1 \times 64 \times 364$. The sequence of 3 FIF frames provides additional information to the network, facilitating the interferometric signal phase unwrapping and better capturing the dynamics of the liquid-air interface.

The total data pairs were split into 2 pools: the first pool consists of 32 impact experiments;

images in this pool were used for both training/validation and testing purposes. The second pool consists of 8 separate droplet impact experiments; these images were used entirely for the final testing of the network performance. To train the network, 12000 and 2000 data pairs were randomly drawn from the first pool to assemble the training and validation data sets, respectively. The testing data set for the network consists of the remaining of data pairs from the first pool, and all the pairs in the second pool. In total, 45484 data pairs that the network did not see during the training were used to test the network’s performance. Out of these testing set, 12395 pairs were from the second pool which were entirely left out during the network training. The root mean square error on all pixels averaged on 45484 images is in order of 10^{-6} , as shown in Section 2.5.

There are four key stages of the droplet impact process, where the images appearing in each stage are somewhat distinctive; namely, before the contact initiation, immediately after the contact initiation, late stage of liquid-solid contact growth, and complete liquid-solid contact development. The last stage is discernible when the contact line(s) become stationary after sweeping the whole contact area and a single or multiple air bubbles might remain trapped. This stage of the impact process is distinguished by no perceptible change from frame-to-frame in the recorded images. Example network output along with the FIF and FTIR images for these four key stages is shown in Fig. 2.4. The network is able to capture the outline of the contact regions successfully at different stages of impact while simultaneously increasing the spatial resolution of the images. This “super-resolution” imaging is achieved by the network due to the higher magnification of the FTIR image. Additionally, the network enhances accuracy in the x_3 direction as a natural consequence of the elevated resolution along x_3 with the FTIR method. Thus, transforming the FIF data to the FTIR data by the use of deep learning implicitly bypasses the need for unwrapping the fringe patterns.

2.3 Mosaic mapping with overset technique

The DCNN input dimension must match the size of the data that is used to train the network [40]. Our deep neural network is trained to transform subregions of the FIF images with dimensions of $3 \times 25 \times 108$, converting them to high resolution 64×364 FTIR-like images. However, we aim to recover the entire dynamics recorded with the full 128×128 pixel field of view in the FIF image sequence. As a consequence of the mismatched dimensionality of our network input and the full FIF image, we must employ a means of using our trained network on the full FIF image despite this dimensional mismatch. Stitching the image sub-regions is commonly carried out in super-resolution imaging applications as a solution. In order to avoid losing the accuracy, we employed the overset grid technique [21, 110], which is inspired by Chimera method used extensively in high fidelity numerical simulations of fluid flows [8, 9, 63, 129]. This method breaks a discretized domain into subregions, and provides a means of connecting the subregions by enforcing high order continuity conditions in an overlapping or overset neighborhood

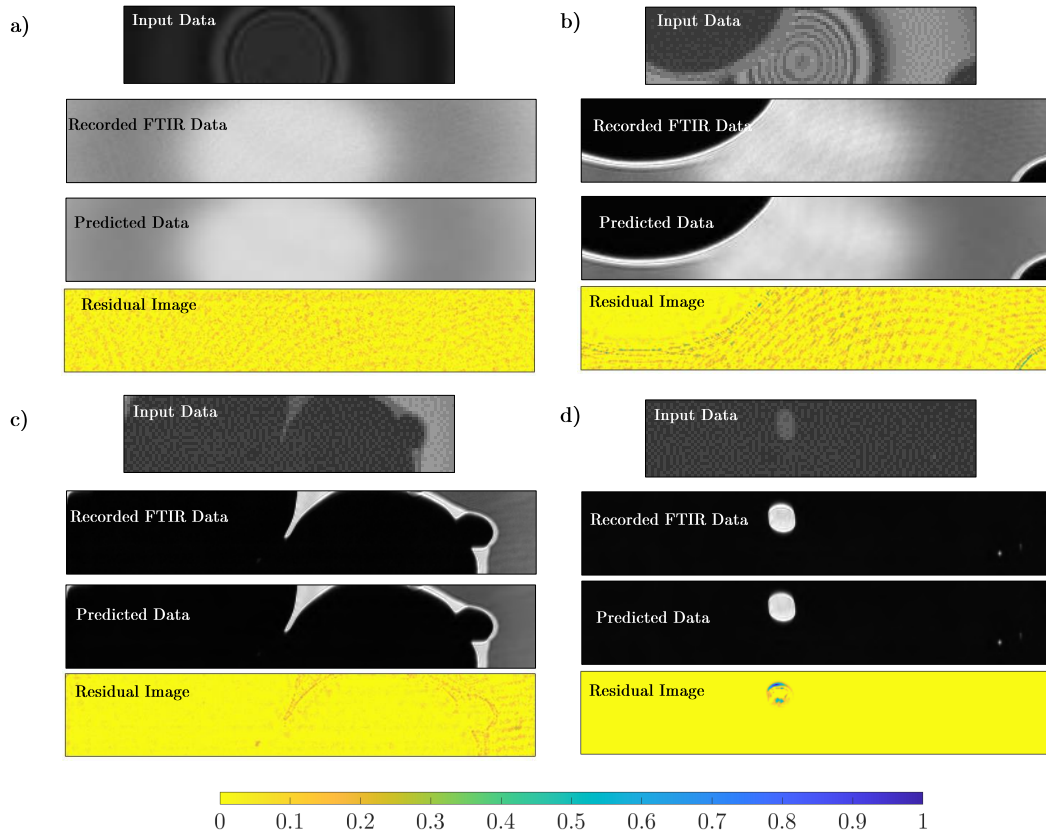


Figure 2.4: (a-d) Top: Sample of the neural network performance when applied to test images corresponding to different stages of droplet impacts. The image labeled “Input Data” is a cropped subset of low resolution (12.7 microns/pixel) interferometry imaging. The target images labeled “Recorded FTIR Data” are the high resolution FTIR image (3.9 microns/pixel in the x_1 -direction and 5.5 microns/pixel in the x_2 direction) in the same experiments but recorded with a different camera. The predicted data are the result of applying the neural network to the corresponding input data. The height and width of all images corresponds to 0.32 mm and 1.37 mm, respectively. a) Images right before the liquid-solid contact; b) Two edges meeting each other shortly after contact formation; c) Complex contact line profile moving; d) The image after the contact line has swept over the surface, and an air bubble is trapped on the surface. (a-d) bottom: The normalized residual image shown are the absolute values of difference between the target FTIR image and the DCNN network divided by a constant value of 59484. The colorbar at the bottom is for the residual images. The maximum normalized error on pixels are in the order of 10^{-4} for these images. The root mean square error (RMS) on all pixels are in the order of 10^{-6} per pixel for all 45484 test images (see Fig. 2.9). If we only consider those 12395 images which were from the 8 droplet experiments that were left out during the pre-processing stage (Section 2.2), the RMS of the error is equal to 8.3×10^{-6} per pixel.

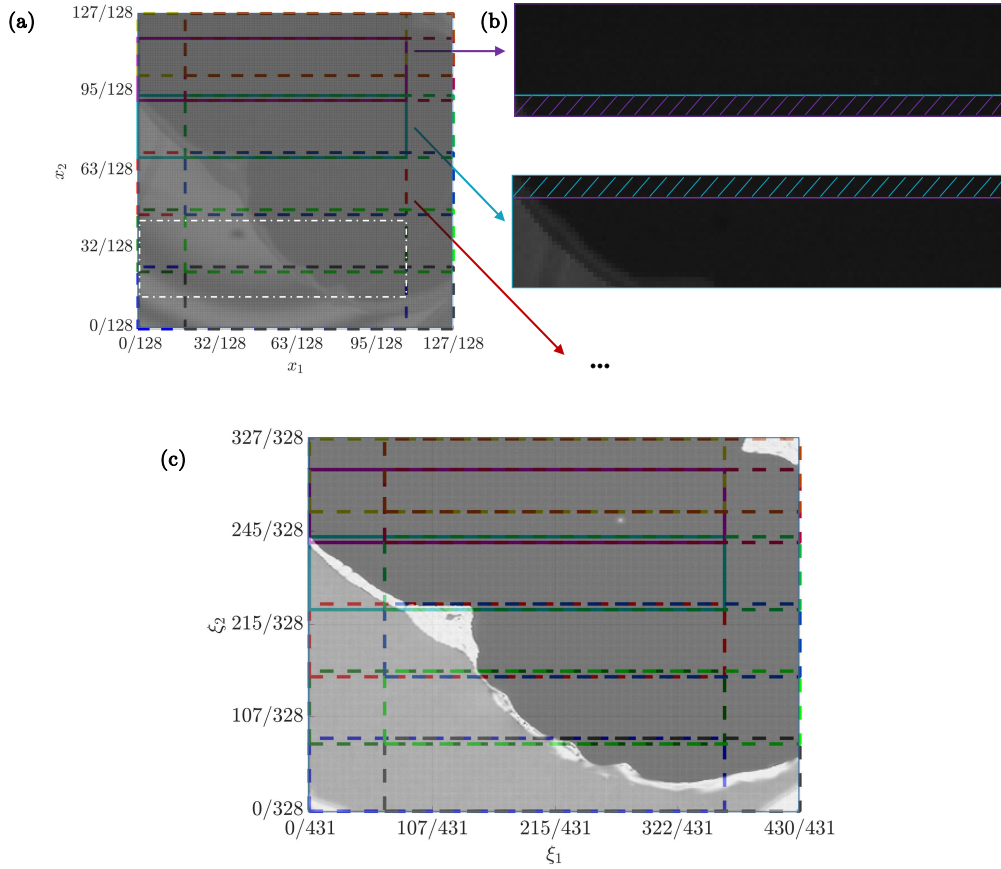


Figure 2.5: The mosaic mapping from the low resolution image (a) with 128×128 pixels to the higher resolution image (c) 431×328 . The white-outlined region near the bottom is the subset of the FIF image where high resolution FTIR data are available and is used for training the neural network. An overset grid with overlapping nodes is adapted from computational fluid dynamics [110] to partition the FIF image into subsets of appropriate dimensions for the neural network input. The subsets in the untransformed domain (a) and the mosaics in transformed image (c) are indicated by the rectangular colored outline; these comprise the unseen input and output of the trained neural network, respectively. This transformation is illustrated in (b) for 2 subdomain/mosaic pairs as an example; the arrows indicate the application of the trained neural network. The height and width the mosaic is normalized to unity with uniform node spacing in x_1 and x_2 directions to construct the interpolation stencils for the overlapping pixels as described elsewhere [64, 110]. The number of overlapping pixels introduced by hatch pattern on (b) is at least 5 in the transformed subdomain; this allows for a 6th-order Lagrangian interpolation of the neural network output.

of each subregion’s boundary.

In order to implement the overset technique, we have partitioned the FIF data where there are a minimum of 2 and 3 overlapping pixels in the “untransformed” FIF images

in x_1 and x_2 directions, respectively, which results in minimum of 5 overlapping data points in both ξ_1 and ξ_2 directions in the transformed subdomain as shown in Fig. 2.5.a. Using this partitioning we are thus breaking the entire FIF image into subregions; each of these subregions is an individual tile in the entire mosaic of the original FIF image. We can thus apply our neural network to each tile and obtain as an output a series of tiles that together form a new mosaic image representing the piece-wise mapping of the entire FIF image into a new super-resolved image. However, in order for the resulting super-resolved image to be coherent, the tiles must be connected properly. The procedure for connecting adjacent tiles in the super-resolved mosaic image is to interpolate the 2-dimensional equally-spaced coincident data points in the boundary region using a 6th-order Lagrangian interpolant [110]. The specific implementation of the interpolator stencils can be found elsewhere [64]. In this way, the subregions of the FIF data are fed one-by-one to the trained network, resulting in the high resolution mosaic shown in Fig. 2.5.b. Finally, by applying the pre-determined interpolator stencils the whole image is reconstructed, as shown in Fig. 2.5.c.

2.4 HOTNNET Results

Our DCNN can demodulate the interferometric fringe patterns and increase the data resolution of the image, as shown in Fig. 2.4. By merit of the FTIR image database used to train the network, the network also enhances the image resolution along the third axis, with some loss of depth-of-field. However, in the prior section we introduced the means to extend the use of our DCNN to the entire FIF image using the high-order overset technique. The combined workflow of first using the DCNN region-by-region with the high-order overset technique comprises a hybrid processing framework that we call HOTNNET for short. With HOTNNET, we are able to enhance the resolution across the entire field of view contained in the interferometric images.

The results of HOTNNET are shown for 3 different FIF images corresponding to 3 stages of droplet impact event in Fig. 2.6. Upon the application of HOTNNET, instead of FIF fringe patterns, the reconstructed images contain light intensities representing the air gap measurements; such an output, in principle, provides a rich database for extraction of the physics of droplet impact, with images that can be mapped onto gap measurements. The HOTNNET output no longer suffer from the 150 nanometers ambiguity in the measurement that the monochromatic FIF and its accuracy is FTIR imaging modality which is proven to have an accuracy of a few nanometers in the x_3 direction [67]. Using HOTNNET, we retain the resolution enhancement of the DCNN for each individual tile of the mosaic - the 128×128 images are up-sampled to 431×328 pixels.

Notably, any defect in the imaging system, *e.g.*, dust on the camera sensor is removed by HOTNNET as indicated in Fig. 2.6.a-c. This is likely due to the use of 3 successive frames in the network training. Even in the presence of such artifacts, the output resolution of

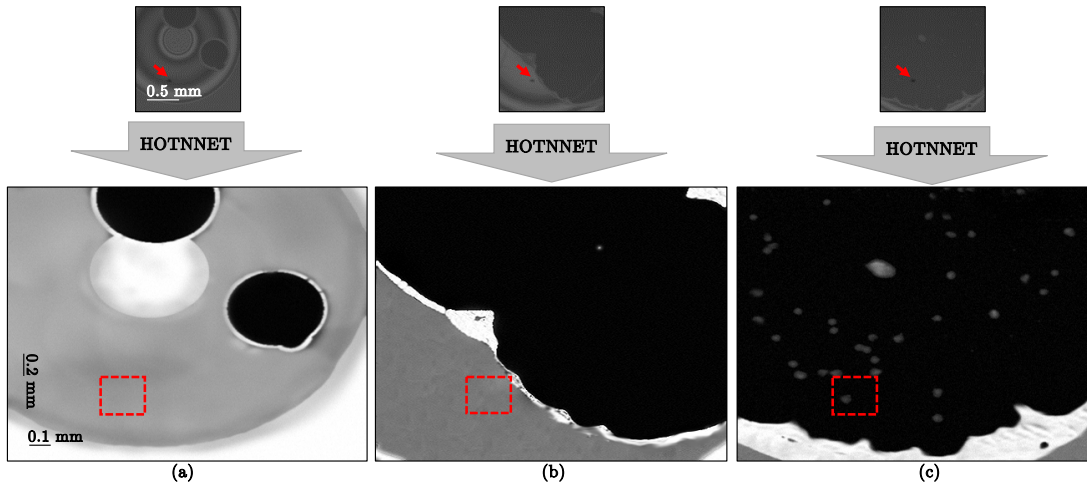


Figure 2.6: Converting low resolution FIF fringes to high resolution, easy-to-interpret, FTIR images by a hybrid overset technique-neural network (HOTNNET) (a-c). The arrows represent application of the HOTNNET framework introduced in this article, namely, untransformed image partitioning, application of the neural network to subsets, and mosaic mapping of neural network output with 6th-order interpolation at edges/-corners for assembling the high resolution image. The size of the reconstructed FTIR images (431×328) exceeds the input FIF data (128×128) by hundreds of thousands of pixels, significantly extending the spatial contents of these images. The dust on the FIF modality sensor is marked by the red arrows. HOTNNET removes this static noise from the demodulated images as indicated by red rectangles.

HOTNNET is at the same level as the FTIR imaging, suggesting that HOTNNET is capable of removing static noise from the input images.

HOTNNET successfully demodulates the grayscale and the profile edges of recorded FIF images. Some minor spurious noise is visible in Fig. 2.6.a & b, arising from the very rapid droplet spreading and the fastest dynamic contact line movement in these experiments. The recognition of fringe patterns is not as precise in Fig. 2.6.c, but the trapped air pockets (light spots in the dark area) are accurately identified. The lower quality of unwrapped fringes in this case arises from the lack of similar patterns in the network training data.

The overset technique employed in HOTNNET ensures that the reconstructed images do not show any non-uniformity in the inter-boundary regions of the tiles, thus eliminating the so-called ‘edge effect.’ as shown in Fig. 2.7. The high order stencils of HOTNNET ensures that even at the edges the error is in the orders of 10^{-4} , but is larger very close to the liquid-solid contact due to sharp change of intensity.

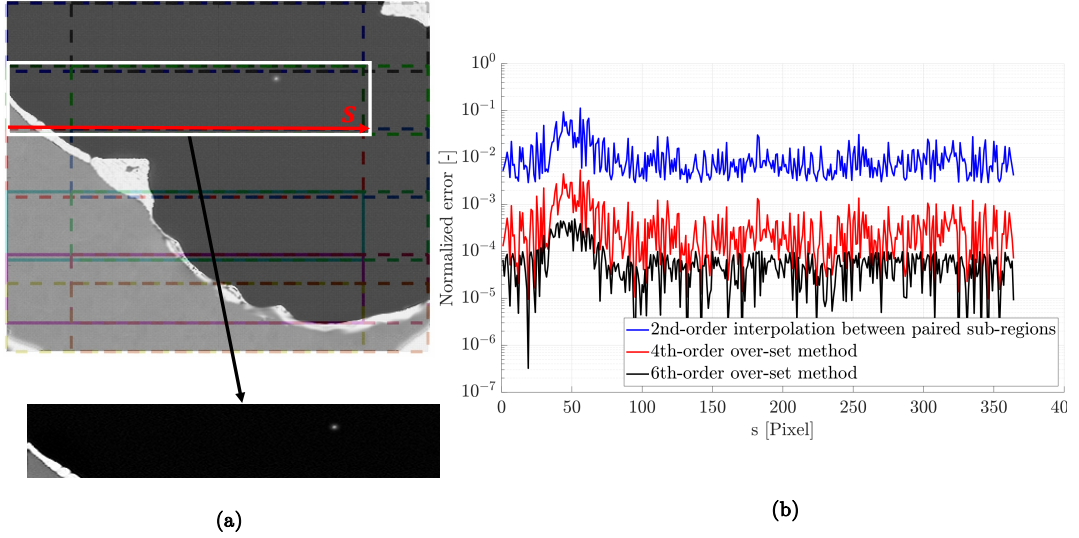


Figure 2.7: (a) The output of the HOTNNET with its subset (solid white rectangle) at the common domain as specified in Fig. 1. The image intensity at overlapping pixels of the tiles (coloured rectangles) are the result of Lagrangian interpolation in the overset scheme. The span (s) is the edge of one of the tiles selected as an example. (b) The normalized error along the horizontal s span passing through the overlapping grids. The error is in the orders of 10^{-4} , but is larger very close to the liquid-solid contact due to sharp change of intensity.

2.5 Discussion

In this work, we introduce HOTNNET - a computational framework that upscales and demodulates interferometric images, thus enhancing spatial resolution in all three dimensions. At the core of HOTNNET is a deep convolutional neural network that eliminates static artifacts from the images while simultaneously enhancing resolution. HOTNNET uses a high order overset technique to produce full super-resolved images from the interferometric images of a given size and is not constrained by the dimensions of the initial network training sets. In order to demonstrate the HOTNNET framework presented in this paper, we used a total 21 888 number of frames generated from experiments on droplet impact interfaces. The underlying physical results are explained elsewhere [67, 69] - when the drop approaches the surface, even at low speeds the initial dynamics of wetting are strongly altered by the confined air layer, which is displaced by the wetting fluid and deforms the liquid-air interface ahead of the contact line. The deformation results in a capillary disturbance that precedes the wetting front and leads to peculiar low wetting velocities beneath the impacting drop. These dynamics, ahead of the contact line, are inertial. Thus, the wetting front is surfing on a capillary wave and dragging a viscous tail in its wake.

Close to the edge of the contact line there is a distinguished halo region with sharp gradient in air layer thickness (Fig. 2.4.b-c). In this vicinity, the FIF images suffer from degradation of fringe patterns due to lack of lateral resolution and sharp slopes at the liquid-air and liquid-solid interfaces. This introduces inaccuracies in capturing the actual peak/trough locations (iso-intensity contours) and their intensity magnitude. Consequently, fringe pattern demodulation becomes impossible or extremely inaccurate. In HOTNNET results, the outline of the halo section is captured and there is little ambiguity in the extent of the actual peak of halo region as the relation between the air layer thickness and the normalized light intensity is monotonic. However, the mapping function from FTIR to air layer thickness given in [111] may need correction [52] for high slopes and curvatures.

In our droplet impact experiments, we are specifically interested in air layer thicknesses of nanometer scales where the van der Waals and other short-range interfacial forces can drive contact formation; these are the subject of recent numerical investigations [23]. We have targeted an accuracy close to few nanometers of precision. Close to darkest point of the camera ($O(10)$) the slope of the transfer function gets over 10^3 nanometer per unit change of normalized intensity (\bar{I}). Hence, in our overall HOTNNET imaging profilometry, we kept normalized root mean-squared error (NRMSE) per pixel below 10^{-5} . However, our initial implementation of FTIR profilometry of droplet impact experiments [69] employed a simplified total energy inversion algorithm,

$$h = -\delta \log(1 - \bar{I}), \quad (2.1)$$

that assumed all light incident upon the droplet's surface above the air transmitted into the drop, without taking into account the important role played by polarization of the light, resulting in error bars in Fig. 2.8 when doing the profilometry of the halo section. We will discuss the corrections required in the next Chapter. Fig. 2.8 shows the kinematics of wetting front for the droplet with a viscosity of 76 centi-Stokes falling from a height of 18 mm.

Further, here we investigate the image dimensions in convergence of training the network in HOTNNET. In an ideal scenario, a super-resolution microscopic imaging method should be capable of recording data with high-precision, covering a large spatial domain. In our experiment, the FIF imaging covers a large enough surface; using the HOTNNET technique, we have been able to improve the accuracy and quality of our FIF images to the same level as our locally recorded FTIR images as shown Fig. 2.9. We are further confident about the overset technique to remove the edge discontinuity (Fig. 2.7). For the physics of contact lines forming beneath impacting droplets, our imaging precision in x_3 direction is satisfactory. However, further improvements of the accuracy in the x_1 and x_2 directions, from the current 3.9 and 5.5 microns per pixel, respectively, are desirable. This augmented resolution can be achieved by replacing the current 5X microscope objective in the FTIR setup to a greater magnification. This will decrease the actual

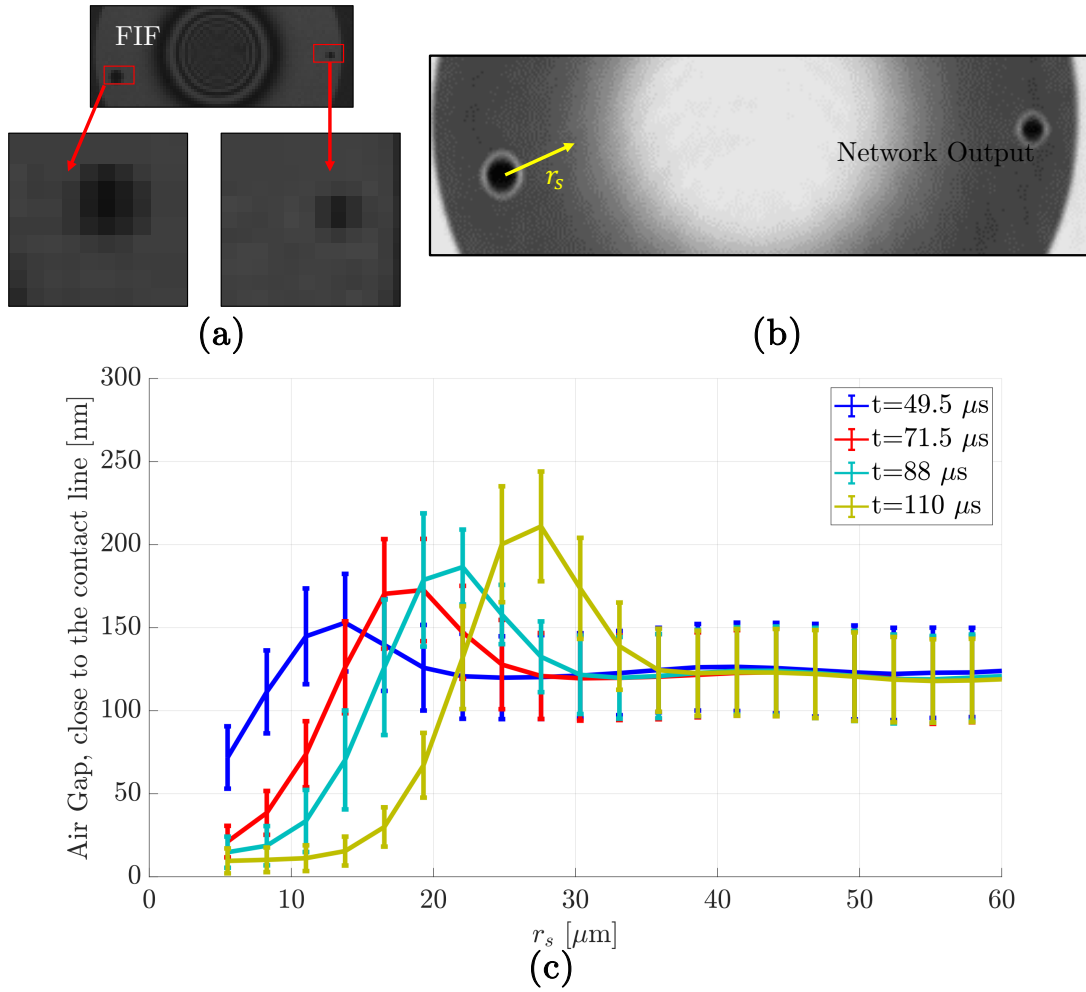


Figure 2.8: Kinematics of the wetting front: Close to the edge of the contact line there is a halo region with sharp gradient in air layer thickness causing smearing of FIF fringes as depicted in (a). The halo region leading the propagating front excites a capillary wave ahead of it. Thanks to the higher pixel per length ratio of FTIR microscopy, HOTNNET is better resolving (b) the outline of the halo section. The profilometry across the radial span r_s is given in (c). It shows wetting front propagating outward from the point of contact initiation.

dimensions of the subset used for the network training, *i.e.*, the blue rectangle in Fig. 2.1 or the white rectangular region in Fig. 5. One must be aware that the smaller subset recorded with the greater magnification might not have sufficient information to train the network to demodulate the FIF fringe patterns. In the other words, the training subset must correspond to sufficient interferometry fringe variation for trainability of the network. This would likely require at least one full modulation from minimum to maximum intensity in the fringe pattern. If this criterion is satisfied, the network is trainable, the rest of the HOTNNET procedure is straightforward.

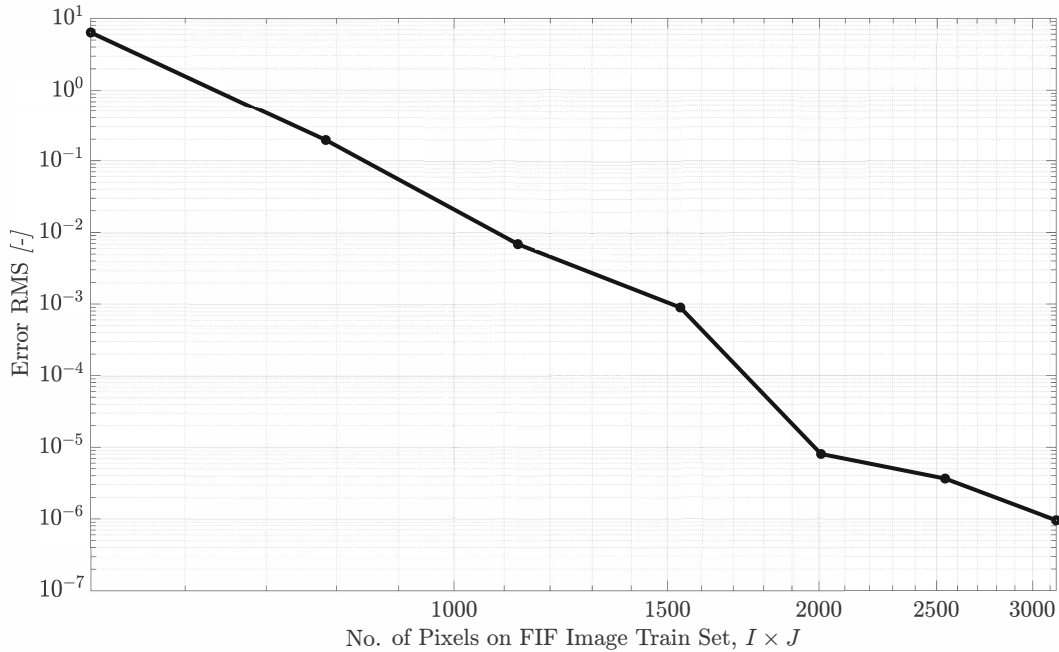


Figure 2.9: RMS of network output image error averaged on the test data sets versus number of pixels in the FIF image subset which is used for network training. Independent neural networks with similar architecture have been trained for different cropped image dimensions ($I \times J$) of 108×25 , 97×24 , 86×20 , 76×18 , 65×15 , 54×13 , and 43×10 . For untransformed subdomain dimensions of $86 \times 20 \approx 1700$ pixels, the error is in an acceptable range for very high resolution air gap measurement and contact line profile studies. This corresponds to $1.15 \text{ mm} \times 0.28 \text{ mm}$ tile size.

To quantitatively evaluate the minimum size of the training data, we have shrunk the dimensions of DCNN input images to 108×25 , 97×24 , 86×20 , 76×18 , 65×15 , 54×13 , and 43×10 towards the center and checked the performance of the network on 45484 test data pairs which were unseen data sets during the network training in terms of the root mean square of error on all pixels. The architecture and the other parameters of the network, including the maximum number of epochs, were maintained to ensure direct comparability of the network fidelity. The results show that using larger dimensions reduces the error, reproducing the FTIR images much more satisfactorily. The network is not trainable for 43×10 pixels, *i.e.*, $0.57 \text{ mm} \times 0.14 \text{ mm}$ subdomain size. For 54×13 pixels input, *i.e.*, $0.71 \text{ mm} \times 0.18 \text{ mm}$ subdomain, which is approximately the subdomain size which can be covered by a 20X objective, the network is trainable but the error is found to be high. We use a maximum root mean square of 10^{-4} as a threshold for trainability, which was achieved with a subdomain dimensions of $86 \times 20 \approx 1700$ pixels, or $1.15 \text{ mm} \times 0.28 \text{ mm}$ tile size. This width of the tile is comparable to the diameter of the droplet, *i.e.*, 1.6 mm .

While the HOTNNET framework can be readily adapted to other imaging datasets,

including those obtained with other interferometric imaging modalities for instance, the weight coefficient factors embedded in our trained neural network correspond to our specific optical setup. Consequently, changing the imaging system will require the network to be retrained. Retraining the network with a novel imaging system requires the collection of sufficient data for training, where the exact volume of training data depends on the quality of the images, but as few as several hundreds of images could suffice. The open-source code for HOTNNET including that for training the network is available on github [64].

Most neural network based super-resolution techniques use an artificially generated database of down-sampled, high-resolution images. Real world imaging artifacts such as sensor noise and static defects are absent from the images in these databases and thus these networks cannot be used for quantitative imaging modalities in science and engineering. HOTNNET faithfully treats the real-world recorded images because the complete data pairs for its network training are the outcome of laboratory experiments including imaging artifacts.

HOTNNET generates the final super-resolved mosaic by first mapping local tiles that are each super-resolved with the deep convolutional neural network. Because the regions of the mosaic correspond to different stages of the dynamics, the local mapping is non-invertible; thus on some level the network is classifying the contents of each tile based on limited information. Thus, like all other supervised learning strategies, the neural network in HOTNNET may lose fidelity when it is subject to substantially different interferometric image inputs. Nevertheless, for sufficiently similar interferometric images, HOTNNET is capable of producing super-resolved data that might be used quantitatively, and represents a step toward physically relevant data generated by neural network. Indeed, given the universality of physical behaviors, it is not outside the realm of possibility to use data obtained with HOTNNET to evaluate physical principles; this would require further work and verification to ensure that results obtained using the HOTNNET output are not artifacts of the processing, but instead are physical phenomena.

2.6 Conclusion

HOTNNET could be directly applied in fields of precision metrology provided that the neural network is appropriately trained. Using HOTNNET, we address constraints on our measurement due to the performance characteristics of our imaging hardware; however one can envision a means by which HOTNNET could address other constraints. For example, if an imaging system places an elliptical aperture in the imaging plane, the imaging domain would result in a non-rectangular tile shape. The overset technique in HOTNNET can be readily adapted to curvilinear geometries. Additionally, with appropriate calibration, HOTNNET could increase the accuracy of white light interferometry [71], which is currently limited by the bandwidth of the color filters on the CCD camera.

Chapter 2 Interface Imaging & Resolution Enhancement with HOTNNET

HOTNNET is designed to address constraints imposed by a given experimental setup using machine learning. This framework makes progress toward accurate and reliable physical measurements as the output of a trained neural network. Here, images recorded during droplet impact and contact formation were treated with HOTNNET, but the technique introduced here can be employed in the broader context of physics and engineering. HOTNNET thus offers a compelling and powerful tool that simultaneously achieves noise rejection, phase unwrapping and resolution enhancement of images when direct measurements are not possible or are cost prohibitive.

3 FTIR and FIF Microscopy

In Chapter 2, we have described the methods for imaging the droplet impact phenomena through the transparent substrates, namely: Fizeau Interferometry (FIF) and Frustrated Total Internal Reflection (FTIR) methods. Here, we describe how the recorded monochromatic images can be used to obtain the profilometry of the liquid-air-solid interfaces. Both FIF and FTIR profilometry modalities are founded on principals of classical electromagnetism, Maxwell's equations, and light diffraction/reflection theories.

The FIF profilometry is a well-established method and we discuss it briefly in Section 3.2. Use of FTIR microscopy as a quantitative tool for profilometry of interfacial mechanics is recent [111]. Here we describe the implementation details of the optical system that are crucial for an accurate microscopy and profilometry. This short chapter serves as a technical note for FTIR and FIF microscopy implementation.

3.1 FTIR Profilometry Modality

In our FTIR setup (Fig. 3.1.a), the top surface of a dove prism is illuminated with a 5 mW red laser light with 635 nm wavelength provided by Arima (www.arimalasers.com). The laser is mounted in the temperature controlled mount, model TCLDM9 provided by Thorlabs (www.thorlabs.com). The collimated light is aligned to be incident at an angle greater than the critical angle for total internal reflection at the substrate-air interface, but smaller than the critical angle at the substrate-liquid interface. The reflected light is recorded by high-speed Photron Fastcam Nova S12 camera sensor (<https://photron.com>) using a long-working distance (Mitutoyo 5X) microscope objective and a Thorlabs tube lens model TTL200.

The reflected light intensity is directly related to the air layer thickness by a deterministic transfer function [111], as long as the light at the substrate-air is linearly polarized -

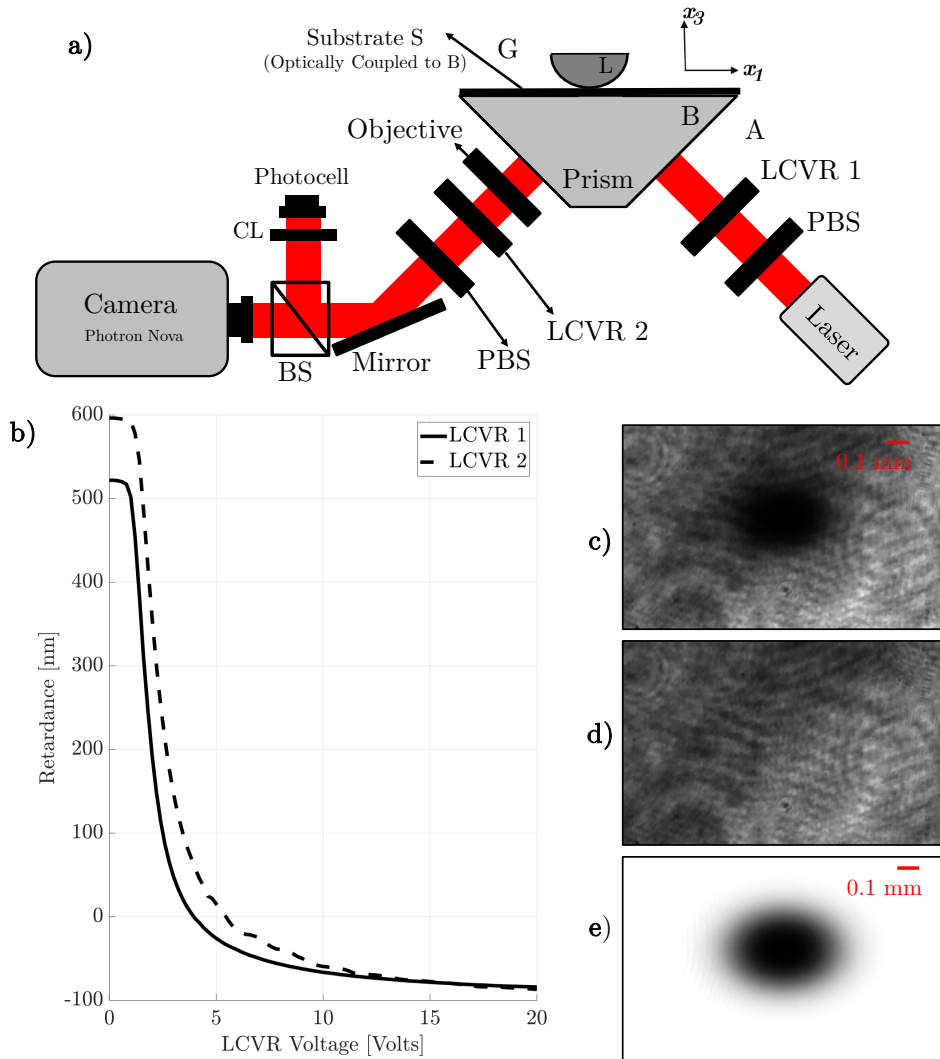


Figure 3.1: a) Schematic of our FTIR setup for a given substrate S: A p-polarized red laser source illuminates the Dove prism top surface with 45 deg incidence angle. The prism top surface is optically coupled with the substrate S. The two (LCVRs) shown perform the corrections for the change in polarization the of a given birefringent substrate like mica sheets. The light intensity recorded on the camera sensor is proportionate to the air gap beneath object/droplet (L) and on top of the substrate surface. Medium A, B, G are air, BK-7 glass, and air respectively. Medium L can be liquid or solid. Medium S can be birifringent. The laser diode wave length is 635 nm. LCVRs 1 and 2, provided by Meadowlark (www.meadowlark.com), are controlled continuously via a National Instrument (www.ni.com) by a MATLAB code. . b) The input voltage to LCVRs from the NI card is calibrated for the red wavelength using Thorlabs PAX1000 (www.thorlabs.com) polarimeter. For isotropic substrates like BK7 glass the corresponding voltages that provide zero retardance is applied. For birifringent substrates, the LCVRs remove the spill the light on the s-polarization plane at S-G interface. The polarizing beam-splitters (PBS) are used before each mirror to ensure no unintended change in the polarization of light occurs as quantified by the photo cell. The raw image, reference image, and normalized images recorded by using a spherical glass lens as L on a substrate mica (S) are shown in (c,e), respectively.

we achieve this by using two polarizing beam splitters and two liquid-crystal variable retarders (LCVRs) provided by Meadowlark (www.meadowlark.com). We used Thorlabs protected Aluminum mirrors for the laser light path alignment. Before any mirror in the optical path, we included a polarizing beam splitter to avoid unwanted light polarization change by the reflection.

We introduce n_G , n_S , ϕ_1 , and \mathcal{P}_1 as refractive index of air (gas), solid (substrate), the light angle of incident, and the light polarization at the air-substrate interface, respectively. For a given weakly birefringent substrate with an arbitrary optical axis (Θ_S), \mathcal{P}_1 is a function of

$$\mathcal{P}_1 = F(n_S, \Theta_S, \Phi_1, \Phi_2), \quad (3.1)$$

where Φ_1 and Φ_2 are the retardance angles of the LCVRs (Fig. 3.1.b). Thanks to the use of polarized light in our setup, \mathcal{P}_1 state can be easily described by s-polarized (\mathcal{E}_\perp) and p-polarized (\mathcal{E}_\parallel) components of the light electric field, \mathcal{E} , using extended Jones matrix algebra [50]. However, the values of n_S and Θ_S are not known a priori and measuring them using refractometer and polarimeter for numerous substrates is not feasible in our droplet impact studies. To overcome this issue, we follow the protocol below to perform an in-place system identification.

For each substrate, we sweep a range of voltages on the LCVRs which in turn characterizes the state of light polarization using the photo cell shown in (Fig. 3.1.a). We alter Φ_1 and Φ_2 in the range of 0.2–0.6 times the light wave length (λ) and find the n_S and Θ_S values that match the output light collected by the photo cell. In this range, the function F has the highest sensitivity to the values of n_S and Θ_S . Finally, we preset the LCVR 1 voltage to have pure p-polarized light at the interface, removing all the unwanted spill ($\frac{\mathcal{E}_\perp}{\mathcal{E}_\parallel} \rightarrow 0$) due to the birefringence of the substrate. We use the retardance of LCVR 2 to maximize the collected light by the photo cell to enhance the dynamic range captured on the camera sensor.

Profilometry with FTIR image processing is described by [111]. To summaries, firstly the FTIR image is stretched in the x_2 [19]. The image intensities are divided by the background image to obtain normalized intensities,

$$\bar{I} \equiv \bar{I}(x_1, x_2) = \frac{I(x_1, x_2)}{I_0(x_1, x_2)}. \quad (3.2)$$

Finally, the normalized intensities are mapped into absolute air layer thickness fields,

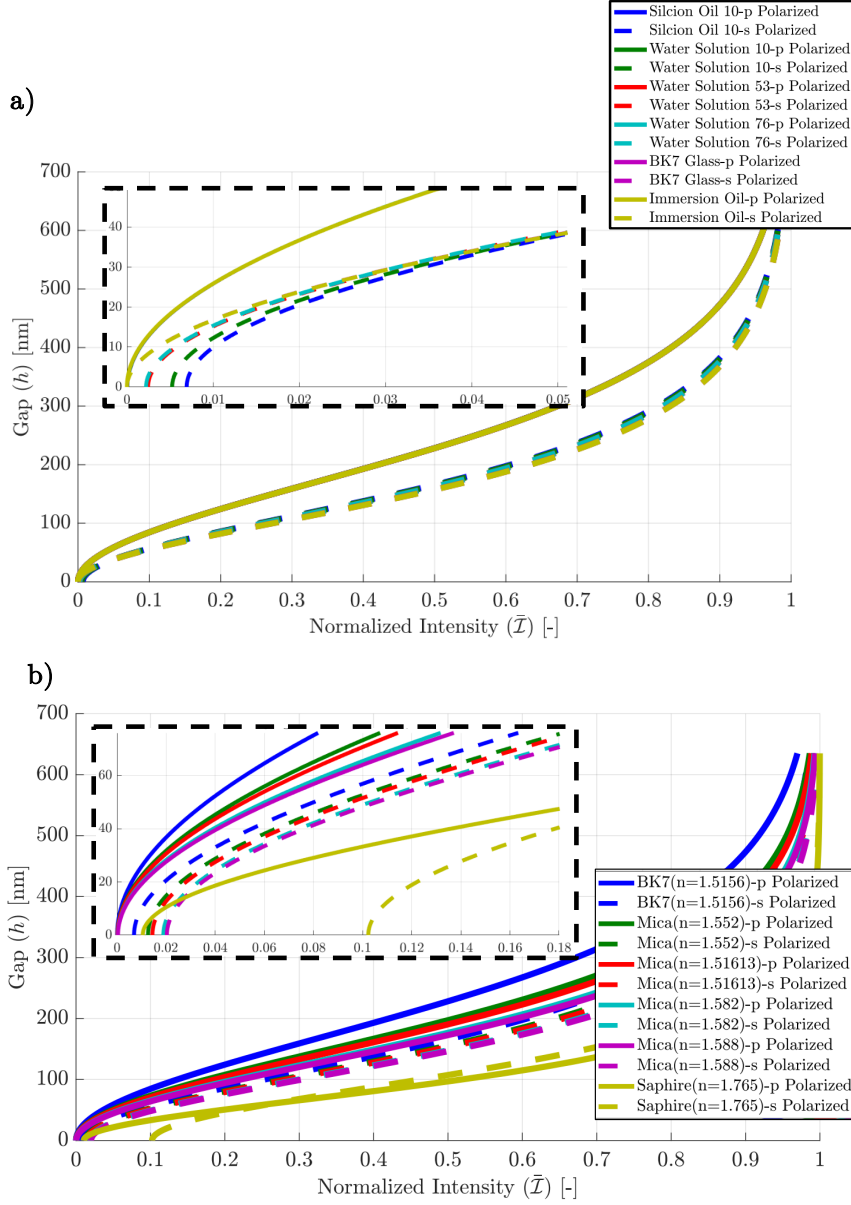


Figure 3.2: The mapping function of FTIR microscopy. a) The sensitivity analysis on refractive index of the liquid/object, n_L , shows little sensitivity of p-polarized light to n_L . b) The sensitivity analysis on refractive index of the substrate, n_S . We included the curve for different grades of mica sheets that we encountered. The mapping function of the p-polarized light is less sensitive to the value of object/liquid refractive index.

$h(x_1, x_2)$, using the following equation,

$$h = \frac{\lambda \delta}{4\pi \sqrt{n_G^2 - n_S^2 \sin^2 \phi_1}}, \quad (3.3)$$

where δ is resulted based on Fresnel equations from the following relation [140]

$$\bar{I} = \left(\frac{r_{SG} + r_{GL} e^{j\delta}}{1 + r_{SG} r_{GL} e^{j\delta}} \right)^2 \quad (3.4)$$

with constant values

$$r_{SG, \perp} = \frac{n_G \cos \phi_1 - n_S \cos \phi_2}{n_G \cos \phi_1 + n_S \cos \phi_2}; \quad r_{SG, \parallel} = \frac{n_S \cos \phi_1 - n_G \cos \phi_2}{n_S \cos \phi_1 + n_G \cos \phi_2} \quad (3.5)$$

$$r_{LG, \perp} = \frac{n_G \cos \phi_3 - n_L \cos \phi_2}{n_G \cos \phi_3 + n_L \cos \phi_2}; \quad r_{LG, \parallel} = \frac{n_L \cos \phi_3 - n_G \cos \phi_2}{n_L \cos \phi_3 + n_G \cos \phi_2} \quad (3.6)$$

$$\phi_2 = \sin^{-1}(n_S/n_G \cdot \sin \phi_1); \quad \phi_3 = \sin^{-1}(n_G/n_L \cdot \sin \phi_2) \quad (3.7)$$

In these equations, n_L is the refractive index of the liquid (or the solid object in the penetration depth of FTIR microscopy), j is the imaginary unit, and the subscripts \perp / denote s- and p-polarized components of the light, respectively.

In practice, we used pure p- polarized light in the FTIR imaging to simplify the equations above and h is readily deduced using a lookup table [111], instead of inverting relation 3.4. The family of $h(\bar{I})$ are presented in Fig. 3.2 for the mediums (liquid-solids) that are studied in this work.

3.2 Interferometric Imaging and Profilometry

The second profilometry method that we used is based on the interferometric images that are presented in Chapter 2 referred to as FIF imaging data. The FIF optical path is perpendicular to the substrate surface as shown in Fig. 3.3.a. In our monochrome FIF imaging [98], we used unpolarized light from a high power blue LED provided by ILS Solutions (<https://i-led.co.uk/>) with a wavelength of 455 nm. We collimated the light and direct it onto the optical path using a 50-50 beam-splitter and focus it on the substrate surface by a long-working distance (Mitutoyo 5X) microscope objective. Due to short coherent length of the LED light we do not include the quarter wave plates required by FIF setup with laser lights [98].

In FIF, the droplet/object (L) enters to within the coherence length of the light, forming an optical cavity between the object (L) surface and the substrate (S) surface. The clearance between S and L are filled by the medium air (G). Some of the light reflects from the S-G interface, *i.e.*, interface (1) in Fig. 3.3.a

$$I_{(1)} \propto r_1^2 I_\infty, \quad (3.8)$$

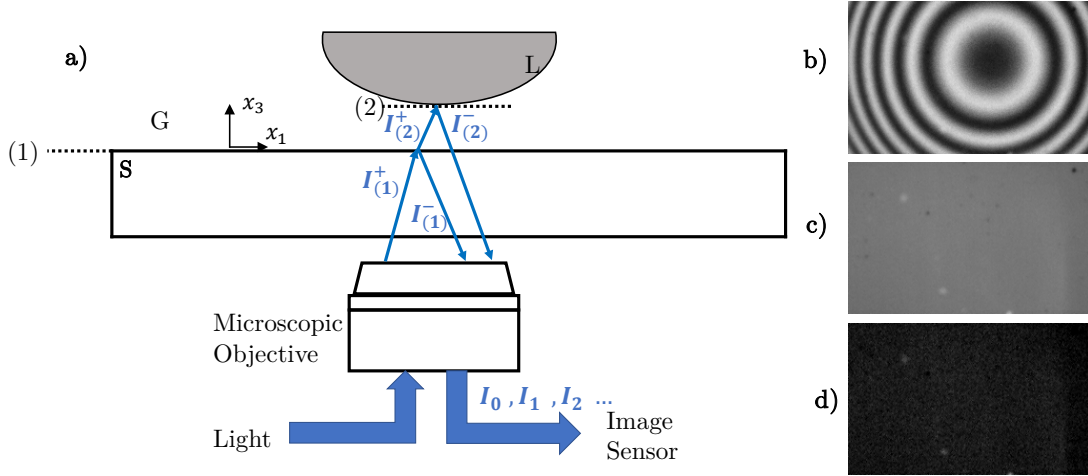


Figure 3.3: a) Schematic of FIF microscopy. b) A spherical lens (L) of known shape in contact with the substrate S creates Newton ring. c) The dark reference image is required for normalizing the image. For liquid droplet experiments it is obtained from the stage that the liquid covers the substrate. For the calibration with the BK-7 glass lens, we obtained it by depositing immersion oil on the substrate which has a similar refractive index as BK-7 glass. d) The bright image is calculated at the post-processing stage from the dark image and the reference image when the object L is absent.

and a smaller portion of the transmitted light reflects from the G-L interface,

$$I_{(2)} \propto (1 - \tau_1^2)^2 (\tau_2)^2 I_\infty, \quad (3.9)$$

that is interface (2) in Fig. 3.3.a where,

$$I := I(x_1, x_2, \lambda) \quad (3.10)$$

is the light we capture on the camera sensor. It is a function of the light source spectrum specified described by (λ_{peak})

$$I \propto \int I(\lambda) I_\infty(\lambda, \lambda_{peak}) d\lambda. \quad (3.11)$$

Depending on the gap thickness between the S and the L, these two reflected beams will interfere [31, 39].

$$(I - I_0) \propto I_{(1)} + I_{(2)} + 2\sqrt{I_{(1)}I_{(2)}} \cos(2k_G h + \pi) \quad (3.12)$$

where

$$h := h(x_1, x_2), \quad (3.13)$$

$$k_G = n_G \frac{2\pi}{\lambda}, \quad (3.14)$$

and I_0 is a constant background light proportionate to the sum all those lights that are reflected from other interfaces in the light path (if any) on the sensor. The interference between the two reflected beams from the varying gap [31, 39] results in a pattern of fringes. For a spherical object (L) in the field of view, the pattern of fringes resembles Newton rings as shown in Fig. 3.3.b. We record the fringe images by a Photron S12 Fastcam through a Thorlabs tube lens model ITL200.

The finite illumination numerical aperture (INA) of the microscopic objective and the resulting light cone introduces additional complication in the formulation [30, 98, 105]. Defining

$$\phi := \arcsin\left(\frac{INA}{n_G}\right), \quad (3.15)$$

$$I \approx I_{(0)} + \Pi [I_{(1)} + I_{(2)} + 2\sqrt{I_{(1)}I_{(2)}}\Gamma(h) \cos(2k'_G h + \pi)] \quad (3.16)$$

where

$$k'_G := k_G(1 - \sin^2(\phi)) \quad (3.17)$$

$$h' := 2k_G h \sin^2(\phi) \quad (3.18)$$

$$\Pi := 4\pi \sin^2(\phi) \quad (3.19)$$

$$\Gamma(h) := \frac{\sin(h')}{h'} \quad (3.20)$$

In practice, we normalized the light with respect to a dark (I_{\min}) and bright field (I_{\max}) [105] shown in Fig. 3.3.c-d and write the normalized intensity \bar{I} as a damped cosine function (g) integrated over λ :

$$\bar{I} = g(h, \phi, I_{\infty}(\lambda, \lambda_{peak}), \mathbf{r}_1, \mathbf{r}_2) =: G(h) \quad (3.21)$$

Instead of relying on the spectrum of the LED light source to do the integration of Eq. (3.11), we followed an engineering approach and constructed the \bar{I} mapping function,

$G(h)$, directly from a controlled experiment as described in Section 3.3.

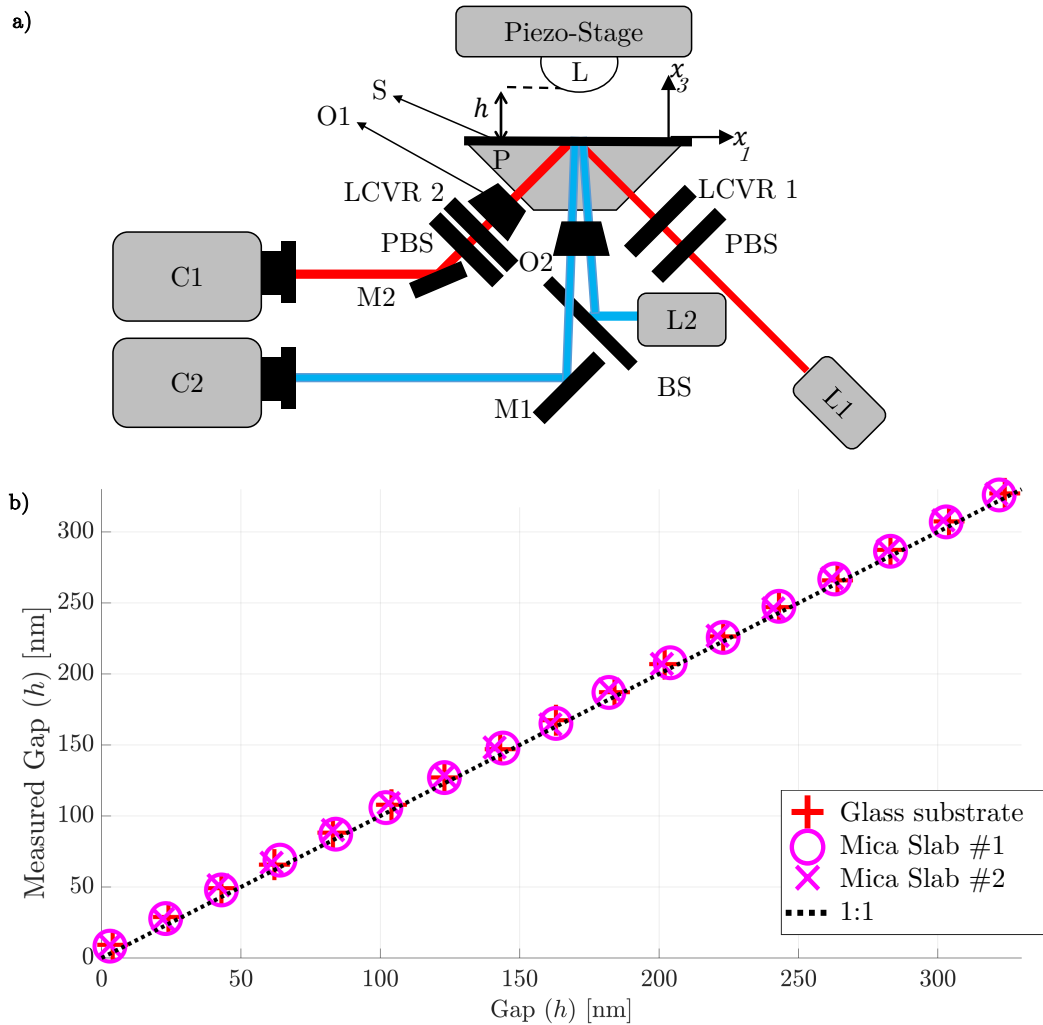


Figure 3.4: a) Schematic of the setup used for the calibration of the profilometry methods introduced in Section 3.1-3.2. All the element in the FTIR (red light path) profilometry modality are introduced in Fig. 3.1. FIF profilometry modality (blue light path) uses a high power blue LED light source (L2) that is collimated and goes through the beam splitter (BS) and is captured on sensor C2 through another dry 5X Mitutoyo microscope objective (O2). Both Cameras C1 and C2 are monochromatic Photron Nova type with tube lenses, recording at 125 FPS. Piezo-stage controller is of NPC3SG type with carries and advances the rigid object (L) towards the substrate with nano-metric precision until the lowest point on the object touches the substrate. b) The gap measurement is presented for FIF and FTIR which are in complete agreement with each other. The microscopy setup is accurate in the range of 0 – 350 nm with an error bar of 7.5 nm in the x_3 - direction.

3.3 Calibration

We will use the FTIR and FIF profilometry methods for the study of liquid-air-solid interfaces in the droplet impact events in this thesis. Specially, we cross check our measurements of the critical air film thicknesses during the droplet impact by the two independent but simultaneous microscopy methods to achieve a good degree of confidence as there have been striking discrepancies in the values reported for this parameter in the literature [45]. It is important to calibrate the microscopy techniques described earlier in this chapter. We optically couple the solid substrates to the optically smooth dove prism (BK-7 glass) in the setup by immersion Oil. We assembled both FTIR and FIF optical elements on the same setup.

The optical configurations for both methods are depicted in Fig. 3.4.a. We used the setup to track the known trajectory of a surface in the field of view. We incorporated a piezo stage with nanometer precision, model NPC3SG provided by Newport (www.newport.com) in our setup. As shown in Fig. 3.4.a top, we attached a spherical glass lens to the stage face and swept in the negative x_3 direction starting from $h \approx 350$ nm with steps of 20 nm until the lowest points of the lens touch the substrate. At each step of piezo stage, the synchronized cameras record 250 FIF and 250 FTIR images at 125 FPS. We reduced the vibrational noise of the setup by using rigid mounts and sorbothane sheets to small amplitudes ≈ 20 nm. We took the median of the 250 recorded images at each stage to deal with the issue. The step at which the solid-solid contact occurs is evident when the lens profile is recorded by the cameras (Fig. 3.4.b). Further at this stage, the mechanical vibrations reduces to zero. There are hundreds of control point on the lens bottom profile that are used for redundancy check of calibration.

We normalized the FTIR images, stretch them in the x_2 directions, and use normalized intensity-to-gap mapping functions per the procedure explained in the previous section. We used different mica sheets and glass as substrates and found the maximum absolute error in the profilometry to be less than 7 nm in capturing the range of gaps $h = 0 - 350$ nm (Fig. 3.4.b). We normalized the FIF images with respect to the dark and bright fields as shown in Fig. 3.3. We found the mapping function to be universal (Fig. 3.5) for our optical setup and fits any point trajectory on the calibration lens even by changing the substrate with an error bar of $+8/-4$ nm.

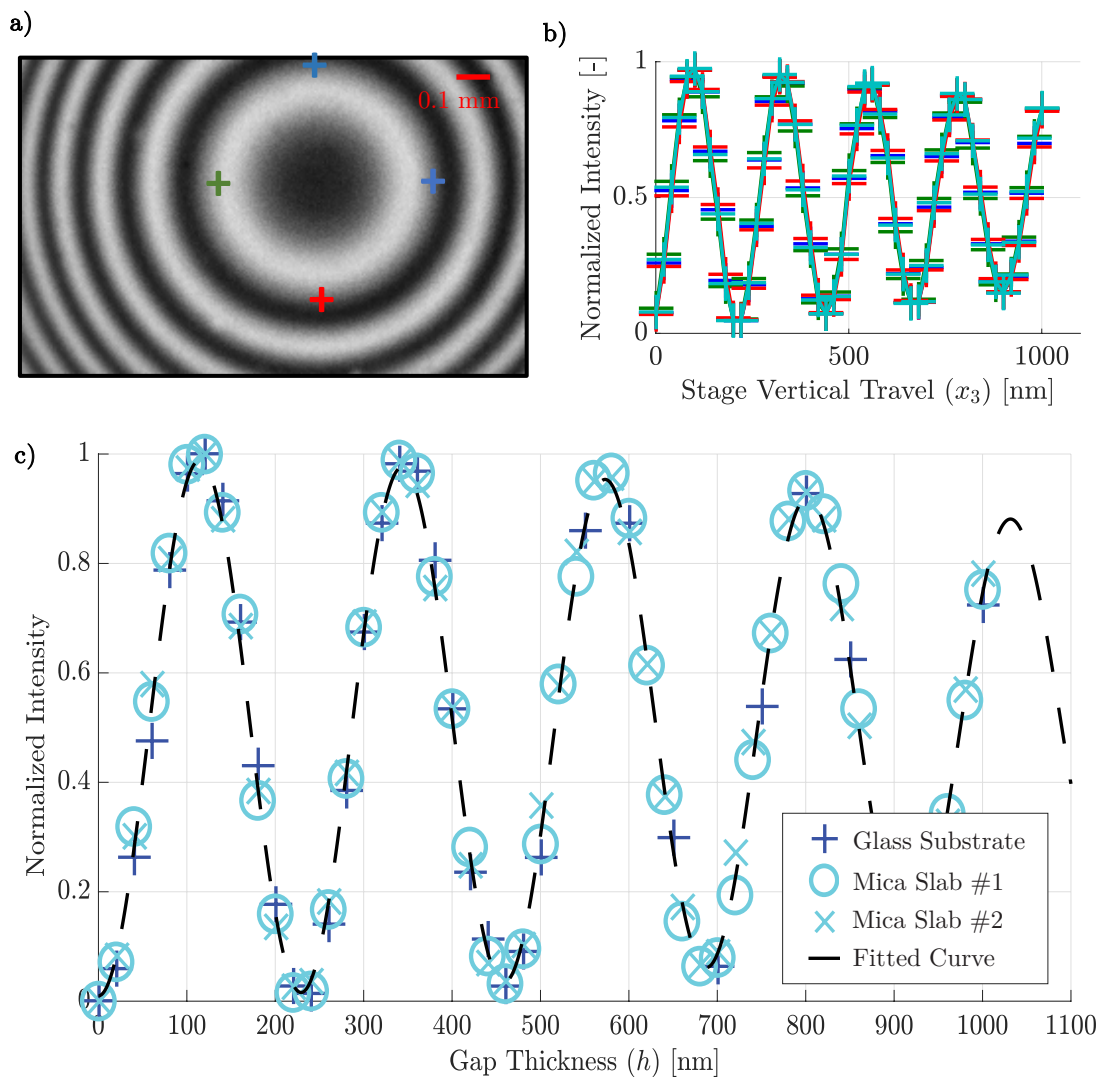


Figure 3.5: a-b) 4 points that are in the equal distance from the center of the spherical lens (L) are tracked by the FIF microscopy using the setup in Fig. 3.4.a and they follow the same curve. c) The mapping function $\bar{I} = G(h)$ is established from the calibration setup. The mapping function doesn't change with different substrates, if image normalization is performed as per Fig. 3.3.

4 Droplet Impact: Air Film Rupture

The initial formation of contact between a liquid and a solid surface is typically mediated by a third medium - most often in our daily experience, air. Indeed, when a droplet of water impacts a solid, it makes contact imperceptibly quickly; - a transition so rapid that it occurs much faster than we can observe with the unaided eye. However, from a continuum perspective, we know the gas must be punctured, or otherwise disrupted, for liquid-solid contact to form.

Although the air film formation and rupture phenomenon are well known, the underlying mechanism of its instability has not yet been conclusively determined. It is only recent that laboratory tools can capture the microscopic scales involved in the process [30, 31, 69, 70, 79, 83, 125]. The formation and dynamics of the air film have been studied using X-ray imaging [76], interferometry [39], white color interferometry [125], two-color interferometry [32], tri-wavelength interferometry [45] and total internal reflection method [70]. For a basic case of a droplet falling at a low velocity, the mediating air gets pressed on which further decreases the droplet inertia. In this regime, the lubrication dynamics of air layer prevents mathematically the rupture of the film in a finite time duration [41]. Hence for a contact to initiate, the finale of the process needs to involve additional physical mechanisms that trigger the instability and rupture of the air film. Indeed, various mechanisms ranging from spinodal dewetting [70] to gas kinetic effects [23] or even surface roughness have been identified as possible causes for air film rupture [41]. In the absence of theoretical justification, the threshold of contact initiation is usually described by an air film cut-off thickness (h^*) below which the film ruptures, known as height of closest approach.

There have been striking discrepancies in the value of h^* that are reported by different

This majority of the material in this chapter is under preparation for submission as Kaviani, R. and Kolinski, J. M. (2023). The Characteristic Rupture Height of the Mediating Air Film beneath an Impacting Drop on Atomically Smooth Mica.

Authors' Contributions J.M.K. conceived the project. R.K. conducted the experiments under the guidance of J.M.K. R.K. and J.M.K. interpreted the results.

experimental studies [32, 45, 70, 85] ranging from 1 – 2 nm till few microns. The imprecision with which the final film thickness prior to rupture is known makes it impossible to distinguish between the various mechanisms that may dominate these dynamics, making numerical calculations significantly more difficult, and leaving open a fundamental and important question of what drives liquids into contact with solid surfaces.

In this thesis, we employ two separate optical measurement methods to determine h^* with a sufficient degree of certainty. We study the process of air layer formation and breakdown for impacting droplets of silicon oil and water-glycerol onto a smooth mica substrate at low and moderate impact speeds. We show that the air layer thickness can get smaller than the mean free path of air. At such length-scales, short-range inter-molecular forces become relevant. This is confirmed by recent numerical simulations of impacting water-glycerol liquid droplets carried out by Chubynsky et al. [23] where van der Waals interactions have been modeled. Our experiments with silicon oil droplets is in qualitative agreement with the findings of Chubynsky et al. [23] indicating that van der Waals pressure is the driving agent for the air film rupture. However, for droplets of water-glycerol solution impacting on mica, our data is inconclusive. We proposed a possible explanation that short-range forces of electrostatic nature may explain the behaviour but in absence of definitive evidence, we report the result of our measurements without prejudice for the scientific community to comment on. We further quantify a critical local air film height of $h_{\min} = 20 \pm 3$ nm right before the wetting initiation through a spontaneous contact. This is in agreement with numerical simulations of Chubynsky et al. [23].

4.1 Experimental Setup

The physical setup considered is a drop of liquid falling from the nozzle on a flat solid surface in the presence of the surrounding gas (air) at room temperature and atmospheric pressure. As the liquid drop falls towards the solid surface, it interacts with the air. The drop is initially spherical, with diameter D , falling towards a horizontal solid surface at uniform vertical U as shown in Fig. 4.1.a-b. We control the impact velocity by releasing the droplet from different fall heights (H) and measure U by a side camera. We studied the velocity ranging between 0.35 – 0.91 m/s (Fig. 4.1.c).

For the solid substrate, we used muscovite mica sheets. A mica slab is transparent and can be easily cleaved through its thickness, obtaining an atomically smooth surface over several millimeters. We conducted the experiments with two different liquids: water-glycerol solution droplets with $D = 1.91$ mm and silicon oil with $D = 1.83$ mm. We used silicon oil with a viscosity of 10 cSt and prepared the water-glycerol solution mixture to have the same kinematic viscosity. The density of the solution and oil are 1168.1 kg/m³ and 937.1 kg/m³, respectively. The surface tension for the solution (68.0 mPa.m) is

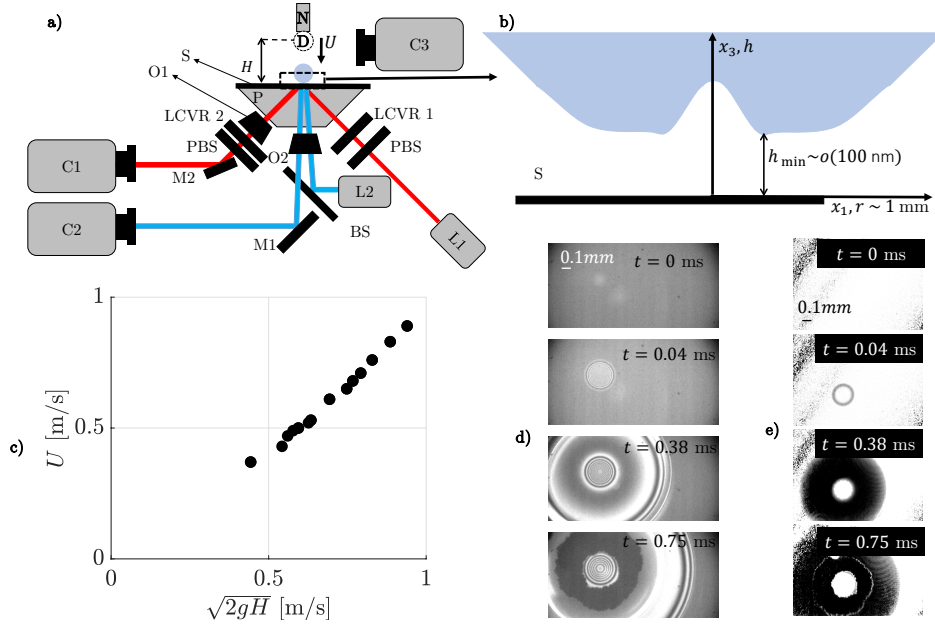


Figure 4.1: a) Schematic layout of simultaneous FTIR and FIF microscopy for the study of droplet impact. The setup is calibrated to have an accuracy of $\pm 7 \text{ nm}$ for air layer thickness measurements below 300 nm in the x_3 direction (see Section 3.3). The liquid drops with diameter ($D \approx 2 \text{ mm}$) fall from the height H from the nozzle (N) on a mica substrate (S) reaching maximum velocity of U . We cleave a mica slab through its thickness to obtain an atomically flat surface over several millimetres in $x_1 - x_2$ plane. We optically couple the mica sheets to the dove prism (P) made from BK-7 glass by immersion oil. In the FTIR microscopy optical path, coherent light emitted by the laser source (L1) illuminates S at incident angles greater than the critical angle for the solid-air interface. We use the polarizing beam splitters (PBS) and liquid-crystal variable retarders (LCVR) to ensure that the light arrives at the substrate-air interface linearly p-polarized. The light is totally internally reflected from the mica-air interface beneath the impacting droplet and is captured by camera C1. FIF data are acquired using a second optical path. Light emitted from a high power LED light source (L2) passes through the beam splitter (BS), reflects from the impact interface, and is captured on camera (C2). Two dry 5X Mitutoyo microscope objectives (O1 and O2) are used for magnification. The monochromatic fast cameras C1 and C2 are fitted with tube lenses (not shown), and are synchronized to record images at 80,000 FPS. Mirrors (M1 and M2) are used to align the light. We use a third camera (C3) recording at 8,000 FPS to measure U . b) The region underneath the droplet just before contact initiation is shown schematically with an exaggerated x_3 axis: the air forms a nanometer-scale lubrication layer, at the periphery of a dimple centered upon the impact axis. c) Impact velocities, U , ranging from $0.34 - 0.91 \text{ m/s}$, are controlled by changing H . d)-e) Example image series of the air film formation and rupture as captured with the FIF and FTIR imaging modalities are shown at three time steps. After post-processing, the light intensities can be converted to the air film thicknesses for each image; the temporal evolution is recovered by evaluating the time series of images. The dimple region centered upon the impact axis of the droplet is clearly visible; it extends a few microns from the impact surface, as can be seen from the fringe rings in the FIF images. This region resides outside the penetration depth of the FTIR imaging modality, and is identifiable from the bright circles centered upon the impact axis in the FTIR images.

greater than of the oil (20.2 mPa.m) as measured by pendant drop method. Both liquids wet the mica surface.

We implemented two concurrent dynamic profilometry techniques to image the liquid-air-solid interface and measure the thin film profile with a good degree of certainty, namely, frustrated total internal reflection microscopy method (FTIR) and Fizeau Interferometry (FIF). Simultaneous FIF and FTIR imaging is used in recent interfacial mechanics studies with success [19, 65, 94, 95]. We explained the details of our setup including the calibration in Section 3.3. These concurrent modalities provide complimentary information about the liquid-air-solid interface - FTIR can resolve air layer thicknesses up to ≈ 400 nm, whereas FIF can visualize the air film profile of up to several microns [98]. In FIF, the film profile is encoded in a two-dimensional fringe pattern, where the intensity of the fringes indicates the optical interference at a given spatial location within the image. The FIF fringe patterns should be demodulated to provide absolute film measurements that are up to few microns thick. We avoid this by simply considering the regions that the film thickness is less than half of the light wavelength, ≈ 200 nm.

Our microscopy setup has a resolution of $3.6 \mu\text{m}$ in the $x_1 - x_2$ plane. In the x_3 direction, the resolution of profilometry is as low as 7 nm but the calibrated field of view in this direction is limited to 350 nm. We observed that the threshold of unstable air gap thicknesses (h^* and h_{\min}) fall below this limit. In our droplet impact experiments, we record the images at 80,000 the frame per second (FPS). The sequence of images in Fig. 4.1.d-e shows the rapid nature of air film formation, its rupture, and surface wetting.

4.2 Squeezing and Piercing the Air layer

The bottom surface of a falling droplet squeezes and drains the air film. At the very early stage of a low speed impact, the liquid skates over the air [70] and increases the lateral extent of the air film. In this regime, the droplet entrains the air at the leading edge of the drop deforming the liquid-gas interface when approaching the solid. If the air film remains stable throughout, the droplet rebounds as shown in Fig. 4.2.a-b. This indicates a threshold height of closest approach (h^*) which decreases as the impact speed increases (Fig. 4.2.c-d). At such small length scales $O(300 \text{ nm})$, the film of air is entrained beneath the impacting drop and decelerates it - the liquid and gas inertia can be neglected. While the air slowly drains, the radial extent of the thin film grows until a minimum h^* after which the rebound starts [69]. The bouncing to wetting transition velocity for the oil droplets (0.6 m/s) is higher compared to that of the solution (0.53 m/s). The minimum h^* for the oil ($32 \pm 3 \text{ nm}$) is lower than the solution's ($60 \pm 3 \text{ nm}$).

While in our daily experience the initiation of contact between the droplet and the surfaces seems trivial, the contact process is a topological transition in these nanometric scales. The drop must first pierce the air to initiate the wetting. The initial formation of

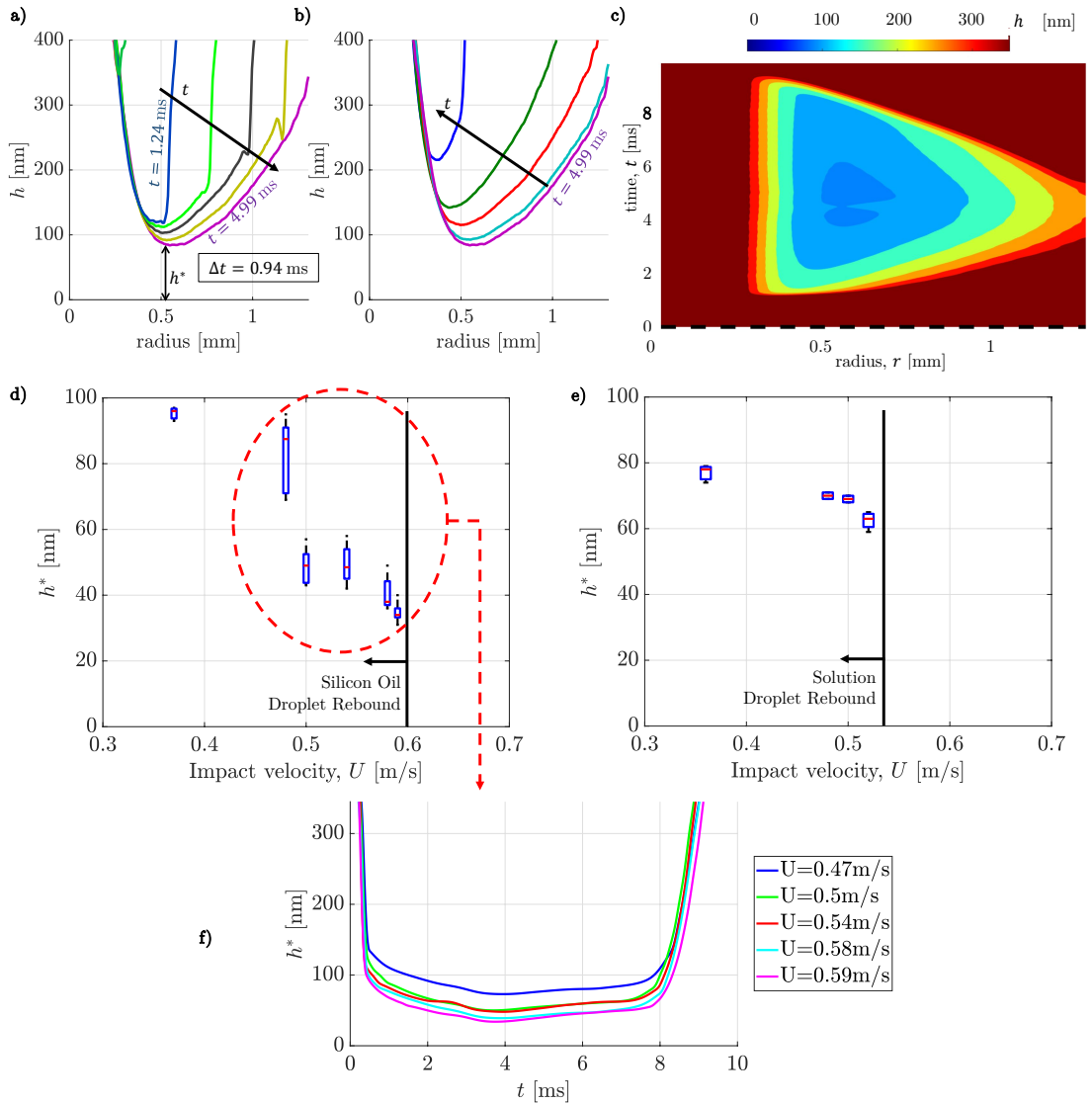


Figure 4.2: Less than a critical impact speed, the air film under the droplet is stable and functions as a cushion that causes the droplet to rebound off the mica substrate. As an example for $U = 0.52$ m/s, the 10 cS water-glycerol droplet pushes the air layer creating a time dependent profile h which is drawn based on the radius, r , from the center of the impact in (a-b) for few time steps. The data is truncated at the maximum gap thickness of 350 nm which is the limit that our microscopy setup is calibrated for. Time (t) is measured from the moment time droplet enters the FIF field of view $h(0, t = 0) = O(10^{-6})$ m. Same data is plotted in color map of (c) indicated by the color-bar for continuous t . For impact velocities more than a threshold, the air layer is always unstable and the wetting initiates. This indicates a limiting stable film height (h^*) which decreases gradually with higher velocities as shown in (d,e) for the silicon oil and the water-glycerol solutions, respectively. The bouncing critical velocity for the oil droplets (0.6 m/s) is higher compared to that of the solution (0.53 m/s). The $h^*(t)$ variation close to critical impact velocity is presented in (f) for the solution. The minimum captured h^* for the oil, at 32 nm, is lower than the solution, at 59 nm.

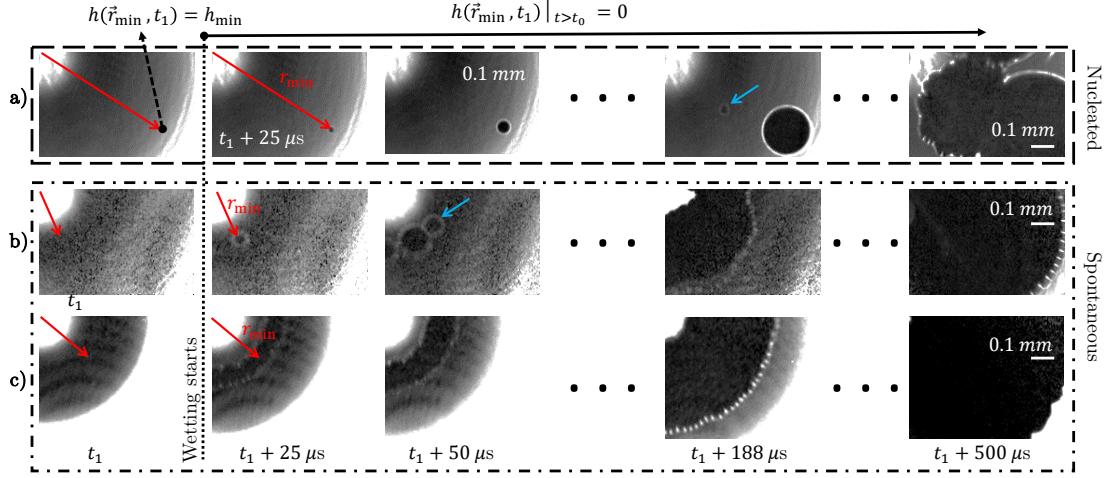


Figure 4.3: The normalized image series of contact formation from the FTIR microscopy for a) $U = 0.5$ m/s, b) $U = 0.58$ m/s, c) $U = 0.91$ m/s. The wetting starts by breaking through a thin layer of air between a mica surface and the liquid. h_{\min} is recorded locally at r_{\min} at the last frame recorded ($t = t_1$) just before the air film rupture is captured by the high speed camera. In (a), 2 nucleated contact form as separate entities and the contact lines moves radially outwards from the respective points of formation until they meet. The spontaneous contact initiation shown (b-c) are considerably more axisymmetric with respect to the center of the droplet ($r = 0$).

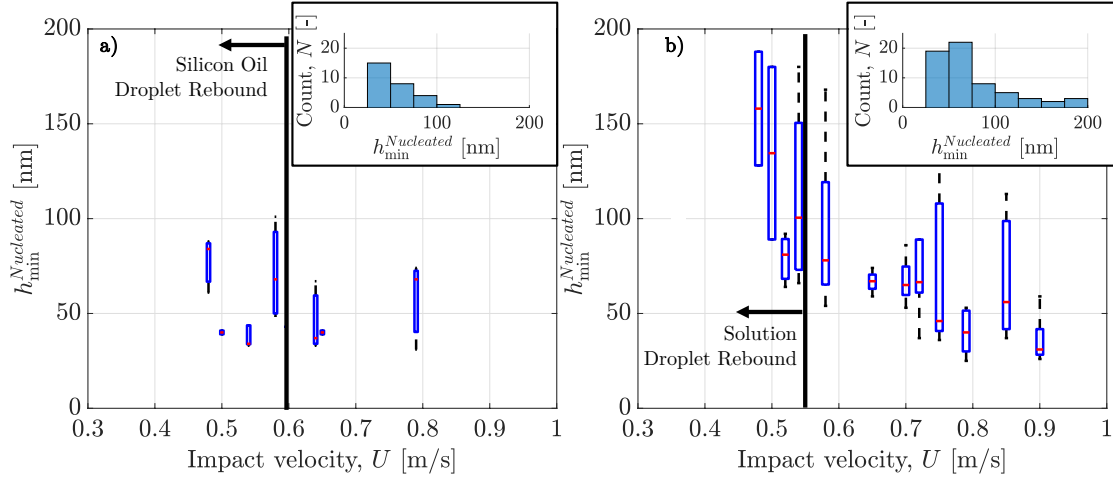


Figure 4.4: For nucleated contact formation between the liquid and the solid, the lowest film heights h_{\min} are shown for a) the silicon oil and b) the water-glycerol solution. The distribution of h_{\min} appears to be randomly distributed, albeit with much greater nucleation heights for the water-glycerol droplets for impacts below the threshold rebound velocity. The bottom and top edges of each box indicates the 25th and 75th percentiles, respectively. The central mark indicates the median. The whiskers extend to the most extreme measurements not considered outliers. The outliers, if any, are plotted individually using the '+' marker symbol.

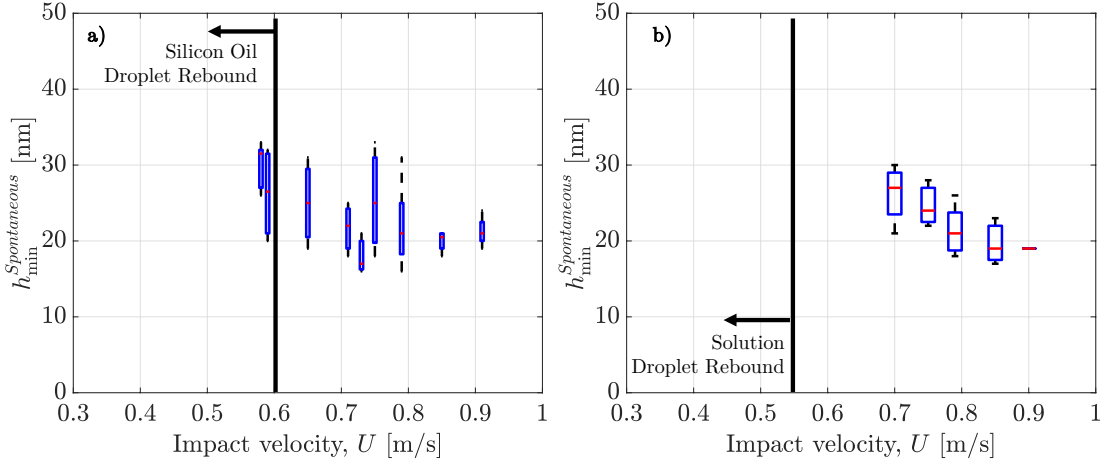


Figure 4.5: The lowest film height, h_{\min} 's, are plotted for spontaneous contacts in (a,b) for the oil and the solution, respectively. Spontaneous contact formations are much more frequent for the oil but h_{\min} lies in a range of 18 – 35 nm for both liquids. The resolution of the data is limited by the cameras speed and the lower bound of h_{\min} data is the relevant quantity, *i.e.*, $h_{\min} = 18 \pm 3$ nm for both the liquids. Minimum h_{\min} 's do not change with the impact speed. This is evident for the silicon oil. The data density for the solution is less dense for spontaneous impacts, still any changes observed (~ 7 nm) in $h_{\min}^{\text{Spontaneous}}$ are within the tolerance of the profilometry measurement. Despite several tries, we did not observe any spontaneous contact formation for moderate velocities of water-glycerol droplet impact, $U < 0.7$ m/s.

contact - via a topological transition from a coherent air film to a locally ruptured air film - is observed to occur in two distinct manifestations. First, and most commonly, the air film ruptures locally, at an isolated contact, independently of the relative location of the globally minimal air film thickness. Such events are clearly nucleated contacts at a local disturbance due to a surface imperfection and the proximity of the liquid to the solid over the extent of the thin air film. An example of such a nucleated contact is given in the time series shown in Fig. 4.3.a. The second mode of contact formation is typified by the near exact correspondence between the location of air film rupture and the globally minimum air film height. Due to the axisymmetry of the air film profile, such events are often clustered closely in time, and occur at a nearly identical radial distance from the impact axis. Two examples of this spontaneous mode of contact formation are shown in Fig. 4.3.b-c.

In both cases of nucleated and spontaneous contact, we record a local height h_{\min} at the point of contact in the last frame recorded ($t = t_1$) just before the air film ruptures and showed them in Fig. 4.4 and Fig. 4.5. The h_{\min} distribution for nucleated contacts is uniform with respect to the impact velocity. In the absence of nucleation, we did not capture spontaneous contact formation for local film thicknesses greater than 35 nm - contact initiates suddenly from a measurable height above the surface. However, the

resolution of the data is limited by the image acquisition rate and the lower bound of h_{\min} data is the relevant quantity. h_{\min} equals 18 ± 3 nm for both the liquids, although spontaneous contact occurs much more frequently for the oil. Further, h_{\min} lies in a range of 18 – 30 nm for both liquids. h_{\min} doesn't change considerably with the impact speed. The changes observed are within the tolerance of our microscopy accuracy (~ 7 nm).

4.3 Discussion

Water-glycerol solution droplets tend to nucleate contact from greater heights than silicon oil droplets; however, both form contact spontaneously from a narrow distribution of film thicknesses, ranging from a minimum of 18 to a maximum of approximately 30 nanometers, with a measurement error of approximately 10 nm. The statistics of contact are consistent with a spinodal dewetting mechanism whereby the air film is destabilized by interfacial attraction of the liquid to the solid surface, as demonstrated by the timescale and height observed for spontaneous and nucleated contact formation.

In the range of impact speeds considered in this work, we frequently observed air layer thicknesses approaching the scales at which inter-molecular forces such as van der Waals attraction and gas kinetic effects (GKE) become relevant [23]. For nucleation driven contact on mica, the increasing rate of liquid-solid contact initiation as air layer thicknesses decreases is also consistent with the experiments on rougher surfaces [67]; several of the contacts we observed formed from distances exceeding 70 nm from the surface (\sim the mean free path length for air).

Both of the liquids that we considered wet the mica surfaces. Hence, the net interfacial forces between liquid-solid should be attractive which act in favor of destabilizing the air film. However, we observe few differences in the behaviors of silicon oil and the water-glycerol solution before the contact.

The transition from droplet rebound to spontaneous contact is immediate for silicon oil - at the critical rebound velocity, the oil drop may bounce or create a ring of contact (Fig. 4.5.c). The water-glycerol droplets behaved differently. There is a range of $U = 0.55 - 0.7$ m/s, that no rebound or spontaneous contacts were observed - all the contacts were nucleated. Despite several tries with freshly made solutions, use of different mica sheets, and change of nozzle, we did not observe any spontaneous contact formation for moderate impact velocities of solution impact¹.

The second culprit of frequent nucleated contacts is the surface roughness possible due to mica sheet surface defects or microscopic debris residue that cannot be observed by

¹We used deionized water and glycerol with purity of > 99 percent for making the solutions. Apart from the common practices in the laboratory, we did not control for possible impurities of the mixture, so we cannot completely rule out their existence - though improbable.

eye and is under-resolved in $x_1 - x_2$ plane by our microscope objective. As the same person performed the task of mica cleaving and utilized the very same technique for both series of experiments with the oil and solution, we expect the probability of nucleated contact occurrence to be proportionate to the total area of the air layer in the $x_1 - x_2$ plane. We compared the event of oil droplet rebound impact at $U = 0.48$ m/s with $h^* = 70$ nm with solution droplet rebound of the same h^* and the difference in the film area is only 13 percent mostly due to the small difference in droplet sizes. However, when comparing Fig. 4.5.a and b, the difference in statistics are much greater. Further comparison between of Fig. 4.5.a,b show the mean $h_{\min}^{\text{nucleation}}$ in the experiments with the water-glycerol (~ 100 nm) is larger compared to ~ 60 nm for oil. Hence, even if these contact nucleation are because of discrete surface roughness, these singular troughs poke silicon oil and the solution differently. This suggests that the magnitude of interfacial forces is different for the two. The electrostatic nature of interfacial forces can explain this.

One possibility is that the water-air interface became charged moreso than the silicon oil-air interface. Indeed, if one supposes that randomly fluctuating electromagnetic fields exist in the laboratory, generated by, *e.g.*, cameras, the laser, etc. that could not be isolated electrically from the impact surface, then the large dielectric constant of the water [3] suggests that the water-air interface should charge more than the silicon oil-air interface. The silicon oil is an excellent liquid dielectric with very small dielectric constant 2.6 as per the data from the supplier. The value for water-glycerol 10 cSt solution is much larger ≈ 62 as per literature [3]. Pure silicone oil droplets (without water absorption) do not contain a sufficient concentration of any ions and counter-ions for the appearance of any Coulomb force or Maxwell pressure even in extreme electrical fields [49]. On the other hand, there are experimental evidences showing immediately after cleaving the mica a reaction between the mica, CO₂ and water in air occurs [22]. Hence, the mica surface is covered by up to one formula unit of K₂CO₃ per nano-metre which is mobile in humid conditions, and crystallizes under drier conditions. The surface charge patches on mica develops inevitably as soon as we cleave it. As all the mica substrates were prepared in the same way, we assume a similar static charge distribution on the mica surface [22]. Thus, it is possible that the water-air interface contained some static charges that trigger nucleated contact for an intermediate range of impact velocity, where the timescale for spontaneous rupture of the air film was too long to be observed before nucleation took over. This is supported by the large height values of nucleated contacts for the water-glycerol solution droplets(Fig. 4.4.b). We have not measured the surface potential distribution of the surfaces, hence, cannot quantify the Maxwell pressure and comment on the validity of this hypothesis.

We now leave open the discussion on the erratic behavior of the solution and only consider the silicon oil droplets. Fig. 4.2.c and Fig. 4.5.c clearly show the systemic decrease of h^* to the upper bound of $h_{\min}^{\text{spontaneous}}$ ($= 35$ nm) with increase in U . This suggests that during the air film squeeze, the van der Waals interactions also attract the liquid surface

towards the solid and competes against the lubrication pressure in the air film.

While the ring of a spontaneous contact is well-defined (Fig. 4.1.d-e), the distribution of contacts on its circumference is not similar for all U . The dynamics of air film rupture are depicted graphically for two impact velocities, $U = 0.58$ and 0.91 m/sec, in Fig. 4.6.a-b. In order to compare the distribution of contacts around the ring for different U 's, we measure $h(t)$ on the ring of contact circumference, centered on the impact axis, with radius $r_{\min} = r_c^{(n)}$ with $r_c^{(n)}$ the radial distance from the impact axis to the point at which contact n initiates. We unwrapped the ring of contact formation, and made a kymograph in $\Theta - t$ as shown in Fig. 4.6.a-b. For slower drop impacts, fewer contacts form at larger mutual separation than the number of contacts forming beneath faster droplets. At highest velocity of 0.91 m/s, the spontaneous contact ring formation along $\Theta = 0 - 2\pi$ starts almost simultaneously which is in the limit of camera recording frequency which corresponding to $\Delta t = 12.5 \mu\text{s}$ (Fig. 4.6.b).

For U slightly greater than the critical velocity for droplet rebound, the air film is perforated discretely, with capillary bridges formed from the liquid closest to the surface; however, there can be a significant delay between the first air film rupture event and the final air film rupture event, Δt_c . For much higher velocity impacts, contact appear to form much more quickly, so that the air film appears to rupture symmetrically from the liquid closest to the surface, within the time resolution of our imaging.

We recorded the height-time traces for all points where liquid-solid contact initiated for the silicon oil. We measured the time t_c between first-passage of the liquid above and the initiation of contact. t_c decreases as U increases (Fig. 4.6.c) because the height at which the air film initially forms decreases with increasing U . However, $h_{\min}^{\text{spontaneous}}$ is almost constant as U varies. Hence, one might expect that the standard deviation of contact initiation times for N contact events,

$$\sigma_{t_c} := \frac{1}{N} \sqrt{\sum_{n=1}^{N-1} \Delta t_{c_n}}, \quad (4.1)$$

would also be independent of U . However, σ_{t_c} falls off abruptly when U increases, as can be seen in inset of Fig. 4.6.c. The conclusion we draw is that although the hydrodynamics of the thin air film formation plays no role in determining the threshold thickness from which the air film ultimately ruptures, it influences the collective rupture dynamics.

In order to compare our measurements with the theory, we must postulate values for the modified Hamaker constant (A) and the wavenumber in Eq. (1.17). In the absence of a directly measured Hamaker constant (A_H) for silicon oil and mica across air, we may take the measured value of the Hamaker constant for mica interacting with mica across air, calculated with Lifshitz theory to be $1e - 19$ J, and measured to be $1.35e - 19$ J [56]. Based on Fig. 4.6.e, we select the value of $A = 3e - 19$ J and wavenumber to provide good

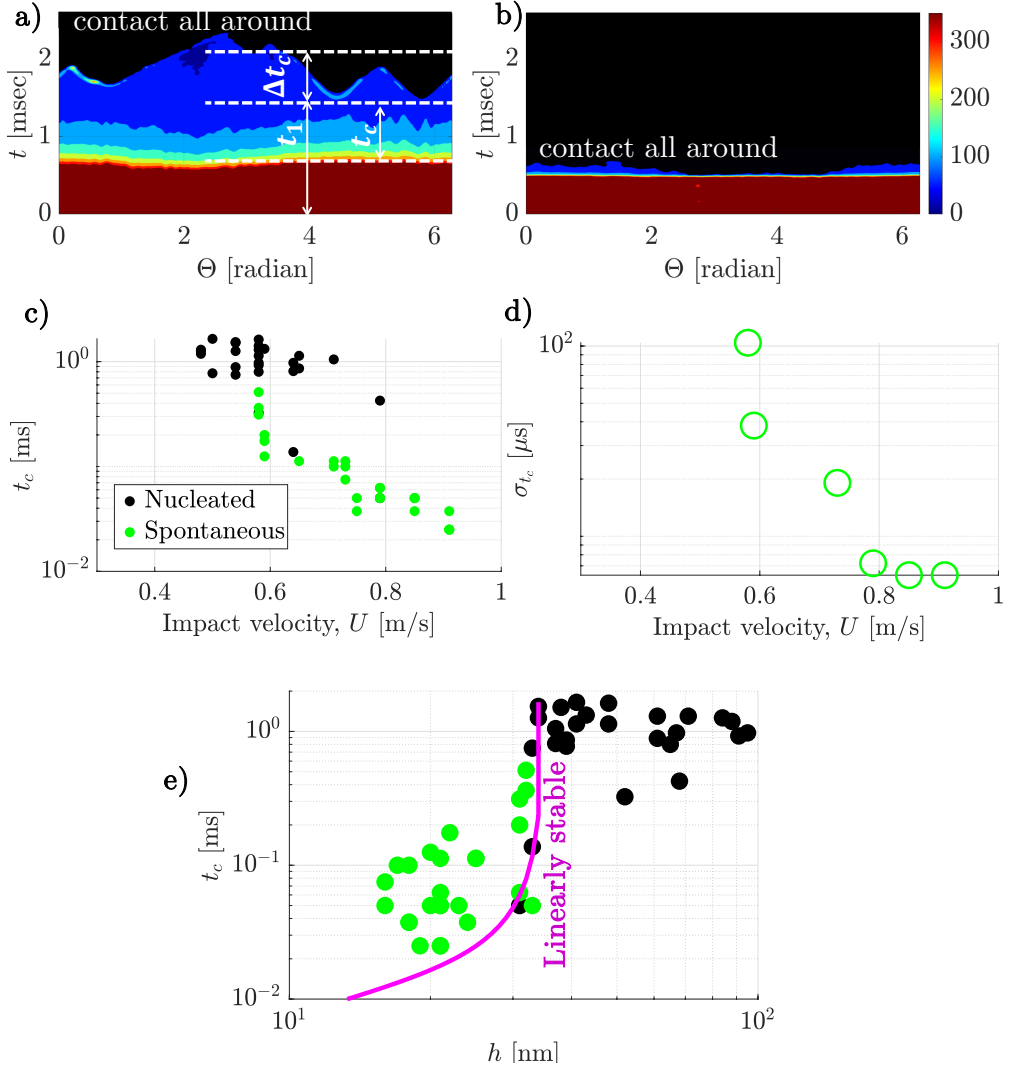


Figure 4.6: Kymographs of the initiation of contact on the circumference of the ring of contact $r = r_{\min}$, centered on the impact axis are plotted in (a,b) for silicon oil droplet impact velocities of $U = 0.58$ and 0.91 m/s, respectively. We made the $\Theta - t$ kymographs by unwrapping the ring of contact formation, $h(r_{\min}, t)$. We measured the time t_c between first passage of the liquid above the ring of contact until contact formations. At highest velocity of 0.91 m/s, the spontaneous contact ring formation along $\Theta = 0 - 2\pi$ starts almost simultaneously. The dynamics occurs close to the limit of camera recording frequency which corresponds to time steps of $12.5 \mu\text{s}$ as shown in (b). Timescale for the development of instability of the air layer under the silicon oil droplets are marked in (a). The data comprise the pairs of (U, t_c) in (c). h_{\min} 's are measured immediately before the initiation of contact for 75 impact events over the range of U . (d) shows that the standard deviation of t_c for the spontaneous contacts decreases suddenly as U increases. The magenta line specifies the transition to wetting based on linear stability analysis (Eq. (1.17)) with fitted parameters $A = 3e - 19$ J and $\frac{k}{2\pi} = 2e5$ 1/m.

agreement between the boundary separating spontaneous and nucleated contact events as $\frac{k}{2\pi} = 2e5 \text{ m}^{-1}$. Using these values, we compare t_c as a function of h_{\min} , substituting t_c for τ in Eq. (1.17) for the prediction of linear instability, as shown in Fig. 4.6.e. By evaluating the observed height and time before contact, the measured data are consistent with a linear instability driven by van der Waals forces.

4.4 Conclusion

We presented calibrated measurements of the nanometer-scale air film that forms prior to liquid-solid contact during droplet impact. In the absence of surface roughness, the liquid-air interface is destabilized when the attractive stresses (*e.g.*, van der Waals forces or electrostatic forces) overcome the stress associated with deforming the surface due to surface tension. This instability is characterized by a critical air film thickness (h^*) at which the wetting initiates. h^* for the silicon oil ($\approx 30 \text{ nm}$) is smaller than that of the water-glycerol solution ($\approx 60 \text{ nm}$); however, the local minimum air film thickness (h_{\min}) immediately prior to contact formation, is approximately the same value for both liquids ($\approx 20 \text{ nm}$). These observation suggests a means of addressing the challenging interfacial forces boundary condition that arises in the numerical calculation of thin film flows, by simply introducing a local cut-off scale for wetting fluids at 20 nm .

With our measurements, we identified two distinct forms of contact initiation - nucleated, and spontaneous - that are distinguished by the relative location of the localized wetting bridge and the location where the air film is most thin. For nucleated contacts, there is no correlation between these locations, whereas for spontaneous rupture events, there is nearly exact coincidence between the location of contact formation and the thinnest region of the air film.

The time to wait between air film formation and eventual rupture t_c is recorded for each event. The $t_c(h_{\min})$ data are then analyzed using the prediction of linear stability analysis for the timescale of linear instability development. A wave-number and Hamaker constant pair yield a line that separates all nucleated contacts from all spontaneous rupture events, highlighting the consistency of the observed air film destabilization events with the interfacial-forces driven instability in a spinodal-dewetting of the air film.

5 Droplet Impact: Liquid-Solid Nucleated Contact

In this Chapter, we examine the initial stages in the formation of liquid solid contact beneath the impacting drop, and resolve the liquid-air interface kinematics over 6 orders of magnitude of spatial scales, from nanometers to millimeters using FTIR microscopy. High speed FTIR microscopy enables us to probe the wetting process beneath the impacting drop with exceptional spatial and temporal resolution and facilitates the full 3-dimensional imaging of the advancing contact line and the nanometer thin film of air that initially separates the liquid from the solid.

5.1 Method

Drops with viscosities varying over two orders of magnitude are released from a syringe tip and impact upon a clean glass surface. We used solutions of water and glycerol to obtain fluids with viscosities ranging from 1 to 100 cSt at room temperature. In each of these experiments, the droplet diameter is approximately 3 mm and the impact velocity is between 0.5 and 0.7 m/sec, corresponding to an impact Weber number with a range of 10.4 – 27.8, calculated based on the droplet diameter. In this regime, the air film initially established during impact varies from approximately 300 to several tens of nm in thickness [68]. As shown in Fig. 5.1.a, to visualize the liquid-air interface, we illuminate the upper surface of a dove prism from below with a collimated, monochromatic light source at an angle of incidence greater than the total internal reflection angle for a glass-air interface, thus exciting an exponentially decaying evanescent field immediately above the glass surface. Any liquid that enters the evanescent field above the surface will

This chapter appeared in *Phys. Rev. Fluids* as Kolinski, J. M., Kaviani, R., Hade, D., and Rubinstein, S. M. (2019). Surfing the capillary wave: Wetting dynamics beneath an impacting drop. *Phys. Rev. Fluids*, 4:123605.

Authors' Contributions J.M.K. and S.M.R. conceived the project. J.M.K. conducted the experiments and post-processing. R.K. and D.H. built and calibrated the experimental setup under the guidance of J.M.K. J.M.K. and S.M.R. equally contributed to drafting the manuscript. R.K. and J.M.K. prepared the supplementary materials, figures, revision of the manuscript, and responses to the reviewers.

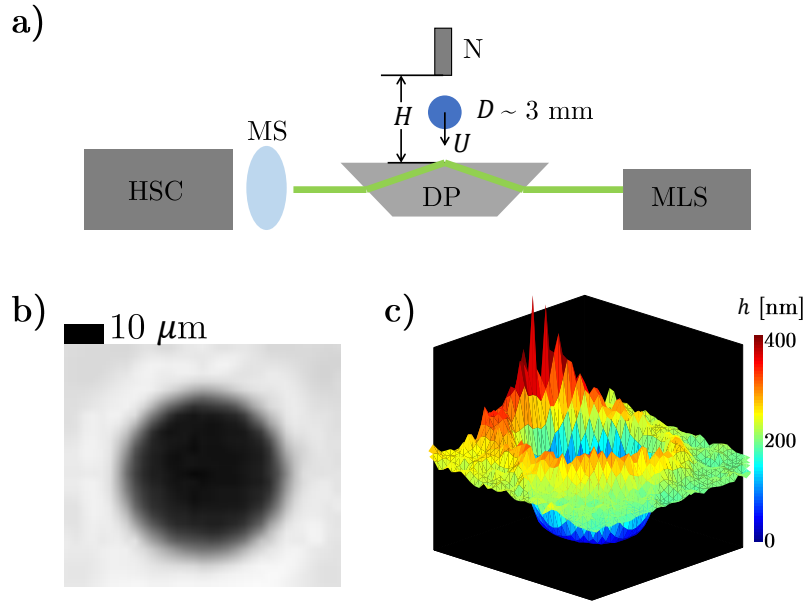


Figure 5.1: High speed FTIR imaging of the initiation of wetting: (a) Collimated, monochromatic light (MLS) totally internally reflects off of the glass-air interface (DP). The angle of incidence is tuned such that for a glass-liquid interface light no longer obeys the conditions for total internal reflection and instead transmits through a wet glass. Reflected light exiting the prism is magnified with a long working distance microscope objective (MS) and is imaged on our fast camera’s imaging sensor (Phantom V711) (HSC) at up to 180,000 frames per second. (b) A typical FTIR image of a capillary bridge formed beneath the thin film of air approximately 500 microns from the center of the impact. The height profile of the liquid above the solid surface can be calculated from the recorded intensity. (c) 3D rendering of the height map for the contact patch shown in (b). Colorbar indicates the height above the glass surface.

allow the light to partially transmit into it. Previous experiments in our group using the technique [68–70] employed a total-energy transfer algorithm to invert the intensity data. However, such transfer algorithm does not account for the polarization of the light [140] introduced in Chapter 3 resulting in increasing the error bars of the measurements. By imaging the light after it exits the prism with our camera’s imaging sensor, we are not light limited, and indeed we can perform ultra-high speed imaging at rates exceeding 180,000 frames per second in order to reconstruct the three-dimensional profile of the liquid-air interface, as shown in Fig. 5.1.b-c.

5.2 Results

While the root mean square (RMS) roughness of the glass slides is of the order of nanometers, sparsely distributed defects on the glass surface will exceed tens or even hundreds of nanometers in height above the surface [68, 86]; these protrusions may

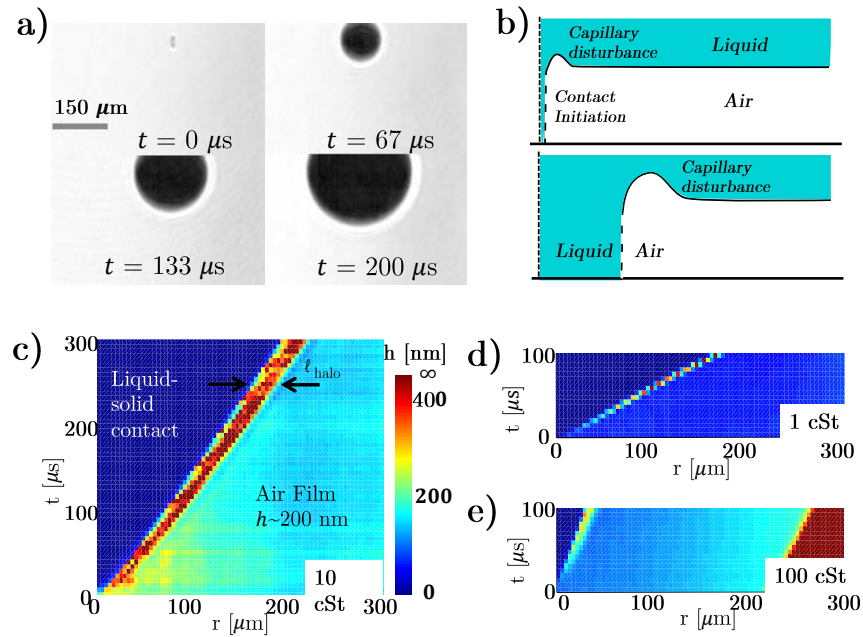


Figure 5.2: Initiation and growth of liquid-solid contact: (a) A sequence of FTIR images showing the initiation of contact between the glass surface and a 10 cSt liquid drop. At $t = 0$, the contact first forms. As time progresses, the contact line moves symmetrically out from the initial point of contact formation. The air ahead of the advancing wetting front fails to drain and instead deforms the liquid-air interface. Consequently, a bright ‘halo’ surrounds the liquid bridge. (b) A schematic representing the $r - z$ plane normal to the impact surface demonstrates how the halo region grows ahead of the advancing contact¹. The conformation of the liquid-air interface (dashed line) cannot be resolved below one micron with the FTIR method, limiting our ability to resolve the profile within nanometers of the contact line. (c) The azimuthally-averaged height profiles are plotted in a kymograph for 10 cSt liquid. The contact line progresses outward with a nearly constant velocity, and the lateral extent of the halo grows over time, as indicated by the widening of the bright red region. (d) A kymograph of liquid-solid contact initiation beneath a 1 cSt liquid drop shows similar, albeit more rapid, dynamics. (e) A kymograph of liquid-solid contact beneath a 100 cSt liquid drop. Here, the contact line moves with a slower velocity.

therefore exceed the thickness of the thin film of air above the surface of the glass, and thus act as nucleation sites for the formation of a capillary nano-bridge. These sparse nuclei are the dominant mechanism for contact initiation in most realistic systems [68, 69]. We characterize the initial dynamics of wetting by analyzing images of the FTIR intensity captured with our fast-camera. For all the fluid viscosities and film thicknesses that we examined, the initial formation of a solid-liquid contact region occurs in a qualitatively similar manner, as shown for a typical example in Fig. 5.2.a. Initially, a point-like contact

¹In this chapter the radius, r , is measured from the center of initial contact point, while in Chapter 4, it was from the symmetry axis of the droplet impact event.

forms beneath the thin film of air; simultaneously, a capillary disturbance is excited at the liquid-air interface wherein the displaced air is driven. This feature reduces the radius of curvature of the interface ahead of the advancing contact line, thus reducing the capillary pressure. The initiation and growth of the capillary disturbance are shown schematically in Fig. 5.2.b. This disturbance appears in the FTIR images as a bright region, or *halo*, encircling the dark spot, which indicates the wetted area. The contact angle between the liquid and the glass is small and therefore, once the contact is formed the wetting front rapidly spreads laterally outward at an approximately constant velocity, eventually reaching the boundary of the thin film of air.

Before the spreading contact line can progress, it must first displace the air in its path; however, the hydrodynamic resistance of the air, which is confined in the thin gap beneath the drop, is very high. Similar flow conditions occur at the onset of droplet coalescence, but the boundary conditions are fundamentally distinct [96, 120]. The capillary number, $Ca_G = \frac{\eta U}{\gamma}$, for this flow is very small, suggesting that the air viscosity plays a negligible role; however, this does not account for the confinement of the air in the thin film beneath the impacting drop: here, the thin gap amplifies resistance to the flow of the air. The deformation of the liquid from the formation of the halo leads to the development of a Laplace pressure, and consequently a pressure drop toward the edge of the spreading droplet, where the pressure is atmospheric; this pressure drop is $\Delta p \sim 0.01 - 0.1$ atm. As a result of the air's strong confinement upon impact, this pressure drop is insufficient to expel the air ahead of the advancing contact line^{II}. Instead, the air accumulates and forces the liquid-air interface to rise and curve at the leading edge, effectively inflating a toroidal bubble.

As the liquid bridge expands and the contact region continuously grows, the halo also grows to accommodate the increasing volume of displaced air, similar to classical inertial and viscous dewetting [46]. The dynamics of the expanding bridge are summarized as a function of space and time for three viscosities in the kymographs shown in Fig. 5.2.c-e. $t = 0$, $r = 0$, indicate the center of the initial contact point. The growing dark region on the left side of the plots corresponds to the wetted area, labeled 'liquid-solid contact' in Fig. 5.2.c. Similar dynamics are observed for the full range of measured viscosities, up to 100 cSt, as shown in Fig. 5.2.d-e. For higher viscosity liquids, the wetting front proceeds more slowly than for lower viscosity liquids; however, the shape of the profile of the air film ahead of the wetting front is qualitatively similar for all air film thicknesses and all liquid viscosities.

^{II}We consider the flow of the air in the thin gap to be viscous due to the thin gap between the droplet and the solid surface. For a typical gap of 100 nm, when the air is driven by the pressure built up in the halo at 0.1 atm over a lateral gap of 100 μm , we estimate a flow velocity of ~ 5 mm/sec at the largest, significantly less than the velocities observed in the experiment, implying that the air accumulates in the halo instead of being forced from the gap by the advancing contact line. For air flow at this velocity, the air film volume loses less than 1/100 of its initial value during contact-line propagation over 100 microseconds, consistent with our observation that h_{film} is nearly constant during the course of the experiment.

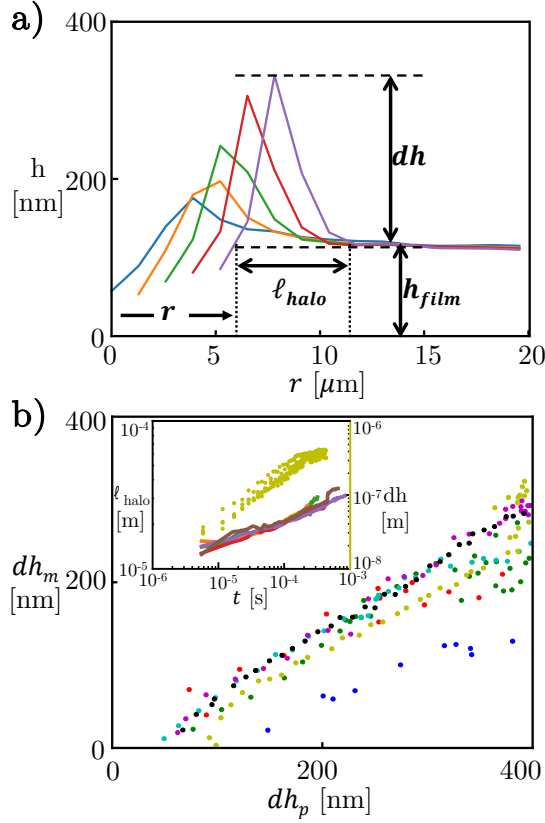


Figure 5.3: Kinematics of the wetting front: (a) Five consecutive height profiles ($dt = 5.5 \mu\text{sec}$) of a wetting front propagating outward from the point of contact initiation. The halo region leading the propagating front excites a capillary wave ahead of it, with a lateral extent, ℓ_{halo} , and vertical dimension, dh . The front position, r_c , is defined as the location where the wetting front reaches the height of the film in the far field h_{film} . (b) The volume of air displaced by the advancing wetting front, assuming the air is incompressible, can be used to develop a prediction for dh , $dh_p = rh_{film}/\ell_{halo}$. The measured value of dh , dh_m , is obtained via FTIR measurements immediately after contact initiation, and compares favorably with dh_p , as can be seen by the direct relationship between these quantities. Inset: ℓ_{halo} as a function of t ; colors represent different viscosities. ℓ_{halo} grows slowly in time; no systematic dependence of ℓ_{halo} is found as ν is varied. The height of the halo feature dh increases in time, as shown here for $\nu = 76 \text{ cSt}$ liquid, as can be seen by the gold points corresponding to the axis on the right-hand side of the plot.

At the earliest stages of contact formation and growth, we directly observe the three-dimensional geometry of the liquid-air interface, and measure both the height, dh , and breadth, ℓ_{halo} , of the deformed interface surrounding the liquid bridge, as shown in the height profiles, $h(r)$, Fig. 5.3.a; the gas film thickness, h_{film} , remains nearly constant as the wetting front progresses [68], as can be seen by the overlap of the successive profiles at large r . For an ensemble of many droplet impacts, we find that the lateral scale of the halo feature ℓ_{halo} grows slowly in time and at the same rate, independent of viscosity, as

shown in the inset to Fig. 5.3.b. Whereas typically dh rapidly exceeds the sub-micron resolution of the FTIR imaging modality, we are able to measure this height at the earliest stage of the capillary nano-bridge for the highest viscosities. The halo shape is robust, and does not measurably deform; this can be understood by the Capillary number for flow in the air, which at the highest contact line velocities is approximately $Ca \sim 10^{-4}$; thus surface tension maintains the shape of the propagating halo [46]. For the earliest instants of contact formation, we also compute the predicted halo height, $dh_p = \frac{h_{film} \cdot r}{\ell_{halo}}$, and compare it to the measured halo height, dh_m , finding good agreement for most viscosities. While the measured and predicted values for dh nearly agree, we see that the measurement is consistently less than the predicted value as shown in Fig. 5.3.b, main plot. This implies that the air is either slowly draining or compressing; however, the capillary stresses correspond to a fraction of a percent of an atmosphere, suggesting that the air is in fact slowly draining from beneath the impacting droplet.

As the liquid bridge spreads, the contact line velocity v remains approximately constant, as shown for 3 different viscosities in Fig. 5.2. As previously stated, similar dynamics are observed during droplet coalescence, where the expanding neck grows at a constant rate before a transition to slower growth [96]; here, our boundary conditions are different, and we do not see a transition, but instead the contact grows at a nearly constant velocity. This velocity does not appear to depend on the air film thickness through which it propagates. Under these conditions, for pure water the capillary pressure generated by a capillary bridge across an air film of 100 nm would rapidly accelerate the contact line to the limiting velocity, given by the balance of inertial and capillary stresses [6], $v = \sqrt{\gamma/(\rho h)} = 26$ m/sec. For $h = 10$ nm, $v = 83$ m/sec, this velocity will even exceed the liquid-capillary limit set by $\gamma/\eta = 70$ m/sec! However, we observe entirely different dynamics: here, the wetting front propagates more than an order of magnitude slower, and at the same speed v through a 10 nm-thick film of air as through a 100 nm-thick film of air, and is thus insensitive to the air film thickness. This suggests that liquid inertia alone does not limit v , and that dynamics of contact initiation and growth are significantly altered by the halo region ahead of the advancing contact line.

The anomalously low measured values of v points to an alternative mechanism of contact line motion through the thin film of air. In order to understand how a wetting front spreads, we consider the flow near the contact line, shown schematically in Fig. 5.4.a. The air ahead of the contact line cannot drain fast enough through the thin gap and instead accumulates in the halo. The contact line advances, driven by wetting forces; however, it must also be accommodated by flow of the liquid along the liquid-air interface. This flow must bypass the halo, which acts as a geometrical disturbance. Thus, the contact line is effectively *dragging* the halo through the drop's lower surface. This provides added inertial resistance to the motion of the contact line, and limits spreading speeds to that of a capillary wave, or the rate at which a disturbance with a typical scale ℓ_{halo} can move on the surface of the liquid as the contact line advances. However, the formation of the halo at the leading edge of the contact line leads to a resistance fundamentally dissimilar

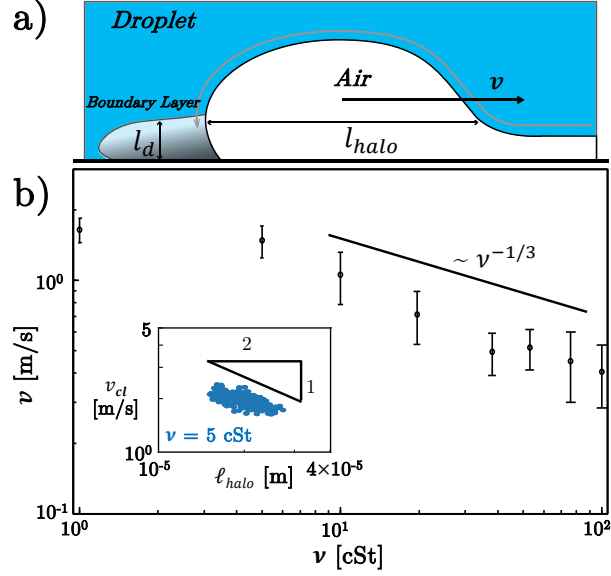


Figure 5.4: Surfing on a capillary wave: a) A schematic of the spreading capillary bridge. Fluid is shown in blue, the halo region and thin film of air are shown in white, and the surface is indicated by the black solid line. Viscous dissipation is localized in a boundary-layer, indicated by the region trailing the contact line. b) The average contact line velocity is plotted as a function of liquid viscosity; error bars indicate standard deviation of all contact events. Mean velocity decreases as a non-linear function of liquid viscosity. inset: over a small range, the velocity varies inversely with ℓ_{halo} for the 5 cSt liquid, consistent with the predicted scaling for a capillary wave.

from classical dewetting films [46, 99, 128]. Here, the contact line is resisted also by the inertia of the fluid displaced by the air in the halo.

The breadth of the halo region varies slowly, and thus we can estimate a wave number corresponding to the average length of $\langle \ell_{halo} \rangle_t = 20 \mu\text{m}$, and the velocity of such capillary disturbances given by $c = \sqrt{\frac{2\pi\gamma}{\rho\ell_{halo}}}$, where c is the wetting velocity [46]. Substituting the typical value of $\ell_{halo} = 20 \mu\text{m}$ into this expression, we find that $c = 4.3 \text{ m/sec}$, which has the same order of magnitude as the velocity of the lowest viscosity 1 cSt water - glycerol solution that we measured.

In order to check whether the capillary wave argument has experimental support, we can use the predicted relationship between c and ℓ_{halo} in the inertial limit, where $c \propto \ell_{halo}^{-1/2}$. The velocity is nearly constant as shown in Fig. 5.2, and ℓ_{halo} varies extremely slowly as shown in Fig. 5.3; nevertheless, these quantities do vary slightly over the course of the experiment. For the 5 cSt liquid, the contact line velocity appears to vary inversely with ℓ_{halo} , as shown in Fig. 5.4 inset. While the range of v and ℓ_{halo} is insufficient to verify the predicted scaling, the nearly 500 data points shown indicate consistency with the capillary wave argument.

5.3 Discussion

If we expect the wetting speed to weigh up the contact line capillary velocity, it should correlate linearly with the inverse of liquid viscosity. This is while, the measured velocities do not vary strongly as such for lowest viscosity values. However, our data density at these lower viscosity values is insufficient to comment on whether this is a distinctive regime, and how it might start transition to a viscous-dominated regime observed for higher viscosities as shown in Fig. 5.4.(b) .

How will the spreading velocity change for a more viscous fluid? Typically the dissipation at the contact line should occur on the scale of the flow; our observed ℓ_{halo} lengthscale is the only candidate scale here, and thus the volume wherein the dissipation occurs should be $r\ell_{halo}^2$. This scaling suggests that the contact line velocity should scale as the square-root of the radius, which is inconsistent with observations, however; thus we introduce a scaling that incorporates a viscous boundary layer. The flow around the halo is inertial^{III}, but close enough to the contact line the fluid flows on scales that are sufficiently small for the dynamics to be dominated by viscous dissipation. Dissipation is nevertheless confined to a boundary layer along the solid-liquid interface, and the propagation dynamics are governed by the balance of viscous and capillary stresses:

$$\frac{\gamma}{\rho\ell_{halo}} \sim \nu \frac{v}{\ell_d},$$

where $\ell_d \sim \sqrt{\nu\tau}$ is the length-scale over which dissipation occurs and is determined by the time required for a boundary layer to develop τ . Here we note that the dominant intrinsic length scale ℓ_{halo} sets $\tau \sim \frac{\ell_{halo}}{v}$. The stress balance equation then reads: $\frac{\gamma}{\rho\ell_{halo}} \sim \sqrt{\frac{\nu}{\ell_{halo}}} v^{3/2} \rightarrow v \sim \left(\frac{\gamma}{\rho\sqrt{\nu\ell_{halo}}}\right)^{2/3}$. This suggests that the contact line velocity varies inversely with the kinematic viscosity, consistent with our measurements.

While our experiments were conducted at low impact velocities significantly below the splashing threshold, the observed wetting velocity might affect splashing, as viscous liquids typically eject their sheet at a much later stage of the dynamics, when contact through the air film is likely to have occurred [39]. When a drop approaches a solid surface, even at moderate velocities the initial dynamics of wetting are strongly altered by the confined air film, which is displaced by the wetting fluid, and consequently deforms the liquid-air interface ahead of the contact line. The deformation results in a capillary disturbance that precedes the wetting front and leads to anomalously low wetting velocities beneath the impacting drop. These dynamics, ahead of the contact line, are inertial. Several nanometers below, trailing the contact line, a boundary layer is formed and the flow is viscous. These dynamically different regimes are coupled by

^{III}As viscosity increases, we anticipate that viscous effects will play an increasingly important role; using the contact line velocity and ℓ_{halo} to calculate the Reynolds number $Re = vL/\nu = v\ell_{halo}/\nu$, we find that the Reynolds number goes from ~ 20 for pure water, down to 0.06 for the 100 cSt solution; the Reynolds number is approximately 1 for the 20 cSt solution

the halo geometry, as on the one hand, the size of the boundary layer depends on the time it takes the wetting front to traverse the size of the halo. On the other hand, the size of the halo depends on the propagation speed of the contact line, which is driven by the extreme curvature and hindered by the trailing viscosity. Thus, the wetting front is surfing on a capillary wave and dragging a viscous tail in its wake.

6 Conclusions and Perspectives

The goal of this dissertation was to experimentally investigate the wetting dynamics of droplets falling on smooth surfaces through air. We developed nanometer precise measurement techniques and employed high-speed imaging for our observation of droplet deformation, air film formation and rupture, liquid-solid contact formation, and propagation of the contact line on the surface. We included the circumstantial conclusions at the end of each chapter. Here, we summarize our main findings followed by few future perspectives.

6.1 Conclusions

6.1.1 Microscopy

We implemented and calibrated 2 highly-sensitive microscopy techniques (FTIR and FIF) to monitor the air film thickness and morphology at high speed during the droplet impact process. We employed machine learning algorithms to improve FIF resolution in the $x_1 - x_2$ plane for droplet impacts. Using deep neural networks, we eliminated the painful FIF fringe demodulation. We showed that the FTIR microscopy can achieve 4D profilometry accurate up to few nano-meters in the x_3 direction for both homogeneous and birefringent substrates.

6.1.2 Wetting Initiation

Before a droplet can contact a surface during impact, it must first displace the air beneath it. Over a wide range of impact velocities, the droplet first compresses the air film, enhancing its resistance to drainage, and slowing the progress toward the surface; indeed, the air film can resist the droplet so much that it rebounds off of the air film without making contact. For impact velocities exceeding a critical impact velocity, the droplet always makes contact. The initiation of contact formation requires a topological

transition whereby the initially connected gas domain is ruptured, and a liquid capillary bridge forms, connecting the droplet to the surface. Our measurements showed that for impact velocities exceeding the critical velocity, the air film ruptures at a nearly identical height 20 nm, for two fluids - silicone oil and a water glycerol mixture. By evaluating the observed height and time before contact, we showed that the data are consistent with a linear instability driven by van der Waals forces for experimentally measured values of the Hamaker constant.

Crucially, there is a distinction between the silicone oil and the water solution, that implicates another mechanism for nucleation of contact during impact of the solution. The premature nucleation of contact beneath impacting solution droplets might be due to electrostatic charges, but the data are widely scattered, and a systematic outcome was not obtained for contact formation at the transitional impact velocity between bouncing and contact formation. These observations suggest a means of addressing the challenging interfacial forces boundary condition that arises in the numerical calculation of thin film flows, by simply introducing a contact cut-off scale for wetting fluids at 20 nm.

6.1.3 Wetting Propagation

The wetting process resulting from an impact of a droplet is mediated by the formation and growth of nanoscale liquid bridges, binding the liquid to the solid across a thin film of air. As the liquid bridge expands, air accumulates and deforms the liquid-air interface, and a capillary wave forms ahead of the advancing wetting front. The contact line is surfing on the capillary wave. 2 new length-scales l_{halp} and dh govern the dynamics of the propagating contact line beneath the impacting drop. All of these dynamics revolve around the entrained air film beneath the impacting drop. This capillary wave regularizes the pressure at the advancing wetting front and explains the anomalously low wetting velocities observed in the experiment.

6.2 Perspectives

In the course of this research, we identified several open questions. Three of these questions are named below as possible future research directions.

6.2.1 Microscopy on Curved Surfaces and Scale Dependency

We conducted all our dynamic profilometry measurements on flat rigid surfaces. Before, during, or after an impact, a compliant surface may deform, become curved, or shape sharp ridges [20, 62, 62, 72, 91, 133]. This may compromise the accuracy of our profilometry technique depending on the length scale and radius of the surface curvature.

Hentschel and Schomerus [52] formulated curvature corrections to Fresnel's laws at a nonplanar boundary. The implications of such corrections in the FTIR and FIF microscopy methods are yet to be studied and incorporated. The mapping procedure from the recorded reflected light intensity to profilometry may no longer be straightforward and require solution of an optical inverse problem. Deep learning-based algorithms can be explored as a possible solution, where numerical calculations of Maxwell's equations are used to generate training data.

There are further difficulties in measuring surface profiles with sharp boundaries. These are attributed to the perceptible reflected lights outside the numerical aperture of the objective or inadequate image resolution for steep height differences. This makes it challenging to use our optical techniques on nano/micro-scale solid substrate topographies [132].

6.2.2 Soft Interfaces

In all of our work, the impact surface was a rigid solid. In our research group, other scientists are studying the impact of soft elastic hemisphere on flat rigid substrates [138]. This has extensive applications in the field of soft robotics. They found evidence that depending on the impact speed a pocket of air can get trapped in a dimple between the hemisphere and the substrate, preventing direct solid–solid contact at the center of the impact area. The current microscopy setup constructed in this work can be readily used for visualization and dynamic profilometry of the soft elastic impactors, shedding light onto dynamic processes occurring during compliant impact.

Alternatively, there is much discussion about the role of substrate compliance on *e.g.* droplet splashing [55]. Despite the profound activity in the area of wetting on compliant substrates, little exists in the direct measurement of air film thickness and contact formation during droplet impact. The microscopy methods described in this work could be directly employed to this end using a coated substrate.

6.2.3 Additional Physical Effects

In this work, we mainly varied the liquid properties, but not the properties of the surrounding gas. It would be interesting to study the dependency of nanometer-scale air film on the ambient pressure of the surrounding gas.

Recently, Gao et al. [44] studied the dynamics of electrically charged falling droplets prior to contact with solid substrates. The electrostatic stresses profoundly alter the wetting outcome and can even suppress formation of the air dimple. The scale of short-range forces like electrical double layer forces and Maxwell pressure are unexplored territories.

In our work, we did not quantify the surface potential of the liquid/solid surfaces^I. Quantitative consideration through calculation of the electrostatic forces acting on the droplet surface might shed light on physical mechanisms of air film rupture under the impacting droplets.

^IWe measured the total surface charge of few mica sheets by use of Electrometer model B2987B provided by keysight (www.keysight.com). However, the measured quantities are the sum all of charges including those on the sheet edges that come onto contact with the probe.

Bibliography

- [1] Abouelsoud, M. and Bai, B. (2021). Bouncing and coalescence dynamics during the impact of a falling drop with a sessile drop on different solid surfaces. Physics of Fluids, 33(6):063309.
- [2] Attard, P. and Miklavcic, S. J. (2001). Effective spring constant of bubbles and droplets. Langmuir, 17(26):8217–8223.
- [3] Behrends, R., Fuchs, K., Kaatze, U., Hayashi, Y., and Feldman, Y. (2006). Dielectric properties of glycerol/water mixtures at temperatures between 10 and 50°C. The Journal of Chemical Physics, 124:144512.
- [4] Betelu, S. and Fontelos, M. (2004). Capillarity driven spreading of circular drops of shear-thinning fluid. Mathematical and Computer Modelling, 40(7):729 – 734.
- [5] Biance, A.-L., Chevy, F., Clanet, C., Lagubeau, G., and Quéré, D. (2006). On the elasticity of an inertial liquid shock. Journal of Fluid Mechanics, 554:47–66.
- [6] Biance, A.-L., Clanet, C., and Quéré, D. (2004). First steps in the spreading of a liquid droplet. Physical Review E, 69:016301.
- [7] Black, J., Chen, S., Thomas, J. G., and Zhu, Y. (2020). Deep neural networks for efficient phase demodulation in wavelength shifting interferometry. Optics Communications, 475:126250.
- [8] Bodony, D. J., Zagaris, G., Reichert, A., and Zhang, Q. (2010). Aeroacoustic predictions in complex geometries. Procedia Engineering, 6:234 – 243.
- [9] Bodony, D. J., Zagaris, G., Reichert, A., and Zhang, Q. (2011). Provably stable overset grid methods for computational aeroacoustics. Journal of Sound and Vibration, 330(17):4161 – 4179.
- [10] Boelens, A. M. P., Latka, A., and de Pablo, J. J. (2018). Observation of the pressure effect in simulations of droplets splashing on a dry surface. Physical Review Fluids, 3:063602.

- [11] Bouwhuis, W., van der Veen, R. C. A., Tran, T., Keij, D. L., Winkels, K. G., Peters, I. R., van der Meer, D., Sun, C., Snoeijer, J. H., and Lohse, D. (2012). Maximal air bubble entrainment at liquid-drop impact. Physical Review Letters, 109:264501.
- [12] Brenner, M. P. and Gueyffier, D. (1999). On the bursting of viscous films. Physics of Fluids, 11(3):737–739.
- [13] Brochard-Wyart, F. and Daillant, J. (2011). Drying of solids wetted by thin liquid films. Canadian Journal of Physics, 68:1084–1088.
- [14] Brooks, C. F., Grillet, A. M., and Emerson, J. A. (2006). Experimental Investigation of the Spontaneous Wetting of Polymers and Polymer Blends. Langmuir, 22(24):9928–9941.
- [15] Buguin, A., Vovelle, L., and Brochard-Wyart, F. (1999). Shocks in inertial dewetting. Physical Review Letters, 83:1183–1186.
- [16] Butt, H. (1991). Measuring electrostatic, van der waals, and hydration forces in electrolyte solutions with an atomic force microscope. Biophysical Journal, 60(6):1438–1444.
- [17] Carre, A. and Woehl, P. (2002). Hydrodynamic behavior at the triple line of spreading liquids and the divergence problem. Langmuir, 18(9):3600–3603.
- [18] Chandra, S. and Avedisian, C. T. (1991). On the collision of a droplet with a solid surface. Proceedings of the Royal Society of London. Series A: Mathematical and Physical Sciences, 432(1884):13–41.
- [19] Chantelot, P. and Lohse, D. (2021). Drop impact on superheated surfaces: short-time dynamics and transition to contact. Journal of Fluid Mechanics, 928:A36.
- [20] Chen, L., Bonaccorso, E., Deng, P., and Zhang, H. (2016). Droplet impact on soft viscoelastic surfaces. Physical Review E, 94:063117.
- [21] Chesshire, G. and Henshaw, W. (1990). Composite overlapping meshes for the solution of partial differential equations. Journal of Computational Physics, 90(1):1 – 64.
- [22] Christenson, H. K. and Thomson, N. H. (2016). The nature of the air-cleaved mica surface. Surface Science Reports, 71(2):367–390.
- [23] Chubynsky, M. V., Belousov, K. I., Lockerby, D. A., and Sprittles, J. E. (2020). Bouncing off the walls: The influence of gas-kinetic and van der waals effects in drop impact. Physical Review Letters, 124:084501.
- [24] Crua, C., Shoba, T., Heikal, M., Gold, M., and Higham, C. (2010). High-speed microscopic imaging of the initial stage of diesel spray formation and primary breakup. SAE 2010 Powertrains Fuels & Lubricants Meeting.

BIBLIOGRAPHY

- [25] de Ruijter, M., De Coninck, J., Blake, T., Clarke, A., and Rankin, A. (1997). Contact angle relaxation during the spreading of partially wetting drops. Langmuir, 13(26):7293–7298.
- [26] de Ruijter, M. J., Blake, T. D., and De Coninck, J. (1999). Dynamic wetting studied by molecular modeling simulations of droplet spreading. Langmuir, 15(22):7836–7847.
- [27] de Ruijter, M. J., Charlot, M., Voué, M., and De Coninck, J. (2000). Experimental evidence of several time scales in drop spreading. Langmuir, 16(5):2363–2368.
- [28] de Ruiter, J., Lagraauw, R., Mugele, F., and van den Ende, D. (2015a). Bouncing on thin air: how squeeze forces in the air film during non-wetting droplet bouncing lead to momentum transfer and dissipation. Journal of Fluid Mechanics, 776:531–567.
- [29] de Ruiter, J., Lagraauw, R., van den Ende, D., and Mugele, F. (2014). Wettability-independent bouncing on flat surfaces mediated by thin air films. Nature Physics, 11:48.
- [30] de Ruiter, J., Mugele, F., and van den Ende, D. (2015b). Air cushioning in droplet impact. I. Dynamics of thin films studied by dual wavelength reflection interference microscopy. Physics of Fluids, 27(1):012104.
- [31] de Ruiter, J., Oh, J. M., van den Ende, D., and Mugele, F. (2012). Dynamics of collapse of air films in drop impact. Physical Review Letters, 108:074505.
- [32] de Ruiter, J., van den Ende, D., and Mugele, F. (2015c). Air cushioning in droplet impact. II. experimental characterization of the air film evolution. Physics of Fluids, 27(1):012105.
- [33] Deka, H. and Pierson, J.-L. (2020). Revisiting the taylor-culick approximation. II. retraction of a viscous sheet. Physical Review Fluids, 5:093603.
- [34] Deng, L. and Yu, D. (2014). Deep learning: Methods and applications. Foundations and Trends in Signal Processing, 7(3–4):197–387.
- [35] Dhaouadi, W. and Kolinski, J. M. (2019). Bretherton’s buoyant bubble. Physical Review Fluids, 4(12):123601.
- [36] Dillavou, S., Rubinstein, S. M., and Kolinski, J. M. (2019). The virtual frame technique: ultrafast imaging with any camera. Optical Express, 27(6):8112–8120.
- [37] Dimiduk, D. M., Holm, E. A., and Niezgodá, S. R. (2018). Perspectives on the impact of machine learning, deep learning, and artificial intelligence on materials, processes, and structures engineering. Integrating Materials and Manufacturing Innovation, 7(3):157–172.
- [38] Driscoll, M. M. and Nagel, S. R. (2011). Ultrafast interference imaging of air in splashing dynamics. Physical Review Letters, 107:154502.

-
- [39] Driscoll, M. M., Stevens, C. S., and Nagel, S. R. (2010). Thin film formation during splashing of viscous liquids. Physical Review E, 82(3):036302.
- [40] Du, Y., Wang, C., Zhang, C., Guo, L., Chen, Y., Yan, M., Feng, Q., Shang, M., Kuang, W., Wang, Z., and Huang, Z.-L. (2021). Computational framework for generating large panoramic super-resolution images from localization microscopy. Biomedical Optical Express, 12(8):4759–4778.
- [41] Duchemin, L. and Josserand, C. (2011). Curvature singularity and film-skating during drop impact. Physics of Fluids, 23(9):091701.
- [42] Duchemin, L. and Josserand, C. (2020). Dimple drainage before the coalescence of a droplet deposited on a smooth substrate. Proceedings of the National Academy of Sciences, 117:202007857.
- [43] Feng, S., Chen, Q., Gu, G., Tao, T., Zhang, L., Hu, Y., Yin, W., and Zuo, C. (2019). Fringe pattern analysis using deep learning. Advanced Photonics, 1(02):1.
- [44] Gao, F., Yi, H., Qi, L., Qiao, R., and Deng, W. (2019a). Weakly charged droplets fundamentally change impact dynamics on flat surfaces. Soft Matter, 15:5548–5553.
- [45] Gao, Y., Jung, S., and Pan, L. (2019b). Interaction forces between water droplets and solid surfaces across air films. ACS Omega, 4(15):16674–16682. PMID: 31616850.
- [46] Gennes, P.-G., Brochard-Wyart, F., and Quéré, D. (2004). Capillarity and Wetting Phenomena: Drops, Bubbles, Pearls, Waves. Springer New York, NY.
- [47] Gordillo, J. M., Riboux, G., and Quintero, E. S. (2019). A theory on the spreading of impacting droplets. Journal of Fluid Mechanics, 866:298–315.
- [48] Gordillo, L., Sun, T.-P., and Cheng, X. (2018). Dynamics of drop impact on solid surfaces: evolution of impact force and self-similar spreading. Journal of Fluid Mechanics, 840:190–214.
- [49] Granda, R., Li, G., Yurkiv, V., Mashayek, F., and Yarin, A. L. (2022). Dielectrophoretic stretching of drops of silicone oil: Experiments and multi-physical modeling. Physics of Fluids, 34(4):042108.
- [50] Gu, C. and Yeh, P. (1993). Extended jones matrix method II. J. Opt. Soc. Am. A, 10(5):966–973.
- [51] Hendrix, M. H. W., Bouwhuis, W., van der Meer, D., Lohse, D., and Snoeijer, J. H. (2016). Universal mechanism for air entrainment during liquid impact. Journal of Fluid Mechanics, 789:708–725.
- [52] Hentschel, M. and Schomerus, H. (2002). Fresnel laws at curved dielectric interfaces of microresonators. Physical Review E, 65:045603.

BIBLIOGRAPHY

- [53] Hicks, P. and Purvis, R. (2010). Air cushioning and bubble entrapment in three-dimensional droplet impacts. Journal of Fluid Mechanics, 649:135–163.
- [54] Hoffmann, J., Bar-Sinai, Y., Lee, L. M., Andrejevic, J., Mishra, S., Rubinstein, S. M., and Rycroft, C. H. (2019). Machine learning in a data-limited regime: Augmenting experiments with synthetic data uncovers order in crumpled sheets. Science Advances, 5(4).
- [55] Howland, C. J., Antkowiak, A., Castrejón-Pita, J. R., Howison, S. D., Oliver, J. M., Style, R. W., and Castrejón-Pita, A. A. (2016). It’s harder to splash on soft solids. Physical Review Letters, 117:184502.
- [56] Israelachvili, J. (2011). Intermolecular and Surface Forces, 3rd Edition. Academic Press.
- [57] Jha, A., Chantelot, P., Clanet, C., and Quéré, D. (2020). Viscous bouncing. Soft Matter, 16:7270–7273.
- [58] Jian, Z., Josserand, C., Popinet, S., Ray, P., and Zaleski, S. (2018). Two mechanisms of droplet splashing on a solid substrate. Journal of Fluid Mechanics, 835:1065–1086.
- [59] Jin, H., Jiao, T., Clifton, R. J., and Kim, K.-S. (2022). Dynamic fracture of a bicontinuously nanostructured copolymer: A deep-learning analysis of big-data-generating experiment. Journal of the Mechanics and Physics of Solids, 164:104898.
- [60] Johnson, K. L. (1985). Contact Mechanics. Cambridge University Press.
- [61] Josserand, C. and Thoroddsen, S. (2016). Drop impact on a solid surface. Annual Review of Fluid Mechanics, 48(1):365–391.
- [62] Karpitschka, S., Das, S., Gorcum, M., Perrin, H., Andreotti, B., and Snoeijer, J. (2015). Droplets move over viscoelastic substrates by surfing a ridge. Nature communications, 6:7891.
- [63] Kaviani, R., Afshari, A., Nikkhah-Bahrami, M., and Ebrahimi, M. (2011). LES of a nozzle/jet aeroacoustics. International Congress on Sound and Vibration, ICSV, 1:333–340.
- [64] Kaviani, R. and Kolinski, J. M. (2019). HOTNNET. <https://gitlab.epfl.ch/kaviani/hotnnet>.
- [65] Kaviani, R. and Kolinski, J. M. (2023). High resolution interferometric imaging of liquid-solid interfaces with hotnnet. Experimental Mechanics, 63(2):309–321.
- [66] Kim, I. I., Paik, S., Jeon, Y. B., Park, J. S., Kim, H., and Kim, H. (2018). Full-field thickness measurement of ultrathin liquid film in receding contact-induced nano-channel using surface plasmon resonance. Optical Express, 26(16):20975–20989.

- [67] Kolinski, J. M., Kaviani, R., Hade, D., and Rubinstein, S. M. (2019). Surfing the capillary wave: Wetting dynamics beneath an impacting drop. Physical Review Fluids, 4:123605.
- [68] Kolinski, J. M., Mahadevan, L., and Rubinstein, S. (2014a). Drops can bounce from perfectly hydrophilic surfaces. Europhysics Letters, 108(2):24001.
- [69] Kolinski, J. M., Mahadevan, L., and Rubinstein, S. M. (2014b). Lift-off instability during the impact of a drop on a solid surface. Physical Review Letters, 112(13):134501.
- [70] Kolinski, J. M., Rubinstein, S. M., Mandre, S., Brenner, M. P., Weitz, D. A., and Mahadevan, L. (2012). Skating on a film of air: drops impacting on a surface. Physical Review Letters, 108(7):074503.
- [71] Kumar, U. P., Haifeng, W., Mohan, N. K., and Kothiyal, M. (2012). White light interferometry for surface profiling with a colour CCD. Optics and Lasers in Engineering, 50(8):1084–1088.
- [72] Langley, K. R., Castrejón-Pita, A. A., and Thoroddsen, S. T. (2020). Droplet impacts onto soft solids entrap more air. Soft Matter, 16:5702–5710.
- [73] Latka, A. (2017). Thin-sheet creation and threshold pressures in drop splashing. Soft Matter, 13:740–747.
- [74] Lavi, B. and Marmur, A. (2004). The exponential power law: partial wetting kinetics and dynamic contact angles. Colloids and Surfaces A: Physicochemical and Engineering Aspects, 250(1):409 – 414.
- [75] LeCun, Y., Bengio, Y., and Hinton, G. (2015). Deep learning. Nature, 521:436.
- [76] Lee, J. S., Weon, B. M., Je, J. H., and Fezzaa, K. (2012). How does an air film evolve into a bubble during drop impact? Physical Review Letters, 109:204501.
- [77] Lee, S., Oh, O., Kim, Y., Kim, D., Hussey, D. S., Wang, G., and Lee, S. W. (2020). Deep learning for high-resolution and high-sensitivity interferometric phase contrast imaging. Scientific Reports, 10(1):9891.
- [78] Lee, T., Jeong, H., Kim, H., Lee, S., and Kim, D. (2016). Effect of platen shape on evolution of total thickness variation in single-sided lapping of sapphire wafer. International Journal of Precision Engineering and Manufacturing-Green Technology, 3(3):225–229.
- [79] Li, E. Q. and Thoroddsen, S. T. (2015). Time-resolved imaging of a compressible air disc under a drop impacting on a solid surface. Journal of Fluid Mechanics, 780:636–648.
- [80] Li, Z., Li, X., and Liang, R. (2020). Random two-frame interferometry based on deep learning. Optical Express, 28(17):24747–24760.

BIBLIOGRAPHY

- [81] Liu, C., Bonaccorso, E., Sokuler, M., Auernhammer, G. K., and Butt, H.-J. (2010). Dynamic wetting of polyisoprene melts: Influence of the end group. Langmuir, 26(4):2544–2549.
- [82] Liu, Y., Moevius, L., Xu, X., Qian, T., Yeomans, J. M., and Wang, Z. (2014). Pancake bouncing on superhydrophobic surfaces. Nature Physics, 10:515.
- [83] Liu, Y., Tan, P., and Xu, L. (2013). Compressible air entrapment in high-speed drop impacts on solid surfaces. Journal of Fluid Mechanics, 716:R9.
- [84] Liu, Y., Tan, P., and Xu, L. (2015). Helmholtz instability in an ultrathin air film causes drop splashing on smooth surfaces. Proceedings of the National Academy of Sciences, 112(11):3280–3284.
- [85] Lo, H. Y., Liu, Y., and Xu, L. (2017). Mechanism of contact between a droplet and an atomically smooth substrate. Physical Review X, 7:021036.
- [86] Mandre, S. and Brenner, M. P. (2012). The mechanism of a splash on a dry solid surface. Journal of Fluid Mechanics, 690:148–172.
- [87] Mandre, S., Mani, M., and Brenner, M. P. (2009). Precursors to splashing of liquid droplets on a solid surface. Physical Review Letters, 102:134502.
- [88] Mani, M., Mandre, S., and Brenner, M. P. (2010). Events before droplet splashing on a solid surface. Journal of Fluid Mechanics, 647:163–185.
- [89] Min, Q., Duan, Y.-Y., Wang, X.-D., Liang, Z.-P., Lee, D.-J., and Su, A. (2010). Spreading of completely wetting, non-newtonian fluids with non-power-law rheology. Journal of Colloid and Interface Science, 348(1):250 – 254.
- [90] Mishra, S., Rubinstein, S. M., and Rycroft, C. H. (2022). Computing the viscous effect in early-time drop impact dynamics. Journal of Fluid Mechanics, 945:A13.
- [91] Mitra, S., Vo, Q., and Tran, T. (2021). Bouncing-to-wetting transition of water droplets impacting soft solids. Soft Matter, 17:5969–5977.
- [92] Monnier, J. D. (2003). Optical interferometry in astronomy. Reports on Progress in Physics, 66(5):789–857.
- [93] Mundo, C., Sommerfeld, M., and Tropea, C. (1995). Droplet-wall collisions: Experimental studies of the deformation and breakup process. International Journal of Multiphase Flow, 21(2):151 – 173.
- [94] Pack, M., Hu, H., Kim, D., Zheng, Z., Stone, H. A., and Sun, Y. (2017). Failure mechanisms of air entrainment in drop impact on lubricated surfaces. Soft Matter, 13:2402–2409.

-
- [95] Pack, M., Kaneelil, P., Kim, H., and Sun, Y. (2018). Contact line instability caused by air rim formation under nonsplashing droplets. Langmuir, 34(17):4962–4969.
- [96] Paulsen, J. D., Burton, J. C., and Nagel, S. R. (2011). Viscous to inertial crossover in liquid drop coalescence. Physical Review Letters, 106:114501.
- [97] Qiao, C., Li, D., Guo, Y., Liu, C., Jiang, T., Dai, Q., and Li, D. (2021). Evaluation and development of deep neural networks for image super-resolution in optical microscopy. Nature Methods, 18(2):194–202.
- [98] Rädler, J. O. and Sackmann, E. (1992). Imaging optical thicknesses and separation distances of phospholipid vesicles at solid surfaces. Journal de Physique II, 3(5):727–748.
- [99] Reyssat, É. and Quéré, D. (2006). Bursting of a fluid film in a viscous environment. Europhysics Letters, 76(2):236–242.
- [100] Riboux, G. and Gordillo, J. M. (2014). Experiments of drops impacting a smooth solid surface: A model of the critical impact speed for drop splashing. Physical Review Letters, 113:024507.
- [101] Roisman, I. V., Rioboo, R., and Tropea, C. (2002). Normal impact of a liquid drop on a dry surface: Model for spreading and receding. Proceedings: Mathematical, Physical and Engineering Sciences, 458(2022):1411–1430.
- [102] Rubinstein, S. M., Cohen, G., and Fineberg, J. (2004). Detachment fronts and the onset of dynamic friction. Nature, 430(7003):1005–1009.
- [103] Sajjadi, M. S., Scholkopf, B., and Hirsch, M. (2017). Enhancenet: Single image super-resolution through automated texture synthesis. In Proceedings of the IEEE International Conference on Computer Vision, pages 4491–4500.
- [104] Sanjay, V., Chantelot, P., and Lohse, D. (2022). When does an impacting drop stop bouncing? arXiv:2208.05935.
- [105] Schilling, J., Sengupta, K., Goennenwein, S., Bausch, A., and Sackmann, E. (2004). Absolute interfacial distance measurements by dual-wavelength reflection interference contrast microscopy. Physical Review E, 69:021901.
- [106] Schroll, R. D., Josserand, C., Zaleski, S., and Zhang, W. W. (2010). Impact of a viscous liquid drop. Physical Review Letters, 104:034504.
- [107] Semal, S., Voué, M., De Ruijter, M., Dehuit, J., and De Coninck, J. (1999). Dynamics of spontaneous spreading on heterogeneous surfaces in a partial wetting regime. Journal of Physical Chemistry B, 103(23):4854–4861.

BIBLIOGRAPHY

- [108] Sevenler, D., Avci, O., and Ünlü, M. S. (2017). Quantitative interferometric reflectance imaging for the detection and measurement of biological nanoparticles. Biomedical Optical Express, 8(6):2976–2989.
- [109] Seveno, D., Vaillant, A., Rioboo, R., Adão, H., Conti, J., and De Coninck, J. (2009). Dynamics of wetting revisited. Langmuir, 25(22):13034–13044.
- [110] Sherer, S. E. and Scott, J. N. (2005). High-order compact finite-difference methods on general overset grids. Journal of Computational Physics, 210(2):459 – 496.
- [111] Shirota, M., van Limbeek, M. A. J., Lohse, D., and Sun, C. (2017). Measuring thin films using quantitative frustrated total internal reflection (FTIR). The European Physical Journal E, 40(5):54.
- [112] Simonyan, K. and Zisserman, A. (2014). Very deep convolutional networks for large-scale image recognition. arXiv 1409.1556.
- [113] Sprittles, J. E. (2015). Air entrainment in dynamic wetting: Knudsen effects and the influence of ambient air pressure. Journal of Fluid Mechanics, 769:444–481.
- [114] Stalcup, E. J., Seemann, R., Herminghaus, S., and Law, B. M. (2009). Dissipation mechanisms in ionic liquids. Journal of Colloid and Interface Science, 338(2):523 – 528.
- [115] Su, X. and Zhang, Q. (2010). Dynamic 3-D shape measurement method: A review. Optics and Lasers in Engineering, 48(2):191–204.
- [116] Tadmor, R., Yadav, S. B., Gulec, S., Leh, A., Dang, L., N’guessan, H. E., Das, R., Turmine, M., and Tadmor, M. (2018). Why drops bounce on smooth surfaces. Langmuir, 34(15):4695–4700.
- [117] Taylor, S. G. and Saffman, P. G. (1957). Effects of compressibility at low reynolds number. Journal of the Aeronautical Sciences, 24(8):553–562.
- [118] Thomas, R. (2003). Wetting kinetics study of modified polyimide surfaces containing ionizable functional groups. Langmuir, 19(14):5763–5770.
- [119] Thoroddsen, S. T., Etoh, T. G., and Takehara, K. (2003). Air entrapment under an impacting drop. Journal of Fluid Mechanics, 478:125–134.
- [120] Thoroddsen, S. T., Etoh, T. G., Takehara, K., and Ootsuka, N. (2005a). On the coalescence speed of bubbles. Physics of Fluids, 17(7):071703.
- [121] Thoroddsen, S. T., Etoh, T. G., Takehara, K., Ootsuka, N., and Hatsuki, Y. (2005b). The air bubble entrapped under a drop impacting on a solid surface. Journal of Fluid Mechanics, 545:203–212.

-
- [122] Thoroddsen, S. T., Takehara, K., and Etoh, T. G. (2010). Bubble entrapment through topological change. Physics of Fluids, 22(5):051701.
- [123] Tignon, J., Marquezini, M., Hasche, T., and Chemla, D. (1999). Spectral interferometry of semiconductor nanostructures. IEEE Journal of Quantum Electronics, 35(4):510–522.
- [124] Tsai, P., C. A. van der Veen, R., van de Raa, M., and Lohse, D. (2010). How micropatterns and air pressure affect splashing on surfaces. Langmuir, 26(20):16090–16095.
- [125] van der Veen, R. C. A., Tran, T., Lohse, D., and Sun, C. (2012). Direct measurements of air layer profiles under impacting droplets using high-speed color interferometry. Physical Review E, 85:026315.
- [126] Versluis, M. (2013). High-speed imaging in fluids. Experiments in Fluids, 54(2):1458.
- [127] Vithin, A. V. S., Ajithaprasad, S., and Rajshekhar, G. (2019). Step phase reconstruction using an anisotropic total variation regularization method in a diffraction phase microscopy. Applied Optics, 58(26):7189–7194.
- [128] Vrij, A. (1966). Possible mechanism for the spontaneous rupture of thin, free liquid films. Discussions of Faraday Society, 42:23–33.
- [129] Wang, G., Duchaine, F., Papadogiannis, D., Duran, I., Moreau, S., and Gicquel, L. Y. (2014). An overset grid method for large eddy simulation of turbomachinery stages. Journal of Computational Physics, 274:333 – 355.
- [130] Wang, X. D., Zhang, Y., Lee, D. J., and Peng, X. F. (2007). Spreading of completely wetting or partially wetting power-law fluid on solid surface. Langmuir, 23(18):9258–9262.
- [131] Worthington, A. M. and Clifton, R. B. (1877). On the forms assumed by drops of liquids falling vertically on a horizontal plate. Proceedings of the Royal Society of London, 25(171-178):261–272.
- [132] Wu, D. and Fang, F. (2021). Development of surface reconstruction algorithms for optical interferometric measurement. Frontiers of Mechanical Engineering, 16(1):1–31.
- [133] Xiong, Y., Huang, H., and Lu, X.-Y. (2020). Numerical study of droplet impact on a flexible substrate. Physical Review E, 101:053107.
- [134] Xu, L., Zhang, W. W., and Nagel, S. R. (2005). Drop splashing on a dry smooth surface. Physical Review Letters, 94:184505.
- [135] Yarin, A. (2006). Drop impact dynamics: Splashing, spreading, receding, bouncing. . . . Annual Review of Fluid Mechanics, 38(1):159–192.

BIBLIOGRAPHY

- [136] Zdravkov, A. N., Peters, G. W. M., and Meijer, H. E. H. (2006). Film drainage and interfacial instabilities in polymeric systems with diffuse interfaces. Journal of Colloid and Interface Science, 296(1):86–94.
- [137] Zewail, A. H. (2000). Femtochemistry: Atomic-scale dynamics of the chemical bond. The Journal of Physical Chemistry A, 104(24):5660–5694.
- [138] Zheng, S., Dillavou, S., and Kolinski, J. M. (2021). Air mediates the impact of a compliant hemisphere on a rigid smooth surface. Soft Matter, 17:3813–3819.
- [139] Zhong, C., Gao, Z., Wang, X., Gao, C., Yang, S., Sun, X., Wen, X., Feng, Z., and Wang, S. (2018). The machine learning method of phase extraction in interferometry. Optics and Lasers in Engineering, 110:384 – 391.
- [140] Zhu, S., Yu, A. W., Hawley, D., and Roy, R. (1986). Frustrated total internal reflection: A demonstration and review. American Journal of Physics, 54(7):601–607.
- [141] Zuo, C., Feng, S., Huang, L., Tao, T., Yin, W., and Chen, Q. (2018). Phase shifting algorithms for fringe projection profilometry: A review. Optics and Lasers in Engineering, 109:23 – 59.

Ramin Kaviani

ramin.kaviani@epfl.ch
No. 11, Avenue de Morges,
CH-1004 Lausanne, Switzerland
Phone: (+41) 77 908 9639

Research Assistant
Engineering Mechanics of Soft Interfaces
École Polytechnique Fédérale de Lausanne
EPFL | STI | IGM | EMSI
Local MED 2 2919, Station 9,
CH-1015 Lausanne, Switzerland

- EDUCATION**
- ◇ **PhD in Mechanical Engineering**, (2018-2023)
École Polytechnique Fédérale de Lausanne (EPFL), Lausanne, Switzerland
Thesis Title: Wetting Dynamics Beneath an Impacting Droplet
 - ◇ **M.Sc. in Mechanical Engineering**, GPA 18.28/20, (2009-2011)
University of Tehran, Tehran, Iran
Thesis Title: Numerical Investigations of Noise Generation in High Speed Jets
 - ◇ **B.Sc. in Mechanical Engineering**, GPA 17.27/20, (2004-2008)
University of Tehran, Tehran, Iran
Specialized Project Title: Three Dimensional Modeling of Compressible Flow in a Junction Using Parallel Processing: A Distributed-Memory Implementation of KIVA-3V
 - ◇ **Pre-University Degree**, GPA 19.50/20, (2004)
National Organization for Development of Exceptional Talents, Babol, Iran
- WORK EXPERIENCE**
- ◇ **Lead Construction Engineer**, Leighton Asia, (2017-2018)
Suite 8.1, Level 8, Menara Tokio Marine Life, 189 Jalan Tun Razak, 50400 Kuala Lumpur, Malaysia
 - ◇ **Senior Installation Engineer**, Bumi Armada Berhad, (2014-2017)
Level 23, Menara Perak, 24 Jalan Perak, 50450 Kuala Lumpur, Malaysia
 - ◇ **Senior Finite Element Engineer**, Leighton Offshore, (2012-2014)
Suite 9.01, Level 9, GTower, 199 Jalan Tun Razak, 50400 Kuala Lumpur, Malaysia
 - ◇ **Senior Pipeline Engineer**, Delta Offshore Technology, (2011-2012)
No. 61, 2nd floor, West Pirouzi St., Nasr Ave. (Gisha), Tehran, Iran
 - ◇ **Research Assistant**, Vehicle, Fuel & Environment Research Institute, (2007-2011)
College of Engineering, North Kargar Ave., Tehran, Iran
- COMPUTER SKILLS**
- ◇ **OS:** DOS, Windows, and Linux
 - ◇ **Programming:** C++, Python, and Fortran
 - ◇ **Open-source Software:** KIVA-3V, OpenFOAM, and OpenDX
 - ◇ **Engineering Software:** Pro|Engineer, Pointwise, ICEM, CFX, ADAMS, OrcaFlex, Sage Profile 3D, OFFPIPE, Bentley AutoPIPE, Moses, ANSYS Workbench, COMSOL, MATLAB & Simulink, Maple, Mathcad, Tecplot, and ...

PUBLICATIONS ◇ **Journal Papers**

- R. Kaviani and J. M. Kolinski, “High Resolution Interferometric Imaging of Liquid-Solid Interfaces with HOTNNET”, *Experimental Mechanics*, Vol. 63, Issue No. 2, pp. 309-321, 2022.
- J. M. Kolinski, R. Kaviani, D. Hade, and S. M. Rubinstein, “Surfing the Capillary Wave: Wetting Dynamics beneath an Impacting Drop”, *Physical Review Fluids*, Vol. 4, Issue No. 12, 2019.
- R. Kaviani and M. Nikkhah-Bahrami, “Improved Navier-Stokes Boundary Conditions Based on Generalized Characteristics”, *Journal of Computational Acoustics*, Vol. 23, Issue No. 2, 2015.
- R. Kaviani, V. Esfahanian, and M. Ebrahimi, “Wavelet-based Postprocessing of Jet LES Data for Acoustic Far-field Extrapolations”, *Journal of Computational Acoustics*, Vol. 21, Issue No. 4, 2013.
- A. Rastgo and R. Kaviani, “Classification of Different Approaches Based on Modeling and Simulation for a Kinematic Analysis of Planar and Spatial Mechanisms”, *International Journal of Mechanical and Materials Engineering*, Vol. 2, No. 2, pp. 139-149, 2007.

◇ **Conference Papers and Presentations**

- R. Kaviani, M. Ebrahimi, and M. Nikkhah-Bahrami, “Development of a High-Order Solver for LES of Aeroacoustics”, 9th EuroMech Fluid Mechanics Conference (EFMC9), September 9-13, 2012.
- M. Ebrahimi, R. Kaviani, and M. Nikkhah-Bahrami, “A High-order Hybrid Filtering for Computational Aeroacoustics”, 9th EuroMech Fluid Mechanics Conference (EFMC9), September 9-13, 2012.
- R. Kaviani, A. Afshari, M. Nikkhah-Bahrami, and M. Ebrahimi, “LES of a Nozzle/Jet Aeroacoustics”, Proceeding of 18th International Congress on Sound and Vibration (ICSV 18), Brazil, July 10-14, 2011.
- R. Kaviani, A. Afshari, and M. Ebrahimi, “Effects of LES Spatial Filtering on the Aerodynamic Sound Generation”, Proceeding of 18th International Congress on Sound and Vibration (ICSV 18), Brazil, July 10-14, 2011.
- R. Kaviani and A. Rastgo, “Optimum Design of Stewart Platform by Using Genetic Algorithm”, Proceeding of International Conference on Modeling and Simulation (MS'07), India, December 3-5, 2007.

CERTIFICATES ◇ **BOSIET (OPITO Approved):** Helicopter Underwater Escape Training including EBS, Sea Survival, Fire Fighting & Self Rescue, First Aid & Hypothermia, Skyscape, and Norwegian Helicopter Suit with Re-breather

◇ **Industrial Safety:** Labour Safety, Fire Safety, and Electrical Safety Training

◇ **EPFL COSEC:** Occupational Health and Safety, Laser Safety, Management of Chemical Hazards and Risks

LANGUAGE ◇ **Farsi:** Native

SKILLS ◇ **English:** Fluent

REFERENCE Available on request